Spin mapping at the nanoscale and atomic scale

Roland Wiesendanger

Institute of Applied Physics and Interdisciplinary Nanoscience Center Hamburg, University of Hamburg, D-20355 Hamburg, Germany

(Published 18 November 2009)

The direct observation of spin structures with atomic-scale resolution, a long-time dream in condensed matter research, recently became a reality based on the development of spin-sensitive scanning probe methods, such as spin-polarized scanning-tunneling microscopy (SP-STM) and magnetic exchange force microscopy (MExFM). This article reviews the basic principles and methods of SP-STM and MExFM and describes recently achieved milestones in the application of these techniques to metallic and electrically insulating magnetic nanostructures. Discoveries of novel types of magnetic order at the nanoscale are presented as well as challenges for the future, including studies of local spin excitations based on spin-resolved inelastic tunneling spectroscopy and measurements of damping forces in MExFM experiments.

DOI: 10.1103/RevModPhys.81.1495 PACS number(s): 68.37.−d, 75.75.+a, 75.25.+z, 75.30.Et

CONTENTS

I. INTRODUCTION

A fundamental understanding of magnetic and spin-dependent phenomena requires the determination of spin structures and spin excitations down to the atomic scale. The direct visualization of atomic-scale spin structures was first accomplished for magnetic metals by combining the atomic-resolution capability of scanning-tunneling microscopy (STM) with spin sensitivity, based on vacuum tunneling of spin-polarized electrons. The resulting technique, spin-polarized scanning-tunneling microscopy (SP-STM), nowadays provides unprecedented insight into collinear and noncollinear spin structures at surfaces of magnetic nanostructures and has already led to the discovery of new types of magnetic order at the nanoscale. More recently, the detection of spin-dependent exchange and correlation forces allowed a first direct real-space observation of spin structures at surfaces of antiferromagnetic insulators. This new type of scanning probe microscopy, called magnetic exchange force microscopy (MExFM), provides a powerful tool to investigate different types of spin-spin interactions based on direct, super-, or Ruderman-Kittel-Kasuya-Yoshida (RKKY) type exchange down to the atomic level. A combination of SP-STM with inelastic electron tunneling spectroscopy or of MExFM with high-precision measurements of damping forces now allows experimental observation of localized or confined spin excitations in magnetic systems of reduced dimensions.

II. HISTORY AND BACKGROUND

Quantum mechanical tunneling is an important physical phenomenon that plays a key role in many different branches of physics including nuclear, atomic, and molecular physics as well as condensed matter physics. Since the first perturbative treatment of tunneling (Bardeen, 1961), it has become clear that the experimentally measured differential tunneling conductance is directly linked to the local density of electronic states or, equivalently, to the squares of the wave functions summed up over some energy window. Therefore, tunneling experiments provide access to the most fundamental physical quantities from which many other properties of matter can be derived.

In the field of superconductivity tunneling experiments have proven to be indispensable (Giaever, 1974; Josephson, 1974) in obtaining detailed information about the superconducting condensate, e.g., the energy gap, the electron-phonon coupling strength, or the symmetry of the order parameter. Tunneling also plays a key role in many semiconductor heterostructures such as the well-known Esaki tunnel diode (Esaki, 1974).

Because tunneling efficiency is extremely distance dependent, it has become the basis for one of the most powerful microscopic techniques in modern condensed matter research, i.e., the STM (Binnig and Rohrer, 1987) and its derivatives. The STM has revolutionized the field of surface science and has become the basic experimental tool for nanoscience and nanotechnology (Wiesendanger, 1994a).

Spin-dependent or spin-polarized tunneling was first observed by Tedrow and Meservey (1971) using planar ferromagnet-oxide-superconductor tunnel junctions. A few years later, Jullière (1975) discovered spin-dependent tunneling between two planar ferromagnetic electrodes separated by an insulating tunnel barrier, which has recently become the basis for the development of magnetic random access memories (MRAMs) (Åkerman, 2005). In the following we first focus on spin-dependent tunneling experiments in planar ferromagnet-oxide-superconductor tunnel junctions because such experiments are important for the quantitative determination of the spin polarization of tunneling electrons. Then we discuss spin-dependent tunneling in planar ferromagnet-insulator-ferromagnet tunnel junctions as a preliminary step toward spin-dependent vacuum tunneling experiments in STM-type tunnel junctions.

A. Spin-polarized electron tunneling in planar tunnel junctions

1. Tunneling between a ferromagnet and a superconductor

The first observation of spin-dependent tunneling, and subsequently the quantitative determination of the spin polarization of the tunneling current in planar ferromagnet-oxide-superconductor tunnel junctions, was based on discovering the Zeeman splitting of the quasiparticle density of states for a superconducting thin film in a strong parallel magnetic field H (Meservey *et al.*, 1970). The Zeeman splitting leads to two BCS-type density-of-states curves shifted in energy by $\pm\mu H$ (μ is the electron magnetic moment) with respect to the density-of-states curve in the absence of an external magnetic field (Fig. 1, top). For the ferromagnetic counterelectrode the two parts (spin up and spin down) of the spin-dependent density of states are shifted relative to each other by the exchange energy, leading to a different density of states at the Fermi level for the two different spin states (Fig. 1, bottom). (To first approximation, it has been assumed that the spin-dependent density of states is constant within a small energy window around the Fermi level.) Examination of the full density-of-states diagram for the ferromagnet-oxide-superconductor tunnel junction in an applied parallel magnetic field (Fig. 1) makes clear that the difference in the density of states at the Fermi level for the two different spin states of the ferromagnetic electrode will lead to an asymmetry in the current-voltage and conductance-voltage characteristics as observed experimentally (Fig. 2). The spin polarization P of the tunneling current is given by

$$P \equiv \frac{N_{\uparrow} - N_{\downarrow}}{N_{\uparrow} + N_{\downarrow}}, \tag{1}$$

where $N_{\uparrow}$ ($N_{\downarrow}$) is the number of tunneling electrons with magnetic moment aligned parallel (antiparallel) to the direction of the magnetic field. By neglecting spin-orbit

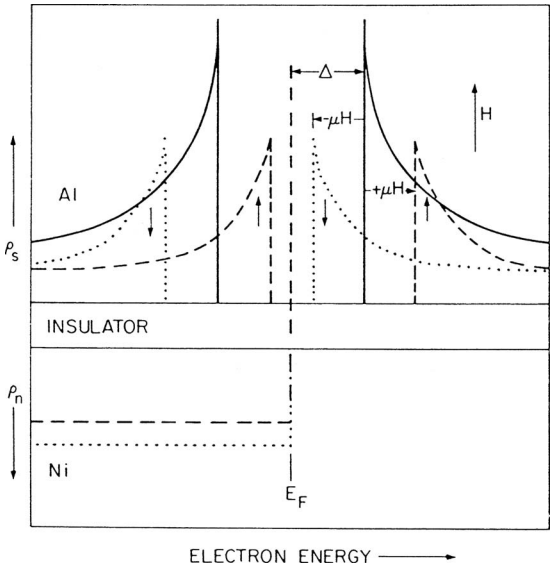

FIG. 1. Tunneling density-of-states diagram for an Al-oxide-Ni tunnel junction showing the Al electrode for a BCS-type density of states split into spin-up (increased in energy by μH) and spin-down (decreased in energy by μH) parts and an assumed predominance of spin-down (magnetic moment parallel to the field) carriers at the Fermi surface of Ni. Arrows on density of states refer to spin direction. From Tedrow and Meservey, 1971.

scattering in the superconducting electrode, which is a good approximation for sufficiently thin films (about 5 nm), and by assuming the absence of spin scattering in the tunnel barrier, Tedrow and Meservey (1973) showed that the polarization P can be determined experimentally from

$$P = \frac{(G_d - G_a) - (G_c - G_b)}{(G_d - G_a) + (G_c - G_b)}, \tag{2}$$

where G_i is the measured tunneling conductance at point i $(i=a,b,c,d)$ of the conductance-voltage curve (Fig. 2).

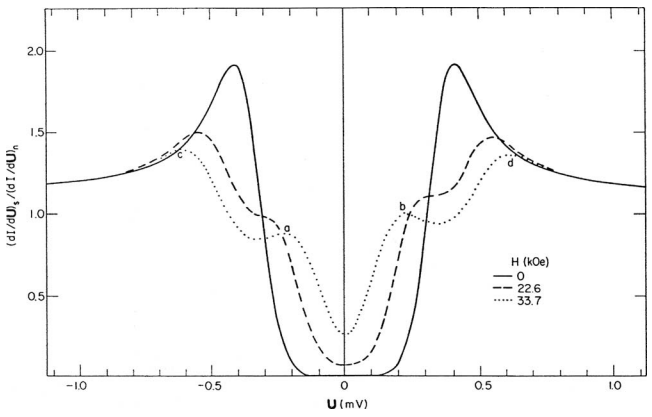

FIG. 2. Normalized conductance of an Al-Al_2O_3-Ni tunnel junction measured as a function of the voltage applied to the Al film for three values of applied magnetic field. The asymmetry of the conductance peaks a, b, c, and d (H=33.7 kOe) results from the spin polarization of the Ni carriers. From Tedrow and Meservey, 1971.

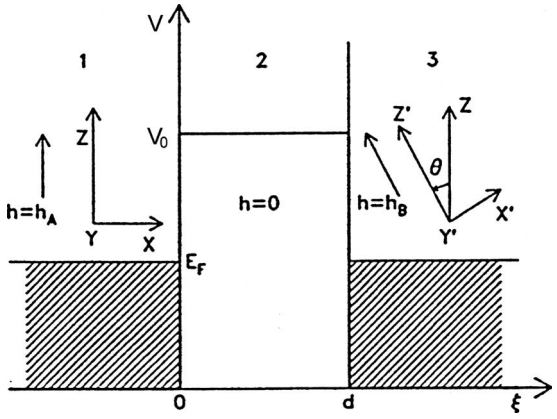

FIG. 3. Schematic potential diagram for two metallic ferromagnets separated by an insulating barrier. The directions of internal fields h_A and h_B within the magnets form an angle θ. From Slonczewski, 1989.

Because the tunneling current in these experiments is mainly dominated by the itinerant d_i electrons of the ferromagnetic electrode, which obtain their spin polarization through exchange interaction with the localized d_l electrons, Tedrow and Meservey measured the polarization of the d_i electrons in a narrow energy window within 1 meV around the Fermi level. In contrast, photoelectrons are dominated by localized states within a much larger energy window (typically on the order of eV) below the Fermi level. Moreover, photoelectrons have an escape depth of some nanometers below the sample surface, while electron tunneling probes the wave-function tails of the electronic states above the surface plane in the barrier region. Therefore, spin polarizations as determined by spin-polarized electron tunneling and spin-resolved photoelectron spectroscopy should generally not be compared with each other.

2. Tunneling between two ferromagnets

Spin-dependent tunneling can also be observed in planar ferromagnet-insulator-ferromagnet tunnel junctions (Jullière, 1975; Maekawa and Gäfvert, 1982). To explain the experimental observation, Slonczewski (1989) considered a tunnel junction with two ferromagnetic electrodes where the directions of the internal magnetic fields differ by an angle θ (Fig. 3). Using a stationary wave-function approach, a free-electron model, and considering the limiting case of a vanishing applied bias voltage, Slonczewski derived the following expression for the conductance G of a ferromagnet-insulator-ferromagnet tunnel junction in the case of two identical ferromagnetic electrodes separated by a rectangular barrier:

$$G = G_{\mathrm{fbf}}(1 + P_{\mathrm{fb}}^2 \cos\theta), \quad |P_{\mathrm{fb}}| \leqslant 1. \tag{3}$$

Here P_{fb} is the effective spin polarization of the ferromagnet-barrier interface and G_{fbf} is the tunneling conductance for the corresponding nonmagnetic case. If the two ferromagnetic electrodes are different, the conductance becomes

$$G = G_{\mathrm{fbf}'}(1 + P_{\mathrm{fb}}P_{\mathrm{f}'\mathrm{b}}\cos\theta). \quad (4)$$

For the two special cases of parallel and antiparallel alignment of the internal magnetic field directions, it follows that

$$G_{\uparrow\uparrow} = G_{\mathrm{fbf}'}(1 + P_{\mathrm{fb}}P_{\mathrm{f}'\mathrm{b}}),$$

$$G_{\uparrow\downarrow} = G_{\mathrm{fbf}'}(1 - P_{\mathrm{fb}}P_{\mathrm{f}'\mathrm{b}}). \quad (5)$$

Therefore, one obtains

$$\frac{G_{\uparrow\uparrow} - G_{\uparrow\downarrow}}{G_{\uparrow\uparrow} + G_{\uparrow\downarrow}} = P_{\mathrm{fb}}P_{\mathrm{f}'\mathrm{b}} =: P_{\mathrm{fbf}'} \quad (6)$$

for the effective spin polarization of the tunnel junction $P_{\mathrm{fbf}'}$.

B. Spin-polarized vacuum tunneling in STM

While electron tunneling experiments based on planar tunnel junctions had a large impact on the field of superconductivity from early on (Giaever, 1974), advances in the field of magnetic tunnel junctions were hindered for some time by inhomogeneities of the oxide layer (spatially variable thickness and magnetic impurities in the oxide). By replacement of the oxide tunnel barrier with a vacuum barrier, a much better-defined tunnel junction can be realized with an adjustable tunnel gap spacing (Young *et al.*, 1971; Binnig *et al.*, 1982a). The invention of the STM by Binnig and Rohrer (1982b, 1987) offered a powerful combination of the concepts of vacuum tunneling, point probing, and scanning, leading to novel methods of microscopy with atomic resolution (Binnig *et al.*, 1983). The combination of STM with electron tunneling spectroscopy methods at an energy resolution down to the μeV regime [scanning-tunneling spectroscopy (STS)] has become an indispensable experimental technique for probing electronic states and quantum effects spatially resolved at the nanoscale. Moreover, using magnetic probe tips the spin character of the electronic states can be probed with spin-resolved STM and STS (Wiesendanger, Güntherodt, *et al.*, 1990a; Bode, Getzlaff, and Wiesendanger, 1998; Wiesendanger, 1998).

1. Tersoff-Hamann theory of nonmagnetic STM

A link between the experimentally measured tunneling current in nonmagnetic STM and the electronic states of sample and tip has been made by Tersoff and Hamann (1983, 1985). The Tersoff-Hamann theory of STM is based on a perturbative treatment of tunneling as first introduced by Bardeen (1961). Within Bardeen's formalism, the following expression for the tunneling current I can be derived in first-order time-dependent perturbation theory:

$$I = \frac{2\pi e}{\hbar}\sum_{\mu,\nu}\{f(E_\mu)[1 - f(E_\nu + eU)] - f(E_\nu + eU)[1 - f(E_\mu)]\}|M_{\mu\nu}|^2\delta(E_\nu - E_\mu), \quad (7)$$

where $f(E)$ is the Fermi function, U is the applied sample bias voltage, $M_{\mu\nu}$ is the tunneling matrix element between the unperturbed electronic states Ψ_μ of the tip and Ψ_ν of the sample surface, and E_μ (E_ν) is the energy of the state Ψ_μ (Ψ_ν) in the absence of tunneling. The δ function describes the conservation of energy for the case of elastic tunneling. The essential problem is the calculation of the tunneling matrix element which, according to Bardeen (1961), is given by

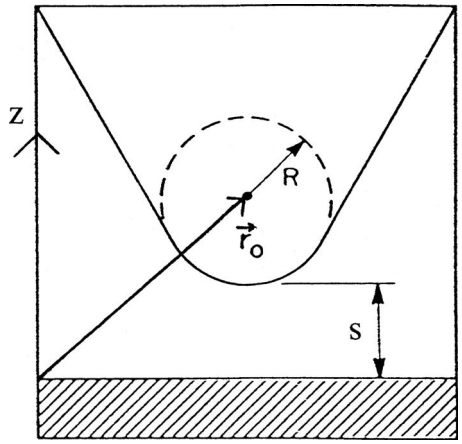

FIG. 4. Schematic of STM geometry in the Tersoff-Hamann model. The probe tip is assumed to be locally spherical with radius of curvature R, where it approaches nearest the sample surface (shaded). The distance of nearest approach is s. The center of curvature of the tip is labeled $\vec{r}_0$. From Tersoff and Hamann, 1983.

$$M_{\mu\nu} = \frac{-\hbar^2}{2m}\int dS(\Psi_\mu^*\nabla\Psi_\nu - \Psi_\nu\nabla\Psi_\mu^*), \quad (8)$$

where the integral has to be evaluated over any surface lying entirely within the vacuum barrier region separating the two electrodes. The quantity in parentheses can be identified as the current density $\vec{j}_{\mu\nu}$. To derive the matrix element $M_{\mu\nu}$ from Eq. (8), explicit expressions for the wave functions Ψ_μ and Ψ_ν of the tip and the sample surface are required. Unfortunately, the atomic structure of the STM tip is generally not known. Therefore, a model tip wave function has to be assumed for the calculation of the tunneling current. Tersoff and Hamann (1983, 1985) used the simplest model for the tip with a locally spherical geometry (Fig. 4). In this model, the tunneling matrix element is evaluated for an s-type tip wave function with an effective tip radius R and an inverse decay length κ,

$$\Psi_\mu = \frac{1}{R}e^{-\kappa R}, \quad (9)$$

whereas contributions from tip wave functions with angular dependence (orbital quantum number $l \neq 0$) have been neglected. As a further simplification, Tersoff and Hamann considered the limits of low temperatures and small applied bias voltage, for which the tunneling current becomes

$$I = \frac{2\pi e}{\hbar} U \sum_{\mu,\nu} |M_{\mu\nu}|^2 \delta(E_\nu - E_F)\delta(E_\nu - E_F), \tag{10}$$

where E_F is the Fermi energy. Within the *s*-wave approximation for the tip state [Eq. (9)], the following expression for the tunneling current is obtained:

$$I \propto U n_t(E_F) \exp(2\kappa R) \sum_{\nu} |\Psi_\nu(\vec{r}_0)|^2 \delta(E_\nu - E_F), \tag{11}$$

where $n_t(E_F)$ is the density of states at the Fermi level for the tip and $\vec{r}_0$ is the center of curvature of the tip. The quantity

$$n_S(E_F, \vec{r}_0) = \sum_{\nu} |\Psi_\nu(\vec{r}_0)|^2 \delta(E_\nu - E_F) \tag{12}$$

can be identified with the surface local density of states (LDOS) at the Fermi level E_F, i.e., the charge density from electronic states at E_F, evaluated at the center of the effective tip $\vec{r}_0$. The STM images obtained at low bias and at constant tunneling current therefore represent contour maps of constant surface LDOS at E_F evaluated at the center of curvature of the effective tip, provided that the *s*-wave approximation for the tip and the perturbative treatment of tunneling can be justified. The latter requires that the STM is operated with a sufficiently large tunneling gap resistance.

Since the sample wave functions decay exponentially in the z direction normal to the surface toward the vacuum region,

$$|\Psi_\nu(\vec{r})| \propto \exp(-\kappa z), \tag{13}$$

one gets

$$|\Psi_\nu(\vec{r}_0)|^2 \propto \exp[-2\kappa(s+R)], \tag{14}$$

where s denotes the distance between the sample surface and the front end of the tip (Fig. 4). Therefore, the tunneling current, given by Eq. (11), becomes exponentially dependent on the distance s,

$$I \propto \exp(-2\kappa s). \tag{15}$$

The strong distance dependence of the tunneling current provides the key for the atomic-resolution capability of the STM.

2. Beyond the Tersoff-Hamann theory of nonmagnetic STM

An extension of the Tersoff-Hamann theory toward consideration of tip states with orbital quantum number $l \neq 0$ was introduced by Chen (1990a, 1991), motivated by the fact that STM tips are usually made of tungsten, platinum, or iridium and are likely to have some *d*-like states near the Fermi level at the apex atom contributing to the tunneling current. Chen (1990a) showed that generally the tunneling matrix element for STM can be obtained from a "derivative rule": The angle dependence of the tip wave function in terms of x, y, and z is replaced by the corresponding derivatives acting on the sample surface wave function at the position of the center of the apex atom. For example, the tunneling matrix element for a d_{z^2} tip state is proportional to the second z derivative of the sample surface wave function at the center of the apex atom. In general, if a tip with a non-*s*-wave state is scanning over a sample surface, the constant-current STM image no longer represents a contour map of constant LDOS at E_F, but rather the tip apex atom follows a contour, determined by the derivatives of the sample surface wave functions. These exhibit a much stronger atomic corrugation than the contour of constant surface LDOS at E_F, resulting in an improved spatial resolution in STM experiments performed with tip states of higher orbital quantum number (Chen, 1990b).

Another limitation for the applicability of Eq. (10) is the restriction to small applied bias voltages. The applied bias voltage enters through the summation of states which can contribute to the tunneling current. Additionally, a finite bias can lead to a distortion of the tip and sample surface wave functions Ψ_μ and Ψ_ν as well as to a modification of the energy eigenvalues E_μ and E_ν. Derivation of these distorted tip and sample surface wave functions and energy eigenvalues is, however, a difficult problem. Therefore, as a first approximation, the undistorted zero-voltage wave functions and energy eigenvalues are usually taken. Consequently, the effect of a finite bias U only enters through a shift in energy of the undistorted surface wave functions or density of states relative to the tip by an amount of eU. Under these assumptions, the following expression for the tunneling current as a generalization of the result of Tersoff and Hamann for the low-bias limit can be obtained:

$$I \propto \int^{eU} n_t(\pm eU \mp E) n_s(E) T(E, eU) dE, \tag{16}$$

where $n_t(E)$ is the density of states for the tip and $n_s(E)$ that for the sample surface. All energies are measured with respect to the Fermi level. The energy- and bias-dependent transmission coefficient $T(E, eU)$ includes tunneling matrix element effects as well as the exponential distance dependence of the tunneling current.

For positive sample bias, the net tunneling current arises from electrons that tunnel from the occupied states of the tip into unoccupied states of the sample, whereas at negative sample bias, electrons tunnel from occupied states of the sample into unoccupied states of the tip. Varying the amount of the applied bias voltage, one can select the electronic states that contribute to the tunneling current and, in principle, measure the local electronic density of states. For example, the current strongly increases if the applied bias voltage allows the onset of tunneling into a maximum of the unoccupied sample electronic density of states. Therefore, the first derivative of the current-voltage characteristics $dI/dU(U)$ reflects the electronic density of states to a first approximation. However, we also have to consider the energy and bias dependence of the transmission coefficient $T(E, eU)$. Since electrons in states with the highest energy "see" the smallest effective tunneling barrier height, most of the tunneling current arises from

electrons near the Fermi level of the negatively biased electrode. As an important consequence, tunneling from the tip to the sample mainly probes the sample's empty electronic states with negligible influence of the tip's occupied states. On the other hand, tunneling from the sample to the tip is much more sensitive to the electronic structure of the tip's empty states which sometimes prevents detailed spectroscopic STM studies of the sample's occupied states.

3. Spin-resolved STM and tunneling spectroscopy

When magnetic materials are used for tip and sample an additional spin dependence of the tunneling current occurs, as in the case of planar magnetic tunnel junctions. For a theoretical description following Bardeen's perturbative treatment of tunneling, the tip and sample wave functions have to be replaced by spinors, and the problem of deriving an expression for the tunneling conductance involves a spinor transformation from the spin coordinate system of one electrode to the spin coordinate system of the other electrode, leading to the following expression for the total tunneling conductance G in the limit of small applied bias voltage:

$$G = 2\pi^2 G_0 (n_t^{\uparrow} n_s^{\uparrow} |M_{\uparrow\uparrow}|^2 + n_t^{\uparrow} n_s^{\downarrow} |M_{\uparrow\downarrow}|^2 + n_t^{\downarrow} n_s^{\uparrow} |M_{\downarrow\uparrow}|^2 + n_t^{\downarrow} n_s^{\downarrow} |M_{\downarrow\downarrow}|^2). \quad (17)$$

Here $n_{t,s}^{\uparrow,\downarrow}$ denote the spin-resolved densities of states for tip and sample, respectively, and $\{M_{\uparrow,\downarrow}\}$ are the tunneling matrix elements for transitions between the spin-dependent states of the tip and sample. Equation (17) can be simplified by introducing

$$n_t = n_t^{\uparrow} + n_t^{\downarrow}, \quad n_s = n_s^{\uparrow} + n_s^{\downarrow} \quad (18)$$

and

$$m_t = n_t^{\uparrow} - n_t^{\downarrow}, \quad m_s = n_s^{\uparrow} - n_s^{\downarrow}, \quad (19)$$

which yields

$$G = 2\pi^2 G_0 |M_0|^2 (n_t n_s + m_t m_s \cos\theta). \quad (20)$$

By defining

$$P_t = m_t/n_t, \quad P_s = m_s/n_s, \quad (21)$$

we finally obtain

$$G = 2\pi^2 G_0 |M_0|^2 n_t n_s (1 + P_t P_s \cos\theta). \quad (22)$$

We can easily see that Eq. (22) is an extension of Slonczewski's result [Eq. (4)] and that Eq. (22) reduces to the result of Tersoff and Hamann [Eq. (11)] if one of the electrodes, either the tip or sample, is nonmagnetic ($P_t = 0$ or $P_s = 0$). According to Eq. (22) the tunneling conductance in the magnetic case is expected to depend on the spin-resolved local density of states at the Fermi energy for both electrodes and on the cosine of the angle θ between the magnetization directions of tip and sample, similarly to the case of planar magnetic tunnel junctions (Fig. 5).

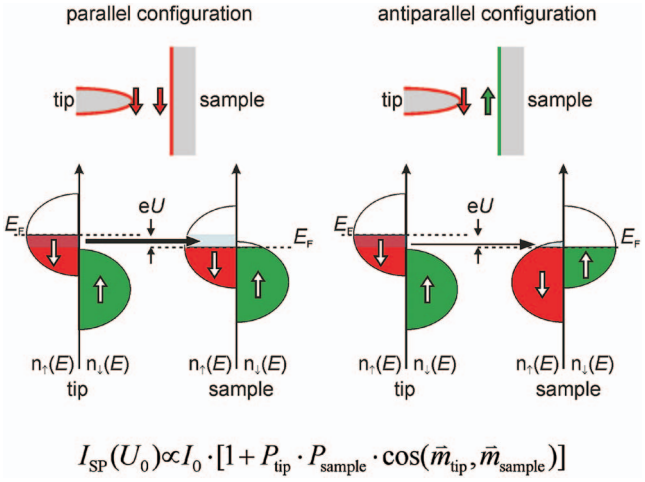

FIG. 5. (Color) Principle of spin-polarized scanning tunneling microscopy (SP-STM): the spin-polarized tunneling current flowing between a magnetic tip and a magnetic sample depends on the relative alignment of the local magnetization of tip and sample as well as on the spin polarization of the electronic states of tip and sample contributing to the tunneling current.

For the more general case of finite bias voltage, Wortmann *et al.* (2001) derived the following expression for the tunneling current I measured at the tip position $\vec{r}_0$ and with an applied bias voltage U:

$$I(\vec{r}_0, U, \theta) = I_0(\vec{r}_0, U) + I_{sp}(\vec{r}_0, U, \theta) = \frac{4\pi^3 C^2 \hbar^3 e}{\kappa^2 m^2} [n_t \tilde{n}_s(\vec{r}_0, U) + \vec{m}_t \tilde{\vec{m}}_s(\vec{r}_0, U)], \quad (23)$$

where n_t is the non-spin-polarized LDOS at the tip apex, $\tilde{n}_S$ is the energy-integrated LDOS of the sample, and $\vec{m}_t$ and $\tilde{\vec{m}}_s$ are the corresponding vectors of the (energy-integrated) spin-polarized (or magnetic) LDOS

$$\tilde{\vec{m}}_s(\vec{r}_0, U) = \int^{eU} \vec{m}_s(\vec{r}_0, E) dE, \quad (24)$$

with

$$\vec{m}_s = \sum \delta(E_\mu - E) \Psi_\mu^S(\vec{r}_0) \sigma \Psi_\mu^S(\vec{r}_0). \quad (25)$$

Ψ_μ^S denotes the spinor of the sample wave function

$$\Psi_\mu^S = \begin{pmatrix} \Psi_{\mu\uparrow}^S \\ \Psi_{\mu\downarrow}^S \end{pmatrix} \quad (26)$$

and σ is Pauli's spin matrix. As an important result, the spin-dependent contribution I_{sp} to the total tunneling current is found to scale with the projection of $\tilde{\vec{m}}_s$ onto $\vec{m}_t$, and therefore with the cosine of the angle θ between the magnetization directions of the two electrodes, in agreement with the limiting case of vanishing applied bias voltage [Eq. (22)].

The first experimental observation of vacuum tunneling with spin-polarized electrons based on the use of STM involving a magnetic tip and a magnetic sample was by Wiesendanger, Güntherodt, *et al.* (1990a, 1990b).

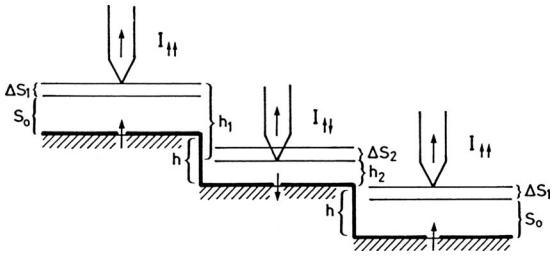

FIG. 6. Schematic of a ferromagnetic tip scanning over alternately magnetized terraces separated by monatomic steps of height h. An additional contribution of spin-polarized tunneling leads to the observation of alternating step height values $h_1=h+\Delta s_1+\Delta s_2$ and $h_2=h-\Delta s_1-\Delta s_2$. From Wiesendanger, Güntherodt, *et al.*, 1990a.

The spin dependence of the tunneling current was demonstrated using an ultrahigh-vacuum (UHV) STM setup (Wiesendanger, Bürgler, *et al.*, 1990; Wiesendanger, Anselmetti, and Güntherodt, 1990) with a ferromagnetic CrO_2 probe tip and a Cr(001) sample surface. The topological antiferromagnetic order of the Cr(001) surface with alternately magnetized terraces separated by monatomic steps (Blügel *et al.*, 1989) provided an ideal model system because the spatial variation in the direction of surface magnetization of a stepped Cr(001) sample is directly linked to the surface topography, thereby avoiding the need for an external magnetic field to change the sample's magnetization state. Figure 6 shows a ferromagnetic tip scanning over alternately magnetized terraces separated by monatomic steps of height h. If the magnetic tip were scanned at a constant distance s_0 from the sample surface, the tunneling current would alternate between $I_{\uparrow\uparrow}=I_0(1+P)$ and $I_{\uparrow\downarrow}=I_0(1-P)$, where P denotes the effective polarization of the tunnel junction given by

$$P=\frac{I_{\uparrow\uparrow}-I_{\uparrow\downarrow}}{I_{\uparrow\uparrow}+I_{\uparrow\downarrow}}. \tag{27}$$

However, if the SP-STM experiment is performed at a constant current, the feedback system has to adjust the distance of the tip from the sample surface accordingly; it is either $s_1=s_0+\Delta s_1$ or $s_2=s_0-\Delta s_2$, depending on the relative directions of magnetization of the tip and surface terrace. As a consequence, the measured monatomic step heights alternate between $h_1=h+\Delta s_1+\Delta s_2$ and $h_2=h-\Delta s_1-\Delta s_2$ (Fig. 6). In the low-bias limit, the following relationship between the effective polarization P, the measurable quantities $\Delta s=\Delta s_1+\Delta s_2$, and the local tunneling barrier height ϕ can be derived to a first approximation (Wiesendanger, Güntherodt, *et al.*, 1990a):

$$P=\frac{\exp(A\phi\Delta s)-1}{\exp(A\phi\Delta s)+1}, \tag{28}$$

with $A=1.025\ \mathrm{eV}^{-1/2}\ \mathrm{Å}^{-1}$.

For SP-STM experiments with a finite bias voltage, the spin- and energy-dependent local density of states for tip and sample have to be taken into account. A model calculation of the effective spin polarization P for

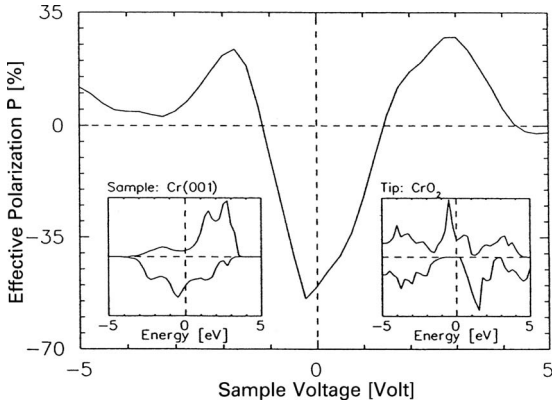

FIG. 7. Effective spin polarization of a CrO_2-vacuum-Cr(001) tunnel junction as a function of sample bias voltage. The insets show the spin-up (upper part) and spin-down (lower part) density of states of CrO_2 and the Cr(001) surface. From Wiesendanger, Bürgler, Tarrach, Wadas, *et al.*, 1991.

the CrO_2-vacuum-Cr(001) tunnel junction, performed assuming a simplified spin-dependent tunneling probability (Wiesendanger, Bürgler, Tarrach, Wadas, *et al.*, 1991), showed that P becomes strongly bias dependent and can even change its sign as a function of bias voltage (Fig. 7). If the spin-resolved LDOS of one electrode (e.g., the tip) were known, measuring the bias dependence of the effective spin polarization could provide information about the spin-resolved LDOS of the other electrode (e.g., the sample), leading to the method of spin-polarized scanning-tunneling spectroscopy (see Secs. III.B.2 and IV.A.3). Moreover, a distance-dependent behavior of the effective spin polarization is expected because the decay rates for s, p, and d states usually differ, resulting in different contributions to the effective spin polarization at different tip-surface separations (Alvarado, 1995).

While the first successful SP-STM experiments were performed on the nanoscale with relatively blunt CrO_2 tips, an improved magnetic tip preparation method (see Sec. III.A) soon led to atomic-scale spin contrast on a magnetite [Fe_3O_4(001)] surface (Wiesendanger, Shvets, *et al.*, 1992a, 1992b, 1992c). Observation of atomic-scale contrast between the two different magnetic ions Fe^{2+} and Fe^{3+} on the iron B sites within the FeO(001) planes of magnetite was attributed to the different spin configurations, $3d^{5\uparrow}3d^{\downarrow}$ for Fe^{2+} and $3d^{5\uparrow}$ for Fe^{3+}. While fluctuations of the $3d^{\downarrow}$ electrons among the iron B sites are rapid in the bulk at room temperature, the reduced coordination and band narrowing at the surface are likely to increase the metal-insulator (Verwey) transition for magnetite from the bulk value to well above room temperature, in agreement with the experimental results (Coey *et al.*, 1993; Wiesendanger *et al.*, 1994).

More recently, atomic-resolution spin contrast has been achieved on many different types of surfaces, including those of antiferromagnetic atomic layers of Mn(110) epitaxially grown on W(110) substrates (Heinze *et al.*, 2000; Bode *et al.*, 2007), antiferromagnetic Mn_3N_2(010) samples (Yang *et al.*, 2002), antiferromag-

netic atomic layers of Fe(001) epitaxially grown on W(001) substrates (Kubetzka *et al.*, 2005; Bode, Vedmedenko, *et al.*, 2006), and reconstructed Mn films grown on Fe(001) (Gao *et al.*, 2007). The experimental advances made SP-STM a routine technique for the investigation of magnetic surfaces and nanostructures down to the atomic level (Wiesendanger, 1994b, 2007; Wiesendanger and Bode, 2001; Bode, 2003; Wiesendanger *et al.*, 2004; Bode and Wiesendanger, 2005; Bode, Kubetzka, Pietzsch, and Wiesendanger, 2005; Wulfhekel, 2005; Schwarz *et al.*, 2007). Simultaneously, the theoretical modeling and simulation of SP-STM has made considerable progress (Heinze, 2006), making it an indispensable method for revealing noncollinear spin structures in systems of reduced dimensions (Bode *et al.*, 2007) and for investigating spin-current-induced magnetization switching in spatially resolved nanoscale structures (Krause *et al.*, 2007). An extension of SP-STM toward the field emission regime (Kubetzka, Bode, and Wiesendanger, 2007) allows for nanoscale magnetic imaging at large tip-sample separations, offering potential future applications of the SP-STM technique in magnetic recording.

III. PRINCIPLES AND EXPERIMENTAL METHODS OF SP-STM

In this section, we review the experimental requirements for successful operation of SP-STM, including the preparation of spin-sensitive probe tips and the various modes of operation of SP-STM. We also focus on the issue of getting quantitative results with respect to measurements of the local spin polarization.

A. Preparation of magnetic probe tips

The most delicate task for successful SP-STM measurements is the preparation of suitable probe tips offering simultaneously a high spatial resolution (down to the atomic level), a high spin polarization (thereby yielding a high signal-to-noise ratio), and a nondestructive magnetic imaging process. Furthermore, the control of the spin orientation at the tip apex is important for determining whether the in-plane or out-of-plane component of surface spins is imaged [according to Eq. (22)].

In the mid-1980s use of optically pumped GaAs tips was proposed for SP-STM experiments (Pierce, 1988), because GaAs optically pumped with circularly polarized light is a well established source for spin-polarized electrons. The main advantage of such probe tips would be that both the sign and the quantization axis of the polarization of photoexcited electrons can easily be controlled by appropriate choice of laser light helicity and experimental geometry, respectively (Laiho and Reittu, 1993, 1996, 1997). However, while several successful SP-STM experiments have been reported involving an optically pumped GaAs sample and a magnetic tip (Alvarado and Renaud, 1992; Sueoka *et al.*, 1993), the reversed configuration with a magnetic sample and an optically pumped GaAs tip has so far failed in providing convincing SP-STM results. The main reason for the failure might be a reduced spin injection efficiency and an insufficient lifetime of the spin carriers at the tip apex related to the tip's roughness (Shinohara *et al.*, 2000; LaBella *et al.*, 2001). Moreover, circular dichroic effects of nonmagnetic origin, caused either by the presence of dichroic spatial fluctuations in the sample's substrate (Nabhan *et al.*, 1999) or by the asymmetric shape of the probe tips (Vázquez de Parga and Alvarado, 1996; Anisimovas and Johansson, 1999), further complicate the analysis of experimental results obtained with optically pumped GaAs tips. Therefore, SP-STM activities currently almost exclusively involve the use of magnetic probe tips. For that reason, we focus on the preparation and use of magnetic probe tips in this review.

Different types of magnetic probe tip have been prepared and evaluated for SP-STM applications, (1) tips from bulk magnetic material (single-crystalline and polycrystalline wires, or amorphous metals), (2) nonmagnetic tips covered with an ultrathin film of magnetic material, and (3) nonmagnetic tips with a cluster of magnetic material at the front end. In most cases so far, 3*d* transition metals, rare-earth metals, or alloys of such materials have been used for SP-STM experiments. Since these materials are easily oxidized in an uncontrolled way when exposed to air, the final step of any tip preparation procedure has to be performed *in situ* in an ultrahigh-vacuum environment. It is an important topic of current research to evaluate various kinds of protective thin-film coatings which can prevent oxidation processes, while still allowing the probing of the wave function tails of the spin-polarized states by SP-STM through such a coating layer (Berbil-Bautista *et al.*, 2006).

1. Tips from bulk magnetic material

The *in situ* preparation of atomically sharp magnetic tips from polycrystalline wires of iron and chromium for SP-STM applications has been described by Wiesendanger, Bürgler, Tarrach, Schaub, *et al.* (1991). In the first step, the wires are electrochemically etched until a constriction is formed. Subsequently, the wires with narrow constrictions are introduced into the UHV STM. Finally, by making use of an *in situ* pulling procedure, very sharp and clean tips can be obtained, providing atomic resolution routinely. Tips prepared in this way first allowed spin-dependent STM imaging on an atomic scale (Wiesendanger, Shvets, *et al.*, 1992a, 1992b, 1992c; Koltun *et al.*, 2001).

Alternatively, the magnetic wires may be electrochemically etched until a STM tip is obtained (Shvets *et al.*, 1992; Murphy *et al.*, 1999; Cavallini and Biscarini, 2000; Albonetti *et al.*, 2002; Mariotto *et al.*, 2002; Ceballos *et al.*, 2003). However, in that case an *in situ* tip cleaning procedure in UHV, such as Ar^+ ion etching, has to follow in order to remove oxide and carbon-containing contamination layers from the tip and allow reproducible SP-STM experiments. When using ferromagnetic 3*d* transition metal tips made from bulk material a serious concern is their high saturation magnetization and the

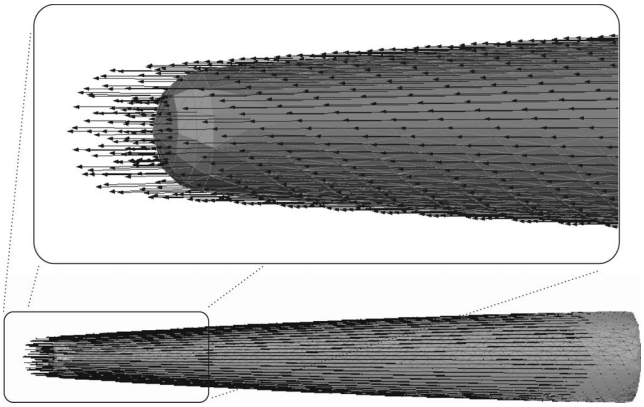

FIG. 8. Energetically lowest magnetic configuration of the end of a ferromagnetic amorphous metal tip. The inset shows the tip apex at higher magnification and reveals that the magnetization on the outer cone surface points along the tip axis. From Wulfhekel *et al.*, 2002.

resulting large magnetic stray fields from such tips. This restricts their application to ferrimagnetic and antiferromagnetic samples which are nearly insensitive to external magnetic fields. As an alternative, amorphous alloys with a low saturation magnetization, such as CoFeNiSiB, may be used for the preparation of SP-STM tips (Wulfhekel *et al.*, 2002). However, even such tips exhibit a residual magnetic stray field resulting from the nonvanishing magnetization, which usually is oriented along the tip axis because of shape anisotropy (Fig. 8). Therefore, SP-STM tips made from antiferromagnetic bulk materials, such as Cr or MnNi, are preferable for a nondestructive magnetic imaging process (Minakov and Shvets, 1990; Wiesendanger, Bürgler, Tarrach, Schaub, *et al.*, 1991; Murphy *et al.*, 1999; Mariotto *et al.*, 2002; Ceballos *et al.*, 2003). In this case, the spin contrast is determined by the spin state of the front atom at the tip apex (Fig. 9). It should be noted that a few uncompensated spins may still exist due to the microscopic roughness of a sharp tip, leading to a nonvanishing, but in most cases negligible residual dipolar stray field from antiferromagnetic SP-STM tips. On the other hand, blunt antiferromagnetic probes are not useful for magnetic tunneling because the contributions to the spin-polarized tunneling current from the two different spin sublattices of the antiferromagnet will cancel each other.

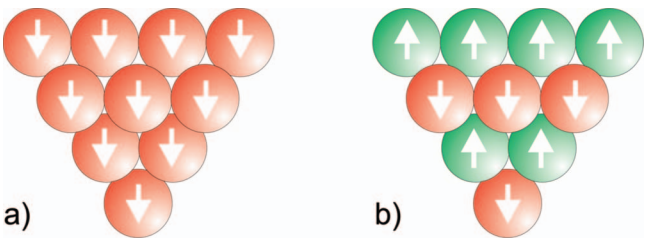

FIG. 9. (Color) Schematic of the apex of a ferromagnetic (a) and an antiferromagnetic tip (b). In both cases, the spin state of the front atom determines the spin contrast in SP-STM. However, only in the case of an antiferromagnetic tip can the disturbing influence of long-range magnetic stray fields be avoided.

In addition to achieving atomic resolution and nondestructive magnetic imaging, the spin contrast in SP-STM images has to be sufficiently high. While the measured spin polarization of tunneling electrons from Fe tips amounts to 40–45 %, only half of that value is typically measured for Cr tips. An optimum choice of materials for SP-STM with respect to the magnitude of the spin polarization for electronic states near the Fermi energy E_F would be half-metallic magnets (de Groot *et al.*, 1983; de Groot, 1991). These materials exhibit metallic behavior for one spin direction, while being insulators (or semiconductors) for the opposite spin direction. As a consequence, a spin polarization of 100% for the electronic states close to E_F can be expected. Several Mn-based Heusler alloys (XMnSb, where X=Ni, Co, Pt), CrO_2, and Fe_3O_4 are theoretically predicted to be half-metallic magnets. Indeed, the first successful SP-STM experiments were performed with CrO_2 tips (Wiesendanger, Güntherodt, *et al.*, 1990a) or Fe_3O_4 samples (Wiesendanger, Shvets, *et al.*, 1992a, 1992b). In order to reduce the magnetic stray field from ferromagnetic CrO_2 tips, thin films of CrO_2 on nonmagnetic Si substrates were prepared. After cleavage of the Si(111)-oriented substrates, sharp tips were obtained. Finally, the Si substrates were etched back, leading to overhanging CrO_2 thin-film tips. A subsequent *in situ* treatment of such tips in UHV led to reproducible SP-STM imaging conditions. However, the magnetic stray field even from a thin film of ferromagnetic material can lead to modifications of the sample's magnetization distribution, especially for magnetically soft materials or magnetic nanoparticles which are close to the superparamagnetic limit. Therefore, the ultimate SP-STM tip materials would be half-metallic antiferromagnets, which have been predicted theoretically (de Groot, 1991), but are still not available for routine SP-STM applications.

2. Nonmagnetic tips covered with an ultrathin film of magnetic material

Another direction toward reducing the magnetic stray field from SP-STM tips is the *in situ* preparation of magnetic thin film tips (Bode *et al.*, 1997; Bode, Getzlaff, and Wiesendanger, 1998). After electrochemical etching of a nonmagnetic tip (e.g., W, PtIr, Ir), it is introduced into a UHV system, where an *in situ* cleaning procedure by electron bombardment is applied. A high-temperature flash up to 2200 K removes oxides and other types of contamination resulting from the electrochemical etching, and provides a clean metallic tip. This is important for the subsequent thin-film deposition process because the evaporated magnetic layers adhere strongly to the tip only if the surface oxides have been removed completely. Otherwise, the magnetic layers are easily dropped off as the tip approaches the surface or during tip scanning. However, as a result of the high-temperature flash, the tip gets rather blunt, with a typical diameter of 1 μm, as shown in Fig. 10. If an ultrathin

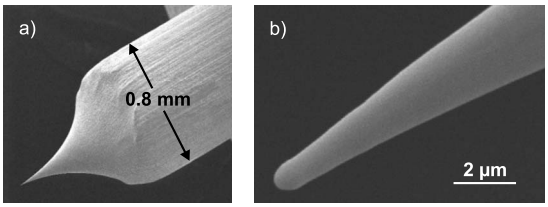

FIG. 10. Scanning electron micrograph of an electrochemically etched W tip after a high-temperature flash at $T>2200$ K at (a) medium and (b) higher magnification revealing a tip diameter of about 1 μm.

magnetic layer is deposited onto such probe tips, the direction of magnetization will be governed by the material-specific surface and interface anisotropies rather than by shape anisotropy as for tips made of a magnetic bulk material (Fig. 11). The reason is that the thickness of the deposited magnetic layer (typically 1–3 nm) is much smaller than the radius of the tip (1 μm). For instance, it is known from the field of thin-film magnetism that 3–10 monolayers (ML) of Fe on W(110) substrates exhibit a strong in-plane magnetic anisotropy, whereas 5–10 ML of Gd on W(110) exhibit an out-of-plane magnetic anisotropy at low temperatures, in agreement with experimental SP-STM results obtained with corresponding thin-film probe tips (Wiesendanger and Bode, 2001; Bode, 2003). Similarly, it was found that the magnetic behavior of Co-coated W(111) tips follows that of Co films prepared on flat W(111) substrates under similar conditions and in the same thickness regime (Bryl and Altman, 2003). By evaporation of a bilayer of 10 ML Au and a Co layer of variable thickness (4–10 ML) onto a clean W tip, both out-of-plane and in-plane spin-sensitive probes have been obtained, depending on the thickness of the Co layer (Prokop *et al.*, 2006). For a Co film thickness up to 8 ML, out-of-plane sensitivity is achieved, whereas thicker Co coverages lead to in-plane sensitivity. This result can be ascribed to a thickness-dependent reorientation transition of magnetic anisotropy for ultrathin Co layers on Au as is well known for the corresponding thin-fim system (Dreyer *et al.*, 1998). To enhance the spin polarization of thin-film probe tips, half-metallic magnets may be used as coating materials. For example, PtIr tips have been coated with a 300 nm thick manganite ($La_{0.7}Sr_{0.3}MnO_3$) film, which is expected to exhibit the characteristics of a half-metallic ferromagnet (Akiyama *et al.*, 2001).

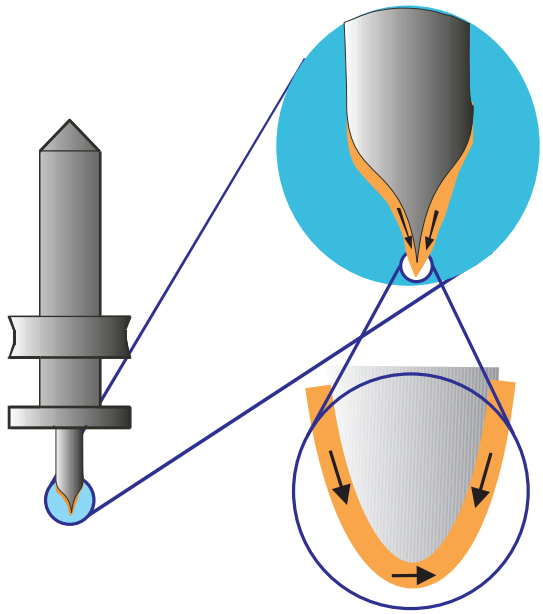

FIG. 11. (Color) Schematic of the magnetization distribution in magnetic thin-film tips, governed by magnetic interface anisotropy.

The main advantage of choosing ferromagnetic thin-film tips is that an additional external magnetic field can be used to force the tip magnetization out of the magnetic easy into the hard direction, thereby allowing both in-plane and out-of-plane sensitive SP-STM measurements with the same tip (Kubetzka *et al.*, 2005; Bode *et al.*, 2007). Moreover, it has been shown that the direction of spin sensitivity may simply be tuned by the applied bias voltage between tip and sample. This experimental result has been interpreted in terms of intra-atomic noncollinear magnetism at thin-film probe tips (Bode, Pietzsch, *et al.*, 2001).

A high lateral resolution of magnetic thin-film tips is typically gained by applying high bias voltages between tip and sample, leading to field-induced diffusion of atoms toward the tip apex where a tiny and sharp cluster is formed. Alternatively, one might pick up an atom or a small cluster from the surface which, due to a magnetic proximity effect, gains the same preferred magnetization direction as the magnetic thin film.

Unfortunately, even in the case of ultrathin ferromagnetic thin-film tips (e.g., 3 ML Fe on a W tip) the magnetic stray field can be sufficiently large to perturb the sample's magnetic structure, as observed experimentally for magnetic domain states of Fe nanowires (see Sec. IV.B) or for magnetic vortex states of mesoscopic Fe islands (see Sec. IV.C). The reason might be the existence of a small cluster at the tip apex. On the one hand, this is required to achieve high lateral resolution in SP-STM; on the other hand, such a small ferromagnetic cluster can be the origin of a sizable magnetic stray field. Therefore, in order to reduce the influence of the tip's stray field to a minimum, antiferromagnetic tip coating materials, such as Cr, are needed (Kubetzka *et al.*, 2002). Interestingly, it has been found that Cr-coated W tips exhibit a thickness-dependent reorientation transition of magnetic anisotropy such that W tips coated with 25–45 ML Cr exhibit out-of-plane sensitivity whereas W tips coated with ca. 100 ML Cr are in-plane sensitive. As a consequence, both out-of-plane and in-plane components of surface magnetization can be probed nondestructively with Cr-coated W tips (Wachowiak *et al.*, 2002).

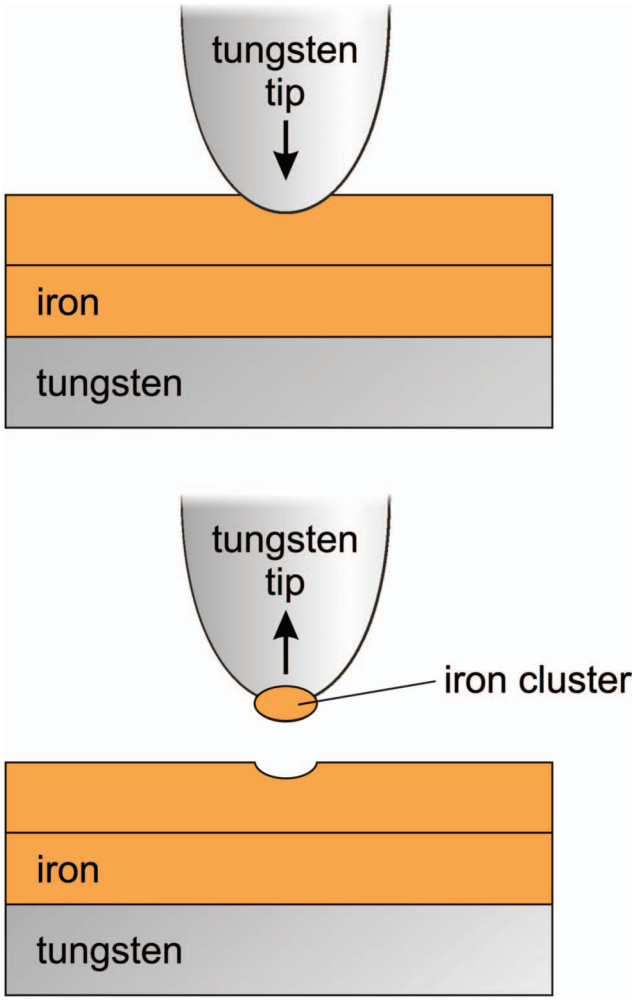

FIG. 12. (Color) Schematic of a simple preparation method for obtaining spin-sensitive probes. A nonmagnetic metallic tip is dipped into a magnetic sample and subsequently retracted. If the materials for tip and sample are chosen such that the magnetic sample material wets the tip, a stable SP-STM probe can be obtained.

3. Nonmagnetic tips with a cluster of magnetic material at the front end

The easiest method for preparing a magnetization-sensitive probe tip for SP-STM experiments might be the use of voltage pulses (e.g., 10 V, 60 μs), applied between a standard nonmagnetic STM tip (e.g., W, PtIr) and a magnetic sample (Yamada, Bischoff, Mizoguchi, and van Kempen, 2003). As a result of the large electric field applied, material can be transferred from the magnetic sample to the tip due to a field desorption process. Consequently, a magnetic cluster is obtained at the tip apex which can serve for spin-contrast imaging. The direction of magnetization for such a cluster may be changed by additional voltage pulses; however, it cannot be controlled as in the case of magnetic thin film-tips. Alternatively, a nonmagnetic metallic tip might be dipped into a magnetic sample by several nanometers and subsequently retracted (Fig. 12). If the magnetic material wets the tip nicely, a stable SP-STM probe with high spin contrast can be obtained (Berbil-Bautista *et al.*, 2007). These two preparation methods for spin-sensitive tips are much less demanding than the *in situ* deposition of magnetic thin films, particularly in cases where an appropriate thin-film deposition stage is not available in the STM system.

B. Modes of operation of SP-STM

In the past 20 years, several different types of operation modes for SP-STM have been developed which all offer advantages and disadvantages, depending on the particular type of application. In the following, the three most commonly used modes of SP-STM operation are presented together with a critical judgment of their range of applicability.

1. Constant-current mode

Since its invention, constant-current imaging has been the most important operation mode of STM (Binnig and Rohrer, 1987). A feedback circuit drives the z component of the STM's piezoelectric actuator such that the tunneling current flowing between tip and sample remains constant while the tip is scanned over the surface by means of the actuator's x and y components. When magnetic tips and magnetic samples are used, the measured tunneling current can be decomposed into spin-averaged and spin-dependent contributions, according to Eq. (23). Surprisingly, it has been shown that the simple constant-current mode is capable of providing the ultimate resolution in magnetic imaging (Wortmann *et al.*, 2001). For a sample surface with two-dimensional (2D) translational symmetry, variation in the tunneling current ΔI can be written in terms of a 2D Fourier expansion with respect to the reciprocal surface lattice vectors $\vec{q}_{\parallel}^{\,\mathrm{n}}$,

$$\Delta I(\vec{r}_{\parallel},z,U,\theta)=\sum_{n\neq 0}\Delta I_{\vec{q}^{\,\mathrm{n}}}(z,U,\theta)e^{i\vec{q}^{\,\mathrm{n}}\cdot\vec{r}}, \tag{29}$$

where $\Delta I_{\vec{q}_{\parallel}^{\,\mathrm{n}}}(z,U,\theta)$ are the tip-sample distance-dependent expansion coefficients. The coefficients decay exponentially with increasing length of the reciprocal lattice vectors, and therefore the STM image is primarily dominated by the smallest nonvanishing reciprocal lattice vector $\vec{q}_{\parallel}^{\,(1)}$. Since any magnetic superstructure leads to larger periodicities in real space compared to a nonmagnetic state, the corresponding reciprocal lattice vectors become smaller than those related to the structural unit cell. As a consequence, the expansion coefficients for the spinpolarized contribution to the tunneling current become exponentially larger than those of the nonpolarized part. A constant-current SP-STM image thus reflects the magnetic superstructure rather than the atomic structure. This is true even in the case of a small effective spin polarization or in the case of a small angle θ between the directions of magnetization of tip and sample, i.e., $\cos\theta \ll 1$.

Historically, the constant-current mode of SP-STM was the first one introduced (Wiesendanger,

Güntherodt, *et al.*, 1990a). It was soon applied for atomic-resolution magnetic imaging of $Fe_3O_4(001)$ surfaces, using the preferential imaging of a large magnetic unit cell by spin-sensitive tips (Fe) in contrast to the smaller structural unit cell, as probed by nonmagnetic W tips (Wiesendanger, Shvets, *et al.*, 1992a, 1992b, 1992c). Similar observations on $Fe_3O_4(001)$ surfaces were also reported (Koltun *et al.*, 2001; Shvets *et al.*, 2004). The smallest magnetic unit cells imaged so far by the constant-current mode of SP-STM are those of single atomic layers of Mn epitaxially grown on W(110) (Heinze *et al.*, 2000) and single atomic layers of Fe epitaxially grown on W(001) (Kubetzka *et al.*, 2005), both in a 2D antiferromagnetic ground state. Further examples of atomic-scale SP-STM imaging of larger magnetic unit cells in the constant-current mode include the studies of $Mn_3N_2(010)$ surfaces (Yang *et al.*, 2002) and single atomic layers of Fe epitaxially grown on Ir(111) (von Bergmann, Heinze, *et al.*, 2006).

In addition to atomic-resolution investigations of collinear spin structures, the constant-current mode of SP-STM has recently found applications for revealing noncollinear spin structures, e.g., the spin structure of antiferromagnetic domain walls (Bode, Vedmedenko, *et al.*, 2006) or the spin spiral state of ultrathin Mn films (Bode, Heide, *et al.*, 2007). According to theoretical predictions (Wortmann *et al.*, 2001; Heinze, 2006), constant-current SP-STM imaging can be a powerful method to reveal even more complex noncollinear spin structures on the atomic scale.

While the constant-current mode of SP-STM is best suited for atomic-scale studies, it can also be applied to atomically flat surfaces of single crystals (Wiesendanger, Güntherodt, *et al.*, 1990a), nanowires (Kubetzka, Pietzsch, *et al.*, 2003a), and nanoscale islands (Rusponi *et al.*, 2005) without problems. However, the spin-sensitive imaging of rough surfaces at larger length scales is difficult using this type of operation mode because topographic features and magnetic structures might interfere. Another limitation of the constant-current mode results from the fact that the spin-polarized contribution to the tunneling current is sensitive only to the energy-integrated spin-polarized LDOS, according to Eq. (24). If a relatively large bias voltage U is applied between tip and sample, the energy integration can lead to a reduced spin-polarized tunneling current signal if the spin polarization of the relevant electronic states, contributing to the tunneling current, changes sign in the energy range between the Fermi level and eU (where e is the elementary charge). The latter limitation can be solved by operating the SP-STM in the spectroscopic mode.

2. Spin-resolved spectroscopic mode

The spectroscopic mode of (spin-averaged) STM was introduced in the mid-1980s in order to separate topographic and electronic structure information. The mode involves the measurement of the local differential tunneling conductance $dI/dU(U,x,y)$ as a function of bias voltage U and spatial coordinates x and y. Experimentally, a small modulation voltage U_{mod} is added to the applied bias voltage and the resulting tunneling current modulation is frequency- and phase-selectively detected by means of the lock-in technique. The amplitude of the bias voltage modulation determines the energy resolution of the spectroscopic measurement if thermal energy broadening is minimized by operating the STM at low temperatures.

Based on Eq. (16) and assuming a constant LDOS for the tip within the relevant energy range, the following expression for the local differential tunneling conductance can be derived:

$$\frac{dI}{dU}(U) \propto e n_t(0) n_s(eU) T(eU,eU) + \int_0^{eU} n_t(\pm eU \mp E) n_s(E) \frac{dT(E,eU)}{dU} dE. \tag{30}$$

At a fixed location, the increase in the transmission coefficient with applied bias voltage is smooth and monotonic. Therefore, structure in dI/dU curves as a function of U can usually be attributed to structure in the sample's local density of states via the first term of Eq. (30). However, interpretation of the spectroscopic data dI/dU as a function of position (x,y) is more complicated if the spectroscopic maps are obtained under constant-current conditions. In this case, the spatial variation in the transmission coefficient shows up in spatially resolved measurements of dI/dU as a background that is essentially an inverted constant-current topograph. Therefore, spectroscopic images corresponding to the spatial variation in dI/dU measured in the constant-current mode in fact contain a superposition of topographic and electronic structure information. To eliminate the influence of the z dependence of the transmission coefficient, the $dI/dU(U)$ curves have to be measured at a fixed tip-surface separation. This can be accomplished by a sample-and-hold amplifier used to gate the feedback control system alternately on and off while scanning the tip over the surface (Wiesendanger, 1994a).

Assuming that the second term in Eq. (30) is small, the spectroscopic mode provides direct access to the energy-resolved LDOS of the sample. In the case of a magnetic tip and a magnetic sample, additional spin resolution can be obtained with tunneling spectroscopy. In this case, the following expression for the local differential tunneling conductance can be derived from Eq. (23) (Wortmann *et al.*, 2001):

$$\frac{dI}{dU}(R_t,U) \propto n_t n_s(R_t,E_F+eU) + \vec{m}_t \cdot \vec{m}_s(R_t,E_F+eU). \tag{31}$$

As a result, the spin-polarized part of the differential tunneling conductance is directly proportional to the spin-polarized LDOS at the energy E_F+eU (within a very narrow energy interval δE, determined by the experimental energy resolution), whereas the spin-

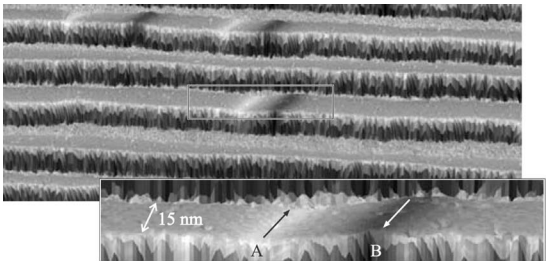

FIG. 13. Constant-current STM topograph colorized with the spin-resolved spectroscopic dI/dU signal, showing domain walls in Fe double-layer nanowires grown on a W(110) substrate (Kubetzka, Pietzsch, *et al.*, 2003a).

polarized tunneling current is proportional to the energy-integrated spin-polarized LDOS. Therefore, the spectroscopic mode of SP-STM is particularly useful in cases where spin-polarized tunneling into a special electronic state (e.g., a highly spin-polarized surface state) at a particular energy is intended in order to make simultaneous use of a large tunneling conductance and a high spin polarization (Bode, Getzlaff, and Wiesendanger, 1998; Kleiber *et al.*, 2000).

It should be noted that the spin-polarized LDOS not only changes its magnitude but may also change its sign as a function of energy. For instance, the sample surface and the tip may exhibit a positive spin polarization for some energy interval and a negative spin polarization for another one (Bode, Getzlaff, and Wiesendanger, 1999; Wiesendanger, Bode, and Getzlaff, 1999). As a consequence, a high dI/dU signal does not necessarily imply that the magnetization directions of both electrodes are parallel, but rather that the spin-polarized LDOSs of both electrodes have the same sign for a given energy.

In principle, the spin-resolved spectroscopic $dI/dU(U)$ signal can be measured simultaneously with and independently from the constant-current topographs, thereby allowing a separation of atomic and magnetic structure information. However, as in spin-averaged tunneling spectroscopy, it is important that the spin-resolved tunneling spectra are recorded at constant tip-surface separation rather than at a constant tunneling current. Under constant-current conditions the tip-sample distance generally varies with the direction of the sample surface magnetization because this distance is controlled by the tunneling current which itself scales with the term $\cos\theta$. An illustration of this behavior is given in Fig. 13, where a constant-current image of magnetic domain walls in Fe nanowires, colorized with the spin-resolved spectroscopic signal dI/dU, is presented. The tip approaches the surface at the position of domain wall A and retracts at the position of domain wall B. As a result, an apparent topographic depression arises at the position of the wall, exhibiting a high spin-dependent dI/dU signal, whereas an apparent topographic elevation is visible at the position of domain wall B, exhibiting a low spin-dependent dI/dU signal. In conclusion, spin-resolved spectroscopic dI/dU measurements should be performed at constant tip-surface separation with the z position of the tip stabilized at a bias voltage U_0 that assures that the spin-polarized part of the tunneling current for this particular bias vanishes, i.e., $I_{sp}(U_0)=0$.

Based on Eq. (31), a separation of the spin-averaged and spin-resolved contributions to the differential tunneling conductance is easy as long as the sample surface exhibits homogeneous electronic properties, because any spatial contrast variation arises from the spin-polarized part in that case. The spectroscopic imaging mode offers a convenient and direct way of imaging magnetic domains over large surface areas at high spatial resolution. For sample surfaces with an inhomogeneous electronic structure, a separation of electronic and magnetic structure information can be achieved by comparing two simultaneously recorded dI/dU images, one obtained with a bias voltage where the spin asymmetry defined by

$$A = \frac{dI/dU_{\uparrow\uparrow} - dI/dU_{\uparrow\downarrow}}{dI/dU_{\uparrow\uparrow} + dI/dU_{\uparrow\downarrow}} \tag{32}$$

becomes zero (electronic contrast image) and a second one obtained with a different bias voltage where the spin asymmetry is maximum (magnetic contrast image).

As in the constant-current mode of operation, the spectroscopic mode of SP-STM also offers atomic-scale spatial resolution, as first demonstrated by resolving antiferromagnetically ordered atomic layers of Fe epitaxially grown on W(001) (Kubetzka *et al.*, 2005).

3. Modulated tip magnetization mode

A third alternative mode of SP-STM operation, aiming at a separation of electronic and magnetic structure information, was introduced by Wulfhekel and Kirschner (1999). In analogy to earlier spin-polarized tunneling experiments performed with a stationary (nonscanned) Ni probe tip (Johnson and Clarke, 1990), a tiny coil was used for periodically switching the tip magnetization back and forth (Fig. 14). If the modulation frequency exceeds the cutoff frequency of the feedback loop, the measured signal in this modulated tip magnetization mode becomes proportional to the local magnetization of the sample, as can be derived easily from Eq. (23),

$$\frac{dI}{d\vec{m}_t}(\vec{r}_0) \propto \vec{m}_s(U). \tag{33}$$

Although this mode of operation can effectively separate topographic and electronic from magnetic contrast effects for a given sample bias, it should be noted that the spin-polarized LDOS is not constant, but changes magnitude as well as sign as a function of energy. Therefore, the spin polarization of the tunneling current and thus the $dI/d\vec{m}_t$ signal may vanish although a local sample magnetization exists. As a consequence, as in the case of the spectroscopic SP-STM mode, the investigation of the bias dependence for the spin-polarized tunneling current is indispensable in the modulated tip

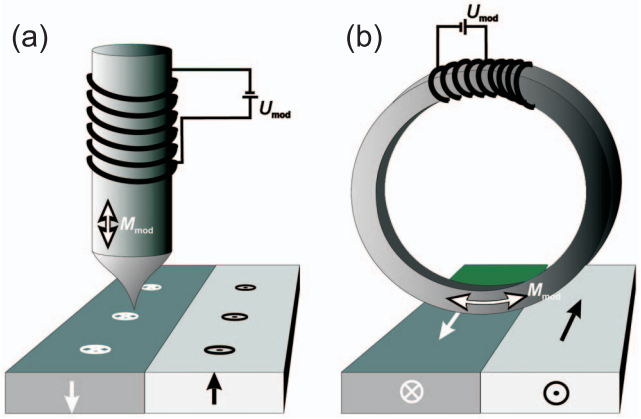

FIG. 14. (Color) Schematic experimental setup for modulated tip magnetization mode measurements with (a) an out-of-plane-sensitive magnetic tip and (b) an in-plane-sensitive ring-shaped magnetic probe.

magnetization mode as well (Ding, Wulfhekel, Bruno, and Kirschner, 2003). Furthermore, a dependence of the measured signal on the tip-sample distance is also present in the modulated tip magnetization mode (Ding, Wulfhekel, Schlickum, and Kirschner, 2003).

By developing two different kinds of experimental setup [Figs. 14(a) and 14(b)], it has become possible to probe both out-of-plane and in-plane components of the sample magnetization, making use of the modulated tip magnetization mode of operation. However, this approach appears to be highly demanding and time consuming compared to the use of magnetic thin-film tips, for which the direction of spin sensitivity can easily be controlled by the choice of coating material or coating thickness, or even by applying an external magnetic field without changing the tip at all. Another limitation of the modulated tip magnetization mode is that ferromagnetic probe tips have to be used and their magnetic stray field can affect the local magnetization distribution (Wulfhekel *et al.*, 2000), particularly for magnetically soft samples or small magnetic islands and nanoparticles. This is especially true for the experimental setup shown in Fig. 14(a); it may be less severe in case of the experimental setup shown in Fig. 14(b) due to the closed-loop geometry.

Recently near-atomic resolution has been achieved on a reconstructed Mn film epitaxially grown on a Fe(001) substrate using the modulated tip magnetization mode and an experimental setup shown in Fig. 14(b) (Gao *et al.*, 2007). Therefore, all three different types of operation modes of SP-STM are able to provide unprecedented insight into magnetism at the atomic level.

C. Quantitative determination of the spin polarization

The quantitative determination of spin polarizations in spin-resolved vacuum tunneling experiments has been an important early issue of SP-STM (Wiesendanger, Güntherodt, *et al.*, 1990a, 1990c). If the constant-current mode of operation with a small applied bias voltage is chosen, the relationship between the measured spin polarization of the tunnel junction and the measured apparent height change Δs is described by Eq. (28),

$$P = \frac{\exp(A\phi\Delta s) - 1}{\exp(A\phi\Delta s) + 1}. \tag{28'}$$

In the low-bias limit, the spin polarization P of the tunnel junction may be written as a product of the spin polarizations P_t and P_s of tip and sample states close to E_F. In this case, the spin polarization of the sample can be obtained directly if the spin polarization of the tip has been determined independently. For example, a spin polarization of up to 22% was found for the Cr(001) surface based on constant-current SP-STM experiments (Wiesendanger, Güntherodt, *et al.*, 1990a, 1990c). Much higher values of spin polarization were found in constant-current SP-STM experiments on nanoscale Co islands grown on Pt(111) (Rusponi *et al.*, 2005).

In the general case of spatially inhomogeneous magnetic surfaces, the measured spin polarization will be a function of the spatial coordinates: $P(x,y)$. The measured spin polarization of the tunnel junction may depend on the tip-surface separation because different types of electronic states (s-, p-, and d-type states) with a different degree of spin polarization may have different characteristic decay lengths (Alvarado, 1995). Finally, different types of electronic states, exhibiting different degrees of spin polarization, will show up at different energies E; therefore the measured spin polarization of the tunnel junction will generally be a function of E.

The energy dependence of the measured spin polarization $P(E)$ of the tunnel junction has been studied in the spectroscopic mode of SP-STM (Bode, Getzlaff, and Wiesendanger, 1998; Wiesendanger, Bode, and Getzlaff, 1999), for which $P(E)=P(eU)$ can be expressed as follows:

$$P(eU) = \frac{dI/dU_{\uparrow\uparrow}(U) - dI/dU_{\uparrow\downarrow}(U)}{dI/dU_{\uparrow\uparrow}(U) + dI/dU_{\uparrow\downarrow}(U)}, \tag{34}$$

where $dI/dU_{\uparrow\uparrow(\uparrow\downarrow)}(U)$ is the intensity of the dI/dU signal measured for parallel (antiparallel) alignment of the magnetization directions of tip and sample. In favorable cases, the spin polarization of the tip may be independent of energy for a given range of applied bias voltages. Then the energy dependence of the measured spin polarization can be ascribed to properties of the sample. For an Fe-coated tip and a Gd(0001) sample, it was found that within a relatively wide energy range of ±0.8 eV around the Fermi level E_F, the spin polarization P_t of the Fe-coated tip can indeed be assumed constant and on the order of 44% (Wiesendanger, Bode, and Getzlaff, 1999). A similar conclusion was drawn from a SP-STM study with an Fe-coated W tip and a Co(0001) sample (Okuno *et al.*, 2002). Under the assumption of a constant tip polarization P_t, the resulting energy dependence of the spin polarization of the Gd(0001) sample, as derived from spin-resolved tunneling spectroscopy experiments, agreed well with data obtained by spin-polarized inverse photoemission spectroscopy (Fig. 15).

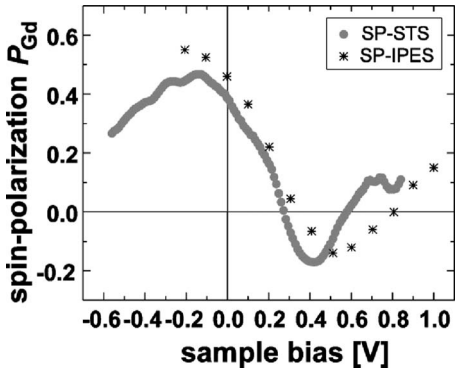

FIG. 15. Comparison of the energy dependence of the measured spin polarization on a Gd(0001) sample using two different techniques: spin-polarized tunneling spectroscopy with an Fe-coated thin film tip (Bode, Getzlaff, and Wiesendanger, 1998) and spin-polarized inverse photoemission spectroscopy (Donath *et al.*, 1996).

If there were a significant energy dependence of the spin polarization on the tip states, this level of agreement between the two techniques would not be achieved. Thus, Fe-coated thin-film probe tips, as introduced in Sec. III.A.2, are well suited for studying the energy dependence of the spin polarization of sample states.

The problem of a quantitative determination of the local surface spin polarization $P_s(x,y,E)$ as a function of energy has been addressed in more detail by Kubetzka, Pietzsch, *et al.* (2003a), based on calculations of the spin-polarized tunneling current for several model-type density-of-states distributions for the sample. A main conclusion is that quantification of spin-polarized tunneling spectroscopic data requires that it is obtained by measuring at a constant tip-surface separation and that the choice of the stabilization voltage U_0 assures a vanishing spin-polarized part of the tunneling current: $I_{sp}(U_0)=0$.

In general, the spin polarizations as determined with different experimental techniques (e.g., vacuum tunneling spectroscopy, tunneling spectroscopy based on planar junctions with oxide barriers, field-emission spectroscopy, and photoemission spectroscopy) can hardly be compared with each other because these techniques probe different electronic states at different energies, at different depths (with respect to the sample surface plane), or in a different environment.

IV. APPLICATIONS OF SP-STM

A. Magnetic domain and domain-wall structure of single crystals and thin films

An important application of SP-STM is the determination of magnetic domain and domain-wall structures at high spatial resolution (<10 nm), a length scale inaccessible by other magnetic imaging techniques. Particularly for materials with a high magnetic anisotropy as well as for low-dimensional systems (quasi-2D films, quasi-1D nanowires, and nanoislands) the width of magnetic domain walls narrows down to a single-digit nanometer scale and can be resolved only by SP-STM at present.

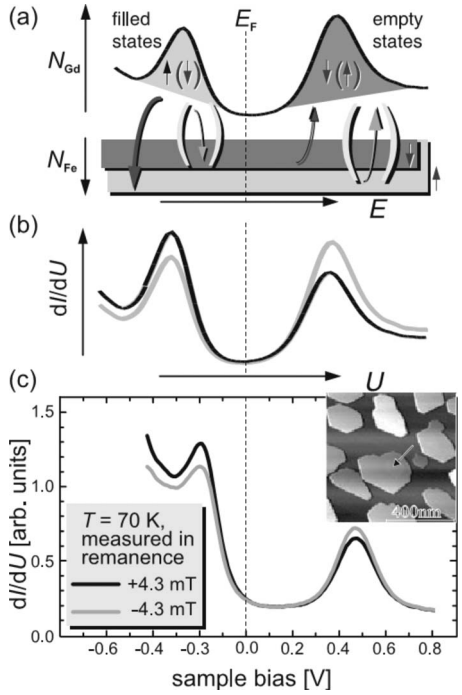

FIG. 16. Application of the spectroscopic mode of SP-STM. (a) Spin-resolved local density-of-states (LDOS) diagram for a tunnel junction with a rare-earth metal (0001) surface, exhibiting a spin-split electronic state close to E_F, and an Fe-coated tip with a constant spin-resolved LDOS. Due to spin-dependent tunneling, the differential tunneling conductance will be enhanced (reduced) at a bias voltage which corresponds to the energy of the surface state spin component parallel (antiparallel) to the tip's preferred spin direction (b). This leads to a reversal in the magnitude of the spin-dependent dI/dU signal at the energies of the peak positions of the spin-split surface state upon magnetic switching of the sample by an external applied magnetic field. (c) This type of behavior was observed in the spin-resolved tunneling spectra measured with an Fe-coated tip above a Gd(0001) island. From Bode, Getzlaff, and Wiesendanger, 1998.

1. Ferromagnetic rare-earth metal films

Rare-earth metals are highly reactive and thus surfaces of rare-earth single crystals are difficult to clean. It is therefore advantageous to prepare thin films of rare-earth materials under UHV conditions and to study their magnetic domain structure *in situ* by SP-STM. Thin films of rare-earth metals with (0001)-oriented surfaces can be grown on clean W(110) substrates. Due to the existence of a spin-split d_{z^2}-like surface state close to the Fermi level, the rare-earth (0001) surfaces are ideal model systems for the application of SP-STM (Bode, Getzlaff, and Wiesendanger, 1998; Getzlaff, Bode, and Wiesendanger, 1999; Krause *et al.*, 2006; Berbil-Bautista *et al.*, 2007). The spectroscopic mode of SP-STM was first demonstrated using a Gd(0001) film prepared in the Stranski-Krastanov growth mode (Fig. 16). The magni-

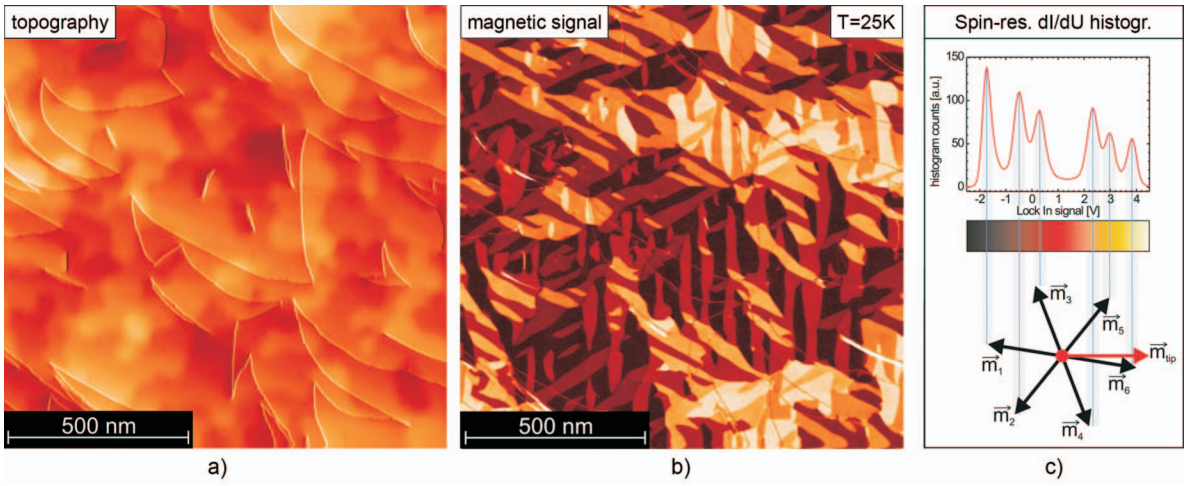

FIG. 17. (Color) Application of SP-STS for magnetic domain imaging with subnanoscale spatial resolution: a thin Dy(0001) film (90 ML) grown epitaxially on a W(110) substrate (a) exhibits a domain structure (b) with six different in-plane orientations of the local magnetization. (c) The six different contrast values in the SP-STM image result from the six different projections of the local sample magnetization onto the local magnetization direction (quantization axis) of the Dy probe tip. From Krause *et al.*, 2006.

tude of the exchange splitting was studied as a function of temperature for Gd(0001), Tb(0001), and Dy(0001) surfaces by means of variable-temperature STS (Bode, Getzlaff, *et al.*, 1998, 1999; Getzlaff *et al.*, 1998; Berbil-Bautista *et al.*, 2007). Spatially resolved SP-STM studies were performed on surfaces of Gd(0001) and, more recently, Dy(0001) thin films. Figure 17 shows simultaneously recorded topographic and magnetic maps of a Dy(0001) thin film grown layer-by-layer on a W(110) substrate. While the constant-current STM topograph in Fig. 17(a) reveals a relatively smooth surface structure with atomically flat terraces together with a few surface steps and some dislocations, the spectroscopic SP-STM image in Fig. 17(b) shows the magnetic domains with sharp transitions (magnetic domain walls) between them. Since the magnetic anisotropy of the Dy film is in plane, an in-plane-sensitive magnetic probe tip had to be used in order to achieve a high spin contrast. Both Cr- and Dy-coated W tips were successfully applied. A conventional spectroscopic STM image obtained with a nonmagnetic W tip showed no domain contrast at all.

The observed six different contrast levels in the magnetic SP-STM image of Fig. 17(b) result from the six equivalent in-plane directions of the local sample magnetization reflecting the sixfold symmetry of the underlying hexagonal crystal lattice structure of the Dy film. For a given tip magnetization direction (quantization axis) this leads to six different projections [described by the cosine function, reflecting the dependence of the spin-polarized tunneling current on the angle between the tip and sample magnetization directions; see Eq. (22)], which can be identified in the histogram of the measured values of the spin-resolved dI/dU signal across the entire image [see Fig. 17(c)]. The very sharp transitions between the observed magnetic domains result from the relatively high magnetic anisotropy k of the Dy film leading to very narrow domain walls, according to

$$w = 2(A/k)^{1/2}, \tag{35}$$

where w is the width of the domain wall and A is the exchange stiffness. Figure 18 shows a spectroscopic SP-STM image of a 60 ML thick Dy(0001) film as obtained with a Cr-coated W tip. Various types of domain walls (60°, 120°, and 180° walls) are observed, which are identified as Néel walls having widths of 2–5 nm (Berbil-Bautista *et al.*, 2007).

2. Ferromagnetic transition-metal single crystals and thin films

Surfaces of the ferromagnetic transition metals Co and Fe have been studied intensively by SP-STM. Figure 19 shows an example of a SP-STM image of the magnetic domain structure at the Co(0001) single-crystal surface as obtained using the modulated tip magnetization mode (dI/dm_T image). While Co has hcp structure, similar to Dy described above, the uniaxial magnetic anisotropy points along the c axis, i.e., perpendicular to the

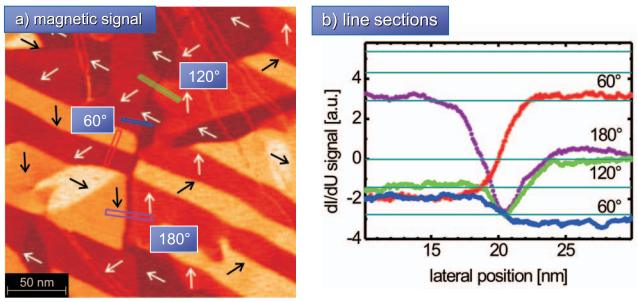

FIG. 18. (Color) Determination of magnetic domain wall widths. (a) Magnetization distribution of a 60 ML Dy(0001) film as measured with a Cr-coated W tip. The relatively high magnetic anisotropy of Dy leads to narrow magnetic domain walls of typically 2–5 nm width, as deduced from the corresponding line sections (b). From Berbil-Bautista *et al.*, 2007.

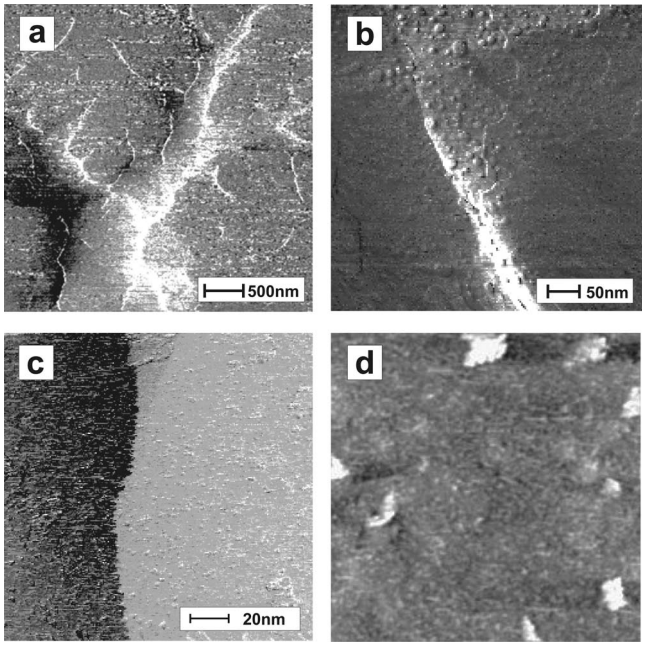

FIG. 19. SP-STM images (dI/dm_T signal) of the dendriticlike magnetic structure on a Co(0001) single-crystal surface at different length scales: (a) fractal-like domain-wall structure at large scale, (b) the end of a branch with a wall-like feature, and (c) detail of a sharp domain wall. (d) The corresponding topography of the same surface area as in (c). From Ding *et al.*, 2002.

(0001) surface plane, in contrast to Dy. However, in order to minimize the total energy, surface closure domains are formed with a magnetization that is locally tilted toward the surface plane, thereby reducing the dipolar energy contribution. A rather complex dendritic-type magnetic structure is formed at the surface with quite narrow branches. A domain-wall width of only $w = 1.1 \pm 0.3$ nm was observed at the very end of such narrow branches (Ding *et al.*, 2002).

Another characteristic spin structure occurs at surfaces of in-plane magnetized Fe(001) single-crystalline whiskers. In contrast to domain walls in Fe bulk samples, which exhibit a Bloch-like profile, a so-called Néel cap is formed at the Fe(001) whisker surface, i.e., the magnetization rotates within the plane in order to reduce the magnetostatic energy. Based on SP-STM images, obtained using the modulated tip magnetization mode, a domain-wall width of about 100 nm has been determined (Schlickum *et al.*, 2003).

Thin films (1–4 ML) of Fe(001) grown epitaxially on W(001) substrates have been studied in detail by SP-STS (von Bergmann, Bode, and Wiesendanger, 2004b; von Bergmann *et al.*, 2005; Bodea *et al.*, 2005). It was found that the Fe(001) films exhibit a fourfold magnetic anisotropy in the film plane. However, while the easy direction of magnetization is [110] for the second and third monolayers, it turns into the [100] direction for the fourth monolayer (von Bergmann, Bode, and Wiesendanger, 2004; von Bergmann *et al.*, 2005). This behavior leads to a rather complex magnetization distribution on the nanoscale, as shown in Fig. 20, and necessarily requires high-resolution magnetic imaging techniques in order to be observable. The width of magnetic domain walls in a 2 ML film of Fe on W(001) was found to be considerably reduced (by a factor of 3) when the wall is located at a surface step edge; this has been explained by the influence of step edges on the ferromagnetic exchange and magnetic anisotropy (Bodea *et al.*, 2005). In contrast to the second, third, and fourth layers of Fe on W(001), the first layer was found to exhibit an out-of-plane magnetic anisotropy and an antiferromagnetically ordered state (Kubetzka *et al.*, 2005; von Bergmann *et al.*, 2005). The corresponding atomic-resolution SP-STM data are presented in Sec. IV.D.

SP-STM has also been applied to study the magnetic domain structure of thick polycrystalline Ni (Wulfhekel and Kirschner, 1999) and thin nanocrystalline Fe films (Wiesendanger and Bode, 2001). In the second case, high-resolution spectroscopic SP-STM data allowed the visualization of single-domain and multidomain states of nanoscale Fe grains within the film (Fig. 21). Narrow domain walls with a width of 2–3 nm were observed in

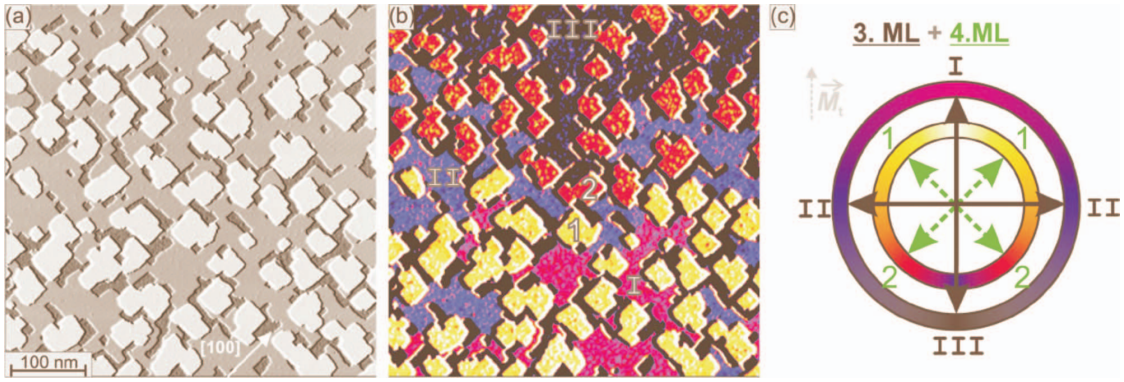

FIG. 20. (Color) Thin film of 3.2 ML Fe on W(001) grown at a temperature $T \sim 525$ K. (a) Constant-current STM topograph showing that patches of 2, 3, and 4 ML Fe on W(001) are exposed at the surface. (b) Simultaneously measured spin-resolved dI/dU map showing three magnetic contrast levels (I–III) on the third monolayer and two magnetic contrast levels (1, 2) on the fourth monolayer. The derived magnetization axes for the third and fourth monolayers are sketched in (c). From von Bergmann, Bode, and Wiesendanger, 2004.

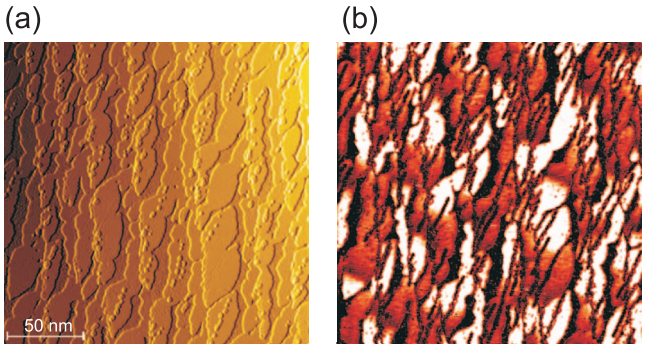

FIG. 21. (Color) Application of SP-STM to nanocrystalline thin films. (a) STM topograph and (b) spectroscopic SP-STM image of a nanocrystalline Fe film showing the correlation between magnetic and grain structure at subnanometer-scale spatial resolution.

multidomain Fe grains. A similar type of SP-STM studies applied to magnetic recording media may help to reveal the relationship between magnetic media noise and subnanometer-scale magnetic structure.

3. Antiferromagnetic single crystals and thin films

Magnetic domain observations in antiferromagnetic materials have been difficult in the past due to the limited number of experimental techniques, that are sensitive to domain states in antiferromagnetic crystals, and their limited spatial resolution. Of particular importance with respect to applications in metallic multilayer systems are the antiferromagnetic transition metals Cr and Mn, which exhibit quite complex spin structures.

For Cr a transverse spin-density-wave state exists below the Néel temperature T_N=311 K, whereas a longitudinal spin-density-wave state is present below the spin-flip temperature T_{SF}=121 K. The spin-density wave propagates along one out of three equivalent [001] directions, leading to ferromagnetically coupled spins within the (001) planes, but to an antiferromagnetic coupling between adjacent (001) planes. Although it was shown theoretically that even on a (001)-oriented surface of Cr the magnetic moments couple ferromagnetically and exhibit an enhanced value compared to the bulk moments (Fu and Freeman, 1986), no net magnetic moment could be found by spin-resolved photoemission (Klebanoff *et al.*, 1984). An explanation for this apparent discrepancy was given by the fact that real surfaces are not atomically flat but exhibit steps separating atomically flat terraces. As a consequence, different (001)-oriented terraces with opposite magnetization directions are exposed at the surface, leading to the so-called topological antiferromagnetism of the Cr(001) surface (Blügel *et al.*, 1989). Since the magnetization direction of a topological antiferromagnet alternates both laterally (terrace widths are typically on the order of 10–100 nm) and vertically [due to the antiferromagnetic coupling between (001) planes], all experimental methods with insufficient lateral resolution (>10 nm) or insufficient surface sensitivity (>1 ML) average over regions of opposite magnetization and therefore are unable to reveal the true magnetic state of the Cr(001) surface. SP-STM does not suffer from such limitations. Using the constant-current mode of SP-STM, Wiesendanger, Güntherodt, *et al.* (1990a) proved the existence of topological antiferromagnetism on the Cr(001) surface (see Sec. II.B.3).

Recently the spectroscopic mode of SP-STM was applied to reveal the magnetic state of the Cr(001) surface at various length scales (Kleiber *et al.*, 2000, 2002; Ravlic, Bode, Kubetzka, and Wiesendanger, 2003; Hänke, Bode, *et al.*, 2005; Hänke, Krause, *et al.*, 2005). The Cr(001) surface exhibits a highly spin-polarized d_{z^2}-like surface state of minority spin character close to the Fermi energy which can be exploited for high spin-contrast imaging by SP-STM. Since the amount of exchange splitting for the magnetic transition metals is higher than for the rare-earth metals, the majority spin component of Cr is located well above the Fermi level and is difficult to detect by tunneling spectroscopy. However, even in cases where only one component of an exchange-split electronic state is located within the energy range that is easily accessible by STS, high-contrast magnetic imaging is possible. As shown in Fig. 22(a) the intensity of the spin-resolved differential tunneling conductance signal at a bias voltage corresponding to the energy of the spin-polarized Cr surface state, as measured with an in-plane-sensitive Fe-coated probe tip, depends on the particular Cr terrace on which the tunneling spectrum was taken. The intensity of that spectroscopic peak was found to alternate between adjacent Cr(001) terraces that are separated by monatomic surface steps [Fig. 22(b)] which can be demonstrated by analysis of corresponding line sections over several terraces or by observation of spatially resolved SP-STS maps [Fig. 22(c)].

The local spin-resolved tunneling spectrum presented in Fig. 22(a) might suggest that the highest magnetic contrast in SP-STS images can be achieved with an applied bias voltage corresponding to the energy of the Cr(001) surface state. However, this is not true if the SP-STS images are obtained under constant-current conditions. If the stepped Cr(001) surface is scanned with a magnetic tip in the constant-current mode at a bias corresponding to the energetic position of the surface state, the tip-sample distance is increased (decreased) above Cr(001) terraces magnetized parallel (antiparallel) with respect to the tip. As discussed above and shown in Fig. 22(b), this variation in the tip-sample distance leads to a periodic alternation of the measured apparent step height values (Wiesendanger, Güntherodt, *et al.*, 1990a; Kleiber *et al.*, 2000). As a consequence, the variation in the spin-resolved differential tunneling conductance at that particular bias is strongly reduced for oppositely magnetized Cr(001) terraces. A high spin contrast in SP-STS images obtained under constant-current conditions can only be achieved if the spin polarization of the energy-integrated tunneling current differs from the spin polarization of the electronic states at the energy that corresponds to the applied bias voltage

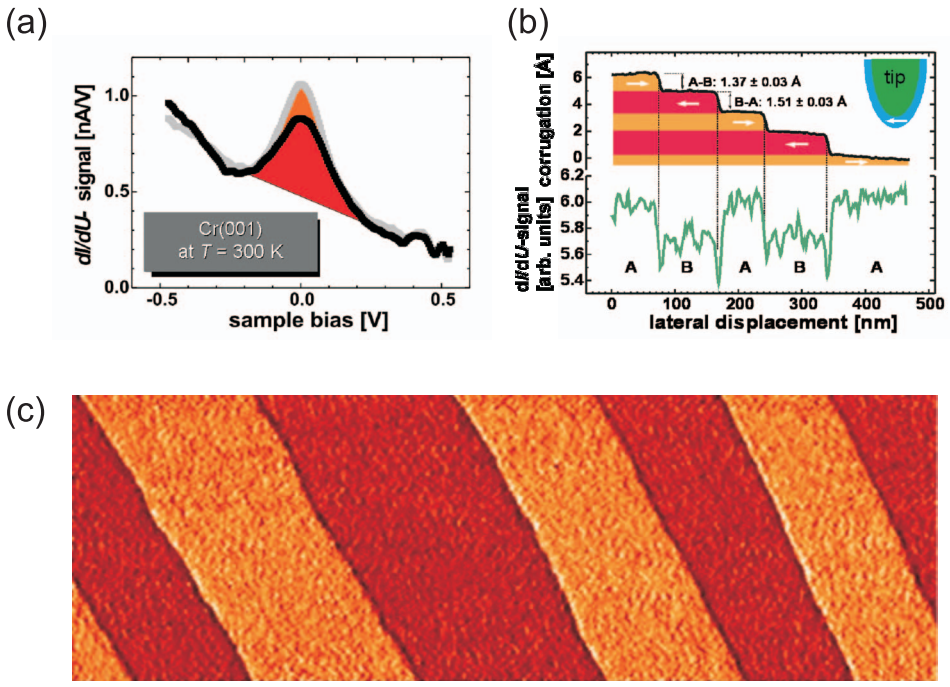

FIG. 22. (Color) Application of SP-STM to surfaces of antiferromagnets. (a) Spin-resolved differential tunneling conductance spectrum dI/dU measured with an Fe-coated W tip above differently magnetized terraces of a Cr(001) surface. A highly spin-polarized d_{z^2}-like surface state of Cr(001) close to the Fermi level provides a high spin-dependent dI/dU signal. (b) SP-STM line profiles measured in the constant-current mode reveal alternating step-height values whereas the spin-resolved spectroscopic dI/dU signal shows low and high levels, depending on the relative directions of magnetization of tip and surface terrace. (c) Spatially resolved spectroscopic SP-STM image (1000×300 nm^2) revealing the topological antiferromagnetic order of the Cr(001) surface. From Kleiber *et al.*, 2000, 2002.

U. For the case of Cr(001), a high spin contrast in SP-STS measurements performed under constant-current conditions was obtained at $U\sim\pm(250\pm50)$ mV.

While the magnetic structure of the Cr(001) surface exhibiting a series of monatomic steps is best described by the term topological antiferromagnet, the situation becomes more complex in the presence of screw dislocations, which are frequently observed at surfaces of Cr(001) single crystals (Wiesendanger and Güntherodt, 1990) and thin films (Kawagoe *et al.*, 2003, 2005). Figure 23(a) shows a SP-STS image of the Cr(001) surface exhibiting such a screw dislocation. The existence of a screw dislocation leads to topology-induced spin frustration in the vicinity of the dislocation core at the Cr(001) surface. As a result, the direction of surface magnetization has to turn by 180° in going around the screw dislocation, leading to a continuous change of contrast in the SP-STS image due to the cosine dependence of the spin-polarized tunneling conductance signal [Eq. (22)]. When two screw dislocations are close together in space, a domain wall is created at one screw dislocation and annihilated at the position of the second one [Fig. 23(b)]. The experimental observation that the domain wall connects two screw dislocations in a straight line can be explained by the lowering of the total energy obtained by minimizing the length of the wall (Ravlic, Bode, Kubetzka, and Wiesendanger, 2003). A line profile of the spin-resolved dI/dU signal across such a domain wall is shown in Fig. 23(c), which can be fitted with a tanh function that describes a 180° wall in the framework of micromagnetic theory (Hubert and Schäfer, 1998),

$$y(x)=y_0+y_{\mathrm{sp}}\tanh\left(\frac{x-x_0}{w/2}\right), \tag{36}$$

where $y(x)$ is the dI/dU signal measured at position x, x_0 is the position of the domain wall, w is the wall width, and y_0 and y_{sp} are the spin-averaged and spin-polarized dI/dU signals, respectively. Extracted values of the domain-wall widths on the Cr(001) surface range between 120 and 170 nm. These values are close to the domain-wall width found on the Fe(001) surface (see, Sec. IV.A.2). A large-scale view of the magnetization distribution at a Cr(001) surface exhibiting several screw and edge dislocations is shown in Fig. 24. Six SP-STS images, each 1 μm^2 in size, are shown together in order to increase the field of view and to demonstrate the reproducibility of the SP-STS imaging process in successive measurements. In principle, larger fields of view can be achieved by designing SP-STM setups with a high-sensitivity piezoelectric scanner for the tip and/or an x-y translation stage for the sample.

Topological antiferromagnetic order has also been observed for Mn(001) thin films grown epitaxially on Fe(001) substrates using either the spectroscopic mode (Yamada *et al.*, 2003a, 2003b; Yamada, Vázquez de Parga, *et al.*, 2005) or the modulated tip magnetization mode (Schlickum *et al.*, 2004; Wulfhekel *et al.*, 2005) of

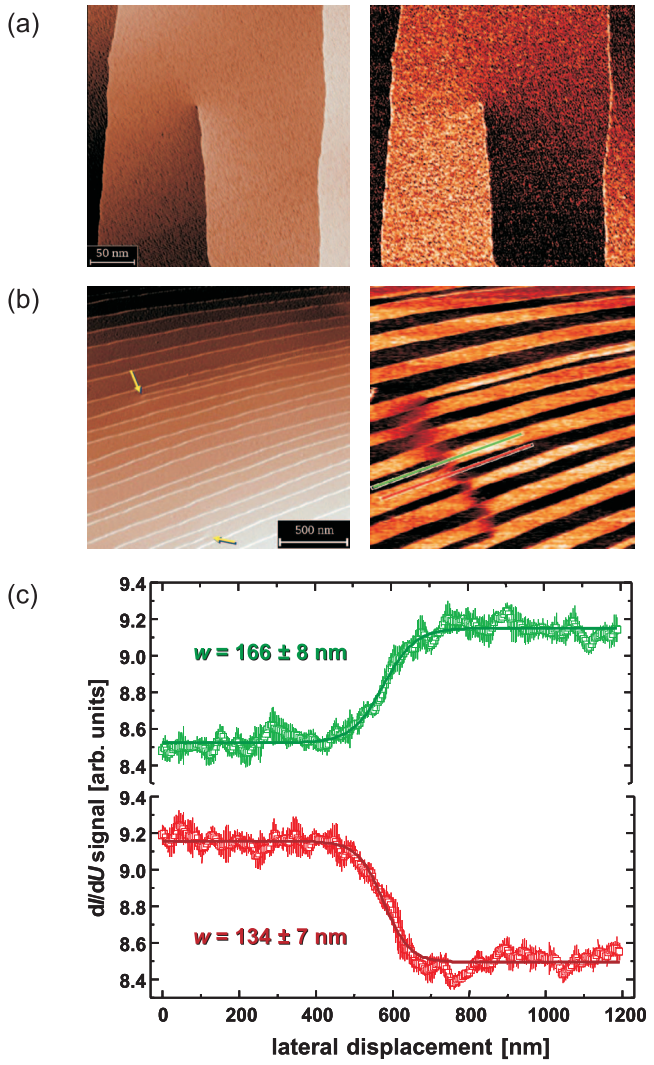

FIG. 23. (Color) Surface magnetic structure in the presence of defects. (a) STM topograph and spectroscopic SP-STM image of the Cr(001) surface revealing the magnetization distribution around a screw dislocation. (b) Large-scale STM and SP-STS images showing the presence of a domain wall connecting two screw dislocations. (c) Line profile across the domain wall observed in (b) yielding a domain-wall width of about 166 nm. From Ravlic, Bode, *et al.*, 2003.

SP-STM. A spin-polarized d_{z^2}-like surface state, located 0.8 eV above the Fermi energy, was also found to be responsible for the spin-dependent spectroscopic contrast (Yamada *et al.*, 2003b). Step-induced spin frustration, leading to the formation of topologically induced 180° walls, was studied as a function of the Mn film thickness. A linear increase in the wall width with Mn thickness was observed, which has been explained on the basis of the Heisenberg model (Schlickum *et al.*, 2004; Wulfhekel *et al.*, 2005).

While the Cr(001) and Mn(001) surfaces discussed above are ferromagnetic, an in-plane antiferromagnetic order is expected for differently oriented surface planes. In this case, in-plane atomic resolution is required in SP-STM measurements; this will be discussed in Sec. IV.D.

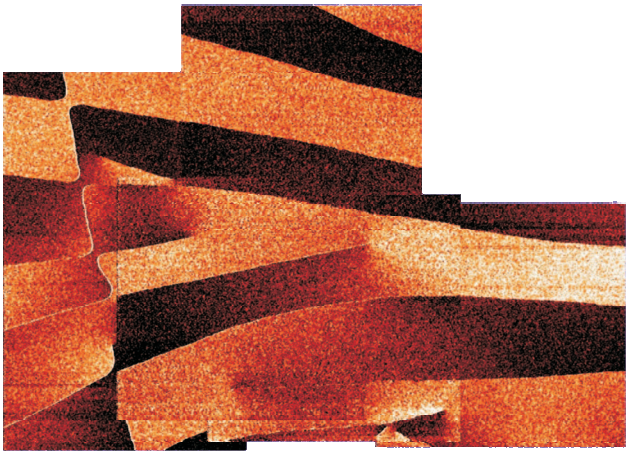

FIG. 24. (Color) Large-scale view of the topological antiferromagnet Cr(001) in the presence of screw and edge dislocations. Several SP-STS images, each 1 μm^2 in size, have been put together in order to reveal the magnetization distribution over an extended surface area and to show the degree of reproducibility of SP-STS imaging even when recording the data at room temperature as in the present case.

B. Magnetic domain and domain-wall structure of nanostripes and nanowires

Magnetic nanowires can be obtained by growth of magnetic materials on a twofold symmetric substrate, e.g., with a (110)-oriented surface plane. In the low-coverage regime ($\ll$1 ML), atomic wires may be formed either by strongly anisotropic surface diffusion or by the self-organization of atomic adsorbates with repulsive interaction (Pascal *et al.*, 1997). Alternatively, one might use the step-flow growth mode at elevated temperatures on a stepped substrate in order to prepare magnetic nanowires or nanostripes. In order to study the magnetic properties of such systems, a very high lateral resolution is necessarily required.

A particular interesting model system is provided by the growth of 1.4–1.8 ML Fe on a stepped W(110) substrate at elevated temperatures ($T\sim$520 K). In this coverage regime arrays of alternating double-layer and monolayer stripes of Fe can be obtained by step-flow growth. While the easy magnetization direction of the monolayer stripes is in plane, the double-layer stripes exhibit an out-of-plane magnetic anisotropy beyond a critical width that is determined by the exchange interaction (Elmers *et al.*, 1999). Due to magnetostatic interactions the double-layer stripes are antiferromagnetically coupled and therefore exhibit an alternating up-and-down magnetization direction. This is shown with the SP-STS image in Fig. 25(a) which was obtained with an out-of-plane-sensitive Gd-coated W tip at low temperatures (Pietzsch *et al.*, 2000a). A schematic picture of the magnetization and stray field distribution is shown in Fig. 25(b). In rare cases magnetic domain walls are observed along the narrow double-layer Fe nanostripes with a characteristic width which is comparable to the stripe width ($w\sim$6 nm). However, a significantly re-

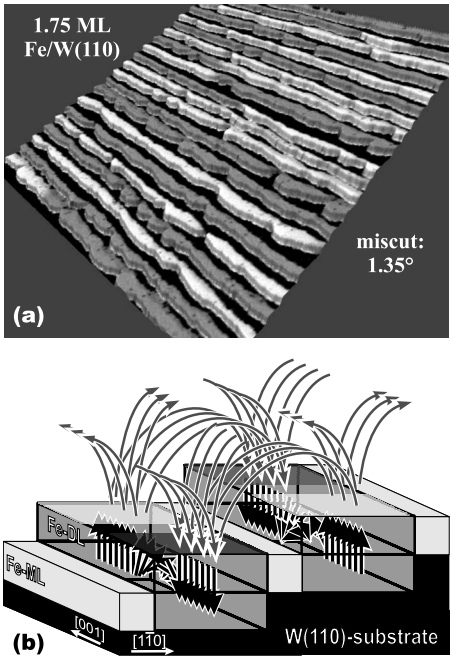

FIG. 25. Application of SP-STM to magnetic nanostripes. (a) Rendered perspective topographic STM image (200 $\times$200 nm^2) of narrow Fe nanostripes ($\sim$6–7 nm wide) prepared on a stepped W(110) substrate, grayscale coded with the spin-resolved spectroscopic dI/dU signal as measured with an out-of-plane-sensitive Gd-coated tip. A dipolar antiferromagnetic coupling between the Fe double-layer nanostripes leads to an alternating spin contrast. However, if two double-layer stripes are too close to each other, the exchange interaction leads to a ferromagnetic coupling. In some cases, narrow domain walls can be observed along the double-layer nanostripes. (b) Schematic of the perpendicularly magnetized double-layer Fe stripes exhibiting an antiparallel dipolar coupling in order to reduce the magnetic stray field of the array. Within the domain walls, the Fe double-layer nanostripes locally exhibit an in-plane magnetization. From Pietzsch *et al.*, 2000a; Bode, Kubetzka, *et al.*, 2001.

duced width ($w \sim 2$ nm) of the domain wall is observed when it is pinned at a structural constriction, in agreement with theoretical predictions (Bruno, 1999).

The response of an array of narrow magnetic nanostripes to an external magnetic field, i.e., a complete magnetic hysteresis cycle, has been measured using a SP-STM setup combined with a superconducting magnet system (Pietzsch *et al.*, 2000b). Since SP-STM is a near-field technique, it can be applied even in the presence of strong external fields, in contrast to conventional far-field electron microscopy. Individual processes of domain nucleation and domain-wall motion could be observed by SP-STS and directly correlated with the magnetic hysteresis loop obtained by counting the area of upward-magnetized stripe segments as a function of the external magnetic field strength (Pietzsch *et al.*, 2001).

If the width of the Fe double-layer stripes exceeds 10 nm, the reduction in the stray field is no longer accomplished by opposite magnetization directions of adjacent double-layer nanostripes but by a periodic reversal of the magnetization direction within every individual nanostripe (Fig. 26). Using an out-of-plane-sensitive Gd-coated W tip the domain structure of the perpendicularly magnetized double-layer Fe nanostripes can be visualized [Fig. 26(a)]. The dark lines observed on some of the stripes are caused by dislocation lines in the Fe double layer, which result from stress release in the pseudomorphically grown Fe film which is lattice mismatched to the W(110) substrate. No significant influence of the dislocation lines on the magnetic domain structure can be recognized. Using an Fe-coated W tip, sensitive to the in-plane component of surface magnetization, a domain-wall contrast image for this particular sample can be obtained [Fig. 26(b)]. Interestingly, the in-plane magnetization component within the domain walls also periodically alternates. Therefore, the magnetization state of the Fe double-layer stripes may be described by spin spirals in this case. It has been found experimentally that the chirality of these spin spirals is always the same. The determination of the sense of rotation (clockwise or counterclockwise) for the spin spirals requires control of the in-plane magnetization direction of the thin-film tips (Meckler, Gyamfi, *et al.*, 2009; Meckler, Mikuszeit, *et al.*, 2009).

The spin contrast as obtained in spectroscopic maps of the out-of-plane and in-plane magnetization components can be understood on the basis of the spin-resolved local tunneling spectra shown in Fig. 26(c). While the use of Gd-coated tips leads to a strong spin dependence of the measured differential tunneling conductance spectrum above the perpendicularly magnetized domains, the in-plane-sensitive Fe-coated tips are sensitive to the change in the magnetization direction within the domain-wall regions of the double-layer stripes (Bode, Kubetzka, Pietzsch, and Wiesendanger, 2002). Interestingly, it has been found that for particular values of the applied bias voltage even nonmagnetic W tips may allow the visualization of magnetic domain walls for the Fe double-layer stripes (Bode, Heinze, Kubetzka, Pietzsch, Nie, *et al.*, 2002; Pietzsch *et al.*, 2004b; Vedmedenko *et al.*, 2004). In this case, the contrast cannot be explained by spin-dependent tunneling but rather by a different local electronic structure above magnetic domain walls compared to the magnetic domain regions. A detailed analysis reveals that the spin-orbit-induced mixing between electronic states can depend on the local magnetization direction and therefore leads to differences in the LDOSs between domain and domain-wall regions that can be probed by spin-averaged STS (Bode *et al.*, 2003). However, no distinction between different in-plane directions of magnetization can be made using nonmagnetic W tips. On the other hand, the application of nonmagnetic tips for domain-wall imaging is very promising in view of a quantitative determination of domain-wall widths, excluding any kind of residual magnetic stray field influence from the tip.

The response of the array of multidomain Fe double-layer nanostripes to an external magnetic field has been studied by Kubetzka, Pietzsch, Bode, and Wiesendanger

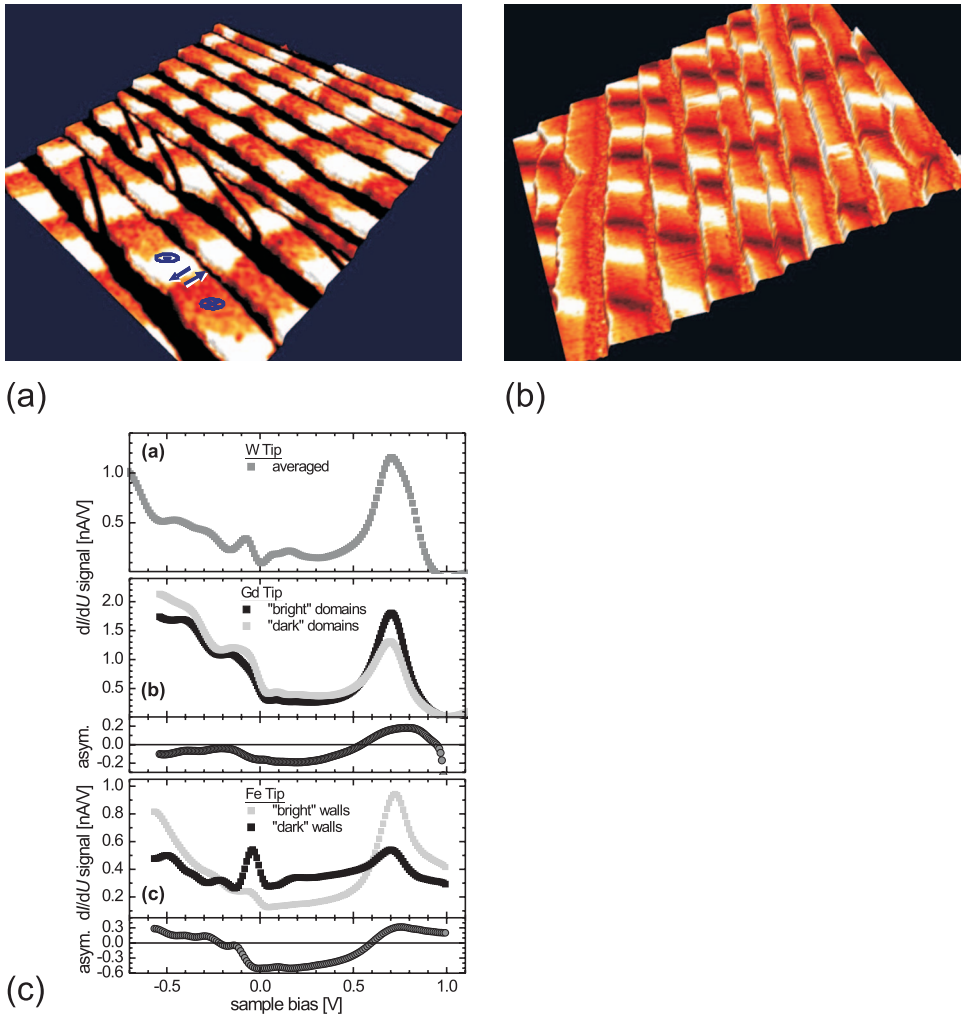

FIG. 26. (Color) Multidomain magnetic nanostripes. (a) Rendered perspective topographic STM image (200×200 nm^2) of ~15 nm wide Fe nanostripes prepared on a stepped W(110) substrate, color coded with the spin-resolved spectroscopic dI/dU signal as measured with an out-of-plane-sensitive Gd-coated tip. A characteristic magnetic domain structure with a typical domain size of 15×20 nm^2 can be observed. (b) Rendered perspective topographic STM image (200×200 nm^2) of ~15 nm wide Fe nanostripes prepared on a stepped W(110) substrate, color coded with the spin-resolved spectroscopic dI/dU signal as measured with an Fe-coated tip. In this case, a domain-wall contrast is achieved due to the sensitivity of Fe thin-film tips to the in-plane magnetization component. (c) Differential tunneling conductance spectra measured with a W tip, a Gd-coated tip, and an Fe-coated tip above Fe double-layer nanostripes exhibiting both out-of-plane and in-plane magnetization directions depending on the particular location. While the W tip is sensitive only to the change of electronic structure between the first and second layers of Fe on W(110), the use of Gd-coated tips as well as Fe-coated tips leads to a pronounced spin dependence of the measured tunneling conductance curves, particularly for a sample bias of $U=+0.7$ V. From Bode, Kubetzka, Pietzsch, and Wiesendanger, 2002.

(2003b). By increasing the magnetic field applied perpendicular to the sample surface plane, pairs of winding 180° walls are formed, finally resulting in 360° walls (Fig. 27). Their internal structure has been studied by analyzing line profiles across such walls, extracted from SP-STS data. The width of the observed 360° walls was found to be on the order of 7 nm.

If the Fe double layer is closed by depositing exactly 2 ML Fe on the W(110) substrate, a typical stripe domain phase along the [1–10] direction with a periodicity of about 50 nm is formed (Wiesendanger *et al.*, 2004). This stripe domain phase does not appear to be influenced neither by the presence of the monatomic steps of the tungsten substrate nor by the high density of dislocation lines in the Fe thin film (Fig. 28). Recently the magnetic characteristics of the dislocation lines in similar Fe thin films have been studied by SP-STS (Bode, von Bergmann, *et al.*, 2006). Furthermore, a coverage-dependent spin reorientation transition temperature of the Fe double layer on W(110) has been observed, i.e., the previously known transition from out-of-plane to in-plane magnetic anisotropy for the Fe double layer on W(110) as a function of temperature was found to occur at different transition temperatures depending on the Fe double-layer coverage (von Bergmann, Bode, and Wiesendanger, 2006).

In addition to the Fe double-layer nanostripes prepared on stepped W(110) substrates, the Fe monolayer

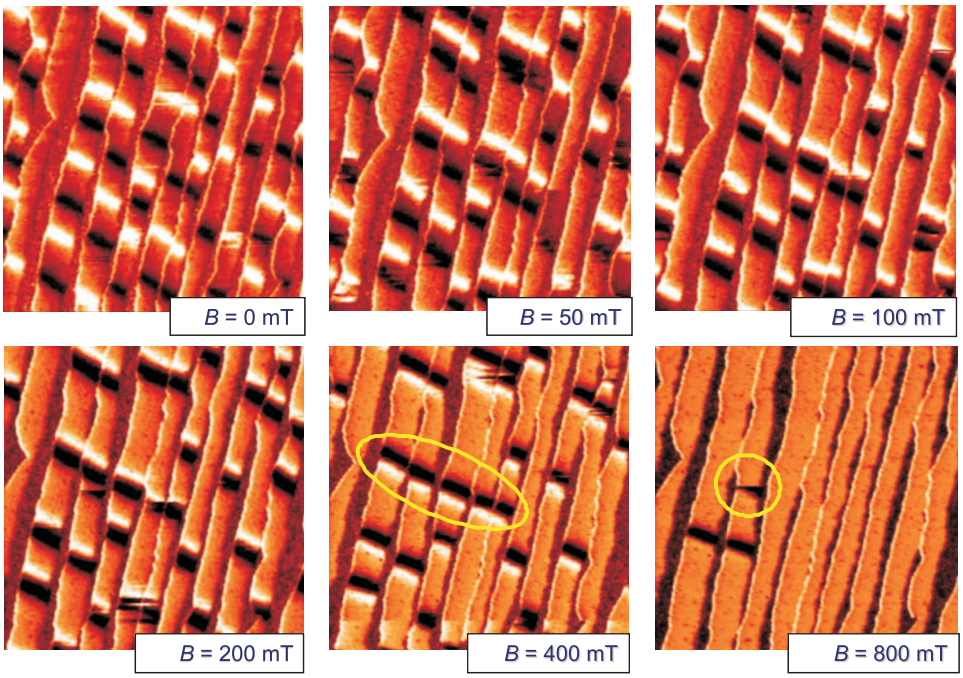

FIG. 27. (Color) Series of spin-resolved spectroscopic dI/dU maps (200×200 nm^2) of an array of multidomain Fe double-layer nanostripes obtained in an increasing perpendicular magnetic field. Pairs of 180° walls are gradually forced together, which is equivalent to the formation and compression of 360° walls. At a field of 800 mT, most of them have vanished, i.e., the Fe thin film is in magnetic saturation. From Kubetzka, Pietzsch, Bode, and Wiesendanger, 2003b.

nanostripes formed between them for coverages of 1–2 ML have been studied in detail by SP-STS as well (Pratzer *et al.*, 2001). Since the Fe monolayer on W(110) has a Curie temperature of $T_C=220$ K and an easy direction of magnetization in the film plane, the SP-STS measurements are performed with in-plane-sensitive tips at low temperatures. Figure 29(a) shows the domain structure of Fe monolayer stripes on a stepped W(110) substrate as measured with an Fe-coated W tip. Since the Fe coverage slightly exceeds 1 ML for this particular sample, there are also very narrow double-layer nanostripes present between adjacent monolayer stripes which appear dark in the SP-STS image. After zooming into a smaller sample region [Fig. 29(b)] the extreme sharpness of the domain walls in the Fe monolayer stripes is striking. The dark spots which are additionally visible on the Fe monolayer are caused by single impurities. Based on STM data the actual amount (1–2 %) of surface impurities is usually overestimated because a single impurity distorts the electronic structure of the sample surface with a decay length a factor of 2–3 larger than the actual size of the impurity (see Sec. IV.E). Since the SP-STS data of Fig. 29(b) simultaneously show domain walls of the very narrow Fe double-layer stripes together with the domain walls of the monolayer stripes, one can directly compare the measured widths of the domain walls for the first and second monolayer Fe nanostripes [Fig. 29(c)]. Based on the fitting function for domain walls within the framework of micromagnetic theory [Eq. (36)], one can derive a wall width of $w_{\mathrm{DL}}=3.8\pm0.2$ nm for the very narrow Fe double-layer nanostripe and a wall width of $w_{\mathrm{ML}}=0.6\pm0.2$ nm for the Fe monolayer stripes. Interestingly, the Fe monolayer stripes exhibit the sharpest domain walls ever observed in a ferromagnetic system. According to Eq. (35), this extreme sharpness of the observed domain walls can be ascribed to a very high value of the magnetic anisotropy k for the first monolayer Fe on W(110), about three orders of magnitude larger than the Fe bulk value, and a small value of the exchange stiffness A of the ML, about one order of magnitude lower than the Fe bulk value (Pratzer *et al.*, 2001). Since the measured width of the domain wall for the 1 ML of Fe on W(110) approaches the atomic scale, one might ask if the measured width of the domain wall is intrinsic or whether instrumental broadening effects have to be considered. Since the SP-STS data presented in Fig. 29 were obtained with a relatively small tunneling current ($I=0.8$ nA) and a relatively large bias voltage ($U=130$ mV), the Tersoff-

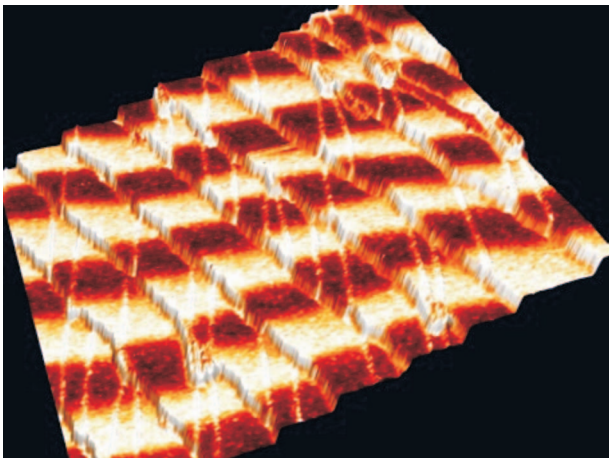

FIG. 28. (Color) Rendered perspective topographic STM image (200×200 nm^2) of a closed Fe double layer prepared on a stepped W(110) substrate, color coded with the spin-resolved spectroscopic dI/dU signal as measured with an out-of-plane-sensitive GdFe-coated tip. The Fe thin film exhibits a stripe domain phase along the $[1\bar{1}0]$ direction with a magnetic periodictiy of about 50 nm. From Kubetzka *et al.*, 2002.

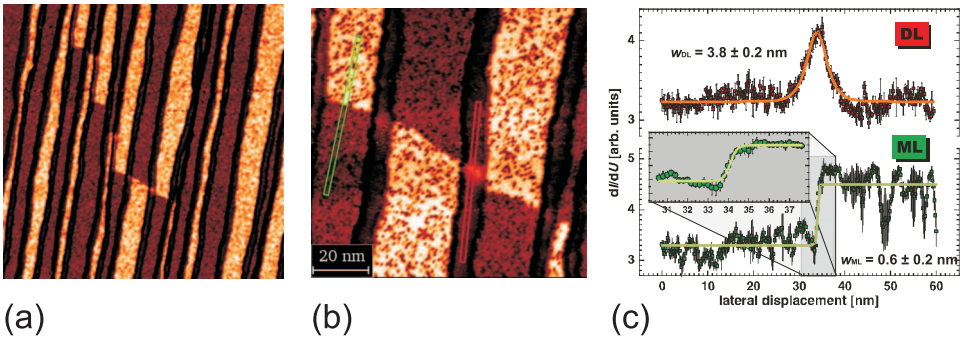

FIG. 29. (Color) Ultrasharp magnetic domain walls. (a) Spin-resolved spectroscopic dI/dU map (400×400 nm^2) of 1.25 ML Fe on a stepped W(110) substrate as measured with an in-plane-sensitive Fe-coated W tip. Monolayer stripes with in-plane magnetic anisotropy exhibit a domain contrast whereas the narrow double-layer stripes in between exhibit a domain wall contrast which is more clearly visible in the zoom-in SP-STS image of (b). A detailed analysis of line profiles across the domain walls of first- and second-layer Fe nanostripes, based on micromagnetic theory, leads to wall widths of $w_{DL}=3.8\pm0.2$ nm for the narrow Fe double-layer nanostripe and $w_{ML}=0.6\pm0.2$ nm for the Fe monolayer stripes (c). From Pratzer *et al.*, 2001.

Hamann theory, which is based on a perturbative treatment of tunneling in the regime of reasonably large values of the tunneling gap resistance, should be applicable. Within the Tersoff-Hamann theory, the following expression for the lateral resolution Δx of STM has been derived (Wiesendanger, 1994a):

$$\Delta x \approx [(2\ \text{Å})(R_t+s)]^{1/2}, \tag{37}$$

where R_t is the effective tip radius and s is the tip-sample distance. Assuming an effective tip radius of $R_t \sim 1$ nm and a tip-surface separation of $s\sim0.7$–1.0 nm, a lateral STM resolution of $\Delta x\sim0.6$ nm results, meaning that instrumental broadening effects cannot be neglected at this particular length scale. Therefore, the true width of the domain wall for the Fe monolayer on W(110) is most likely smaller than the value of 0.6 nm derived from the SP-STS data. If this is the case, one might question the applicability of micromagnetic theory which has been used to fit the domain-wall profile [Eq. (36)]. The spin structure of domain walls in the ultimate limit of very high magnetic anisotropy has been investigated theoretically by Hilzinger and Kronmüller (1972). It was found that micromagnetic theory describes the spin structure of the domain wall reasonably well as long as $(k/A)^{1/2}a<1$, i.e., as long as the width of the domain wall $w\geqslant3a$, where a is the lattice constant. However, if the magnetic anisotropy reaches a critical value, given by $(k/A)^{1/2}a>1.5$, spin rotation no longer takes place continuously, but occurs by an abrupt 180° rotation between two adjacent atomic lattice sites (Fig. 30). Since the values of k and A for the first monolayer of Fe on W(110) are close to the limit where a continuous spin rotation becomes unstable, the extremely sharp domain walls as observed by SP-STS might result from lines of antiferromagnetically coupled lattice sites.

A similar SP-STS study of the magnetic domain and domain-wall structure of monolayer and double-layer nanostripes was performed for Fe deposited onto a stepped Mo(110) substrate (Bode, Kubetzka, von Bergmann, *et al.*, 2005; Prokop *et al.*, 2005, 2006). In contrast to the Fe/W(110) system, the Fe monolayer stripes on Mo(110) were found to be perpendicularly magnetized. The Fe double-layer nanostripes on Mo(110) also exhibit a perpendicular magnetic anisotropy and are antiferromagnetically coupled due to magnetostatic interaction. Domain-wall widths of $w_{DL}=4.2\pm0.5$ nm for the Fe double-layer nanostripes and $w_{ML}=1.2$–2.9 nm for the Fe monolayer stripes were extracted from line profiles of SP-STS data. More recently, Au-coated Fe nanostripes on stepped Mo(110) substrates were investigated by SP-STS (Prokop *et al.*, 2007). However, the interpretation of the data was complicated by the fact that interdiffusion and alloying between Au and Fe led to nanostructures of unknown chemical composition and magnetic properties.

SP-STS studies have also been performed on Co nanostripes grown on stepped Pt(111) substrates (Meier *et al.*, 2006, 2007). Despite the strong electronic inhomogeneity of the Co monolayer stripes on Pt(111), resulting from the existence of double-row reconstruction lines, a magnetic domain structure with a perpendicular easy-axis magnetization direction could be observed with SP-STS using out-of-plane-sensitive Cr-coated tips [Fig. 31(a)]. The dominant feature in the spin-resolved tunneling spectra of Co/Pt(111) was assigned to a d-like surface resonance of minority-spin character, which is

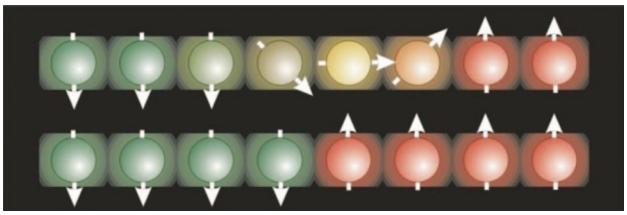

FIG. 30. (Color) Schematic of a narrow domain wall where the magnetization rotates quasicontinuously on a lateral scale of several lattice sites (top part) and the case of an extremely narrow domain wall for which the spin-density orientation rotates between two atoms, where the spin density is minimal, leading to antiferromagnetically coupled neighboring lattice sites (bottom part).

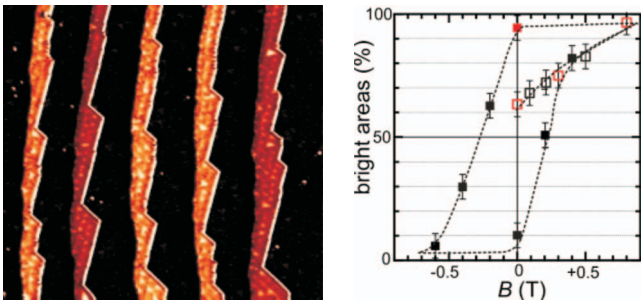

FIG. 31. (Color) Magnetic behavior of Co nanostripes. (a) Spin-resolved spectroscopic dI/dU map (130×130 nm^2) of Co monolayer nanostripes prepared on a stepped Pt(111) substrate, as measured with an out-of-plane sensitive Cr-coated W tip. (b) Magnetic hysteresis curve extracted from SP-STS data of Co monolayer stripes on Pt(111) showing a coercive field of 0.25 ± 0.05 T. From Meier *et al.*, 2006.

highly sensitive to the type of Co stacking (fcc or hcp). A domain-wall width of less than 4 nm was determined for the Co monolayer on Pt(111). Furthermore, the response of arrays of Co monolayer and double-layer stripes to an external magnetic field was studied. While the Co monolayer nanostructures exhibited a coercivity of about 0.25 T [Fig. 31(b)], a much higher coercive field of more than 2 T was found for Co double-layer nanostripes on Pt(111) substrates.

C. Magnetic states of nanoislands and nanoparticles

As a local probe, SP-STM or SP-STS allows the investigation of individual nanoislands and nanoparticles in various size regimes, from the mesoscopic scale of several hundred nanometers down to the single-digit nanometer scale. Different types of magnetic state can be found as a function of island size and island thickness. Thanks to the unprecedented spatial resolution of SP-STM and SP-STS, the various magnetic states of individual islands and nanoparticles can now be studied down to the atomic level.

1. Multidomain states

If the size of magnetic islands or particles well exceeds the magnetic length scale given by the domain-wall width, they exhibit a multidomain state similar to the corresponding thin-film system, thereby reducing the stray-field energy. Figure 32 shows multidomain Dy islands with sizes much larger than the typical domain-wall width (between 2 and 5 nm). The observed domain structure on the Dy islands resembles the one found for extended Dy thin films (Sec. IV.A.1). Multidomain states were also observed on Gd islands of similar size in early SP-STS studies (Bode, Getzlaff, and Wiesendanger, 1998).

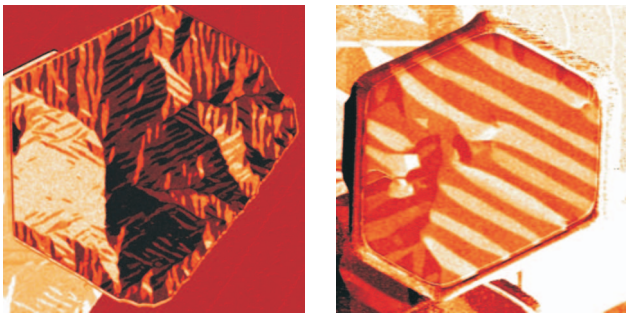

FIG. 32. (Color) SP-STS images showing the multidomain state of large nanoislands of Dy on a W(110) substrate. The island size is about (a) 800 nm and (b) 400 nm.

2. Magnetic vortex states

As the island size is reduced, another micromagnetic state becomes favorable. This state is characterized by a magnetic vortex exhibiting a curling in-plane magnetization, which gradually becomes out of plane as the central vortex core region is approached [Fig. 33(a)]. SP-STS allows the imaging of these magnetic vortex states with unprecedented spatial resolution (Wachowiak *et al.*, 2002; Bode, Wachowiak, *et al.*, 2004). Figure 33(b) shows SP-STS data of a vortex core state in an Fe nanoisland obtained with an in-plane-sensitive Cr-coated W tip. The continuously curling in-plane magnetization component leads to a cosinelike dependence of the spin-resolved dI/dU signal (Wachowiak *et al.*, 2002). The spin contrast in the spectroscopic data originates from a minority-spin d-like surface resonance in this case. By preparing tips with different Cr coating thickness, both in-plane and out-of-plane components of the surface magnetization distribution can be revealed [Figs. 34(a) and 34(b)]. An analysis of line profiles across magnetic vortex cores, as extracted from in-plane- and out-of-plane-sensitive SP-STS images, yields a consistent value for the width w_V

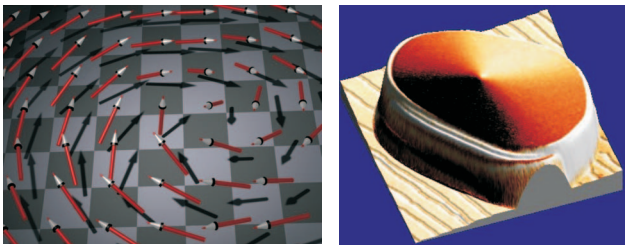

FIG. 33. (Color) Application of SP-STM to magnetic vortex states. (a) Schematic of a magnetic vortex. Far away from the vortex core the magnetization continuously curls around the vortex center with an orientation in the surface plane. Toward the center of the vortex core the magnetization turns out of the surface plane until it is perpendicularly oriented. (b) SP-STS image revealing a magnetic vortex state in an Fe island with a size of about 200 nm and a thickness of about 8 nm. A Cr-coated W-tip that is sensitive to the in-plane magnetization component was used.

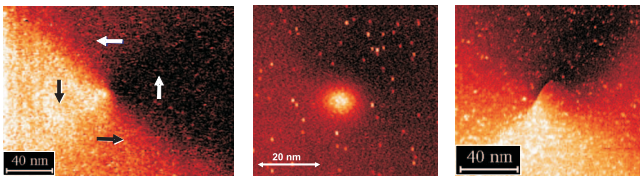

FIG. 34. (Color) Magnetic vortex core contrast depending on the SP-STM tips being used. (a) High-resolution SP-STS image of the in-plane magnetization component of a magnetic vortex core state in an Fe island measured with an in-plane-sensitive Cr-coated W tip. (b) High-resolution SP-STS image of the out-of-plane magnetization component of a magnetic vortex core state measured with an out-of-plane-sensitive Cr-coated W tip. (c) Distorted SP-STS image of a magnetic vortex core obtained with an Fe-coated W tip.

=9 nm of the central vortex core of Fe nanoislands. That size of a magnetic vortex core was theoretically (Feldtkeller and Thomas, 1965) determined by the minimum of the total energy, which is dominated by the exchange and the magnetostatic (or demagnetization) energy; the magnetocrystalline and the surface anisotropy energy contributions are negligible as long as magnetically soft materials are considered. For the thin-film limit, the following expression for the vortex core width w_V was derived:

$$w_V = 2(A/K_d)^{1/2} \approx 6.4 \text{ nm}, \tag{38}$$

where A is the exchange stiffness and $K_d = \mu_0 M_{\text{sat}}^2/2$ is the magnetostatic energy density with M_{sat} the saturation magnetization. For the material parameters of Fe a theoretical value of $w_V \sim 6.4$ nm is obtained for the vortex core width, in reasonable agreement with the experimental value derived from the SP-STS data. It is surprising that it took almost 40 years for a quantitative determination of the size of magnetic vortex cores to be achieved. It should be emphasized that the use of antiferromagnetic probe tips in SP-STS has proven indispensable for a reliable and quantitative analysis of the central regions of magnetic vortex cores (Wachowiak *et al.*, 2002). If ferromagnetically coated tips are used, the vortex core can easily be perturbed by magnetostatic interactions between tip and sample as shown in Fig. 34(c). This can happen even in cases where the Fe coating thickness is reduced to only 3 ML.

The response of a magnetic vortex core to an external magnetic field applied perpendicular to the sample surface plane is shown in Fig. 35. Depending on the direction of the external field relative to the out-of-plane magnetization direction in the vortex core, parallel or antiparallel, the size of the vortex core is either increased or decreased, respectively. Comparison of the experimental data to the field dependence with micromagnetic calculations confirms that only two material parameters, the exchange stiffness and saturation magnetization, are relevant for the size and shape of magnetic vortex cores in Fe nanoislands.

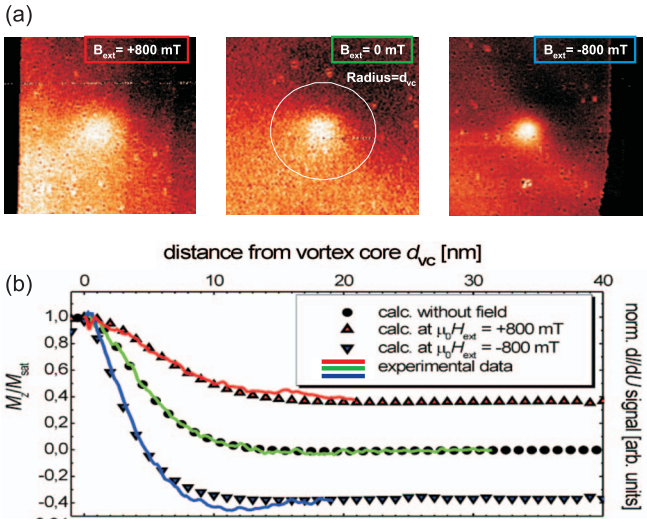

FIG. 35. (Color) Magnetic vortex core contrast as function of external field direction. (a) Response of a magnetic vortex core to an external magnetic field: while the size of the vortex core is increased if the external field is applied parallel to the out-of-plane magnetization direction in the core region, the opposite behavior is observed for the antiparallel case. (b) The field dependence of line profiles across the vortex core, extracted from the experimental SP-STS data obtained with a Cr-coated tip, show good agreement with calculated line profiles based on micromagnetic theory. From Wachowiak *et al.*, 2002.

Micromagnetic calculations (Hertel, 2002) also showed that the lowest-energy state of magnetic nanoislands depends not only on their lateral size but also on their thickness (Bode, Wachowiak, *et al.*, 2004). For instance, by increasing the Fe island thickness from 7.5 to 8.5 nm, while keeping the lateral size constant, a transition from a single-vortex to a double-vortex ("diamond") state has been observed by SP-STS (Fig. 36). On the other hand, if the thickness of a nanoisland with a given lateral size is reduced, a transition from a single-vortex state to a single-domain state occurs (Yamasaki *et al.*, 2003; Bode *et al.*, 2004).

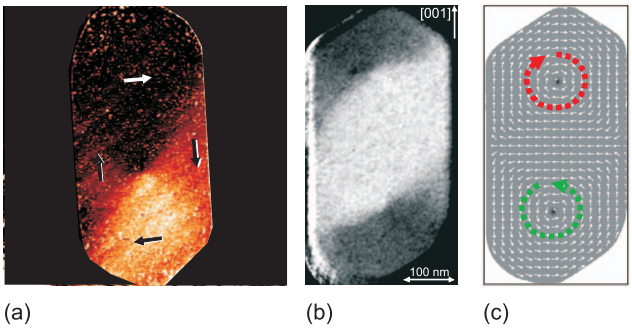

FIG. 36. (Color) Magnetic vortex core state as function of nanoisland thickness. (a) SP-STS image (400×400 nm^2) showing a single-vortex state of an Fe island 7.5 nm thick. (b) Diamond (double-vortex) state observed by SP-STS on an Fe island of similar lateral size but slightly thicker (8.5 nm) than the one in (a). (c) Magnetization distribution for the double-vortex state observed in (b). From Bode, Wachowiak, *et al.*, 2004.

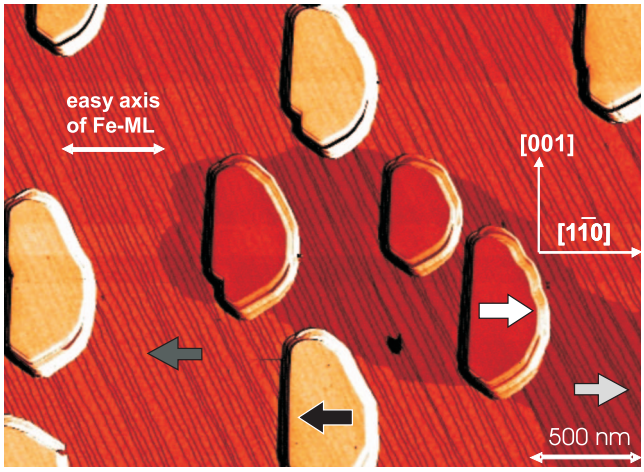

FIG. 37. (Color) SP-STS data obtained with an Fe-coated W tip showing simultaneously in-plane magnetized, single-domain Fe nanoislands and the magnetic domain structure of an Fe monolayer (wetting layer) on a W(110) substrate. The magnetization directions of the Fe nanoislands and the magnetic domain structure of the Fe monolayer are strongly correlated. From Wiesendanger *et al.*, 2004.

3. Single-domain states

For islands with a sufficiently small lateral size and thickness, the single-domain state becomes energetically favorable. Figure 37 shows Fe islands of similar size to the ones presented in Figs. 36(a) and 36(b), but with a reduced thickness of only 3.5 nm. They exhibit a spatially uniform spin-resolved dI/dU signal characteristic for a single domain state. Since an in-plane-sensitive Fe-coated probe tip has been used for recording the SP-STS data, one can conclude that these Fe islands have a twofold magnetic in-plane anisotropy leading to two different spin contrast levels for different islands. Between the 3D Fe islands, which were prepared in the Stranski-Krastanov growth mode on a W(110) substrate, an Fe wetting layer of single atomic height exists that exhibits a magnetic domain structure. The transitions between the magnetic domains of the Fe monolayer, i.e., the domain walls, appear atomically sharp, as in the case of Fe monolayer stripes on W(110) (Sec. IV.B). Interestingly, the magnetization state of the single-domain nanoislands is strongly correlated with the magnetic domain structure of the Fe monolayer.

As the thickness of the Fe nanoislands on the W(110) substrate is reduced to 2 ML, a thickness-dependent reorientation transition of magnetic anisotropy leads to an out-of-plane magnetization state of such nanoislands which can be observed with an out-of-plane-sensitive probe tip [Fig. 38(a)]. The Fe monolayer that is exposed between the double-layer islands exhibits an in-plane magnetic anisotropy. This type of thickness-dependent behavior was also found for Fe double-layer and monolayer nanostripes (Sec. IV.B). However, in addition to the thickness-dependent magnetic anisotropy of Fe nanostructures on W(110), one can observe a size-dependent reorientation transition of magnetic anisotropy. Figures 38(b) and 38(c) show that the out-of-plane spin contrast disappears for the smallest islands with a lateral size below 2.5 nm. The size-dependent behavior can be understood based on a model of spatially switching magnetic anisotropies (Elmers, 1998; Kubetzka *et al.*, 2001). Consideration of nanoscale Fe islands shows that, as the double-layer islands become smaller and smaller, the energy gained by turning the magnetization into the easy direction of the double layer decreases. If the double-layer island size is reduced below a critical value, the energy gain for turning the magnetization out of plane into the easy direction of the Fe double layer becomes less than the energy that has to be used for a 90° domain wall between the Fe double-layer nanoisland and the in-plane-magnetized Fe monolayer. As a result, the magnetization direction of the smallest Fe double-layer nanoislands follows that for the Fe monolayer. This example illustrates that the application of SP-STM or SP-STS leads to considerably improved insight into the magnetic behavior of spatially inhomogeneous systems.

Nanoscale Fe islands of double-layer height have also been studied on W(001) substrates by SP-STS (Kubetzka *et al.*, 2005; von Bergmann *et al.*, 2005). In this case a fourfold in-plane magnetic anisotropy has been revealed

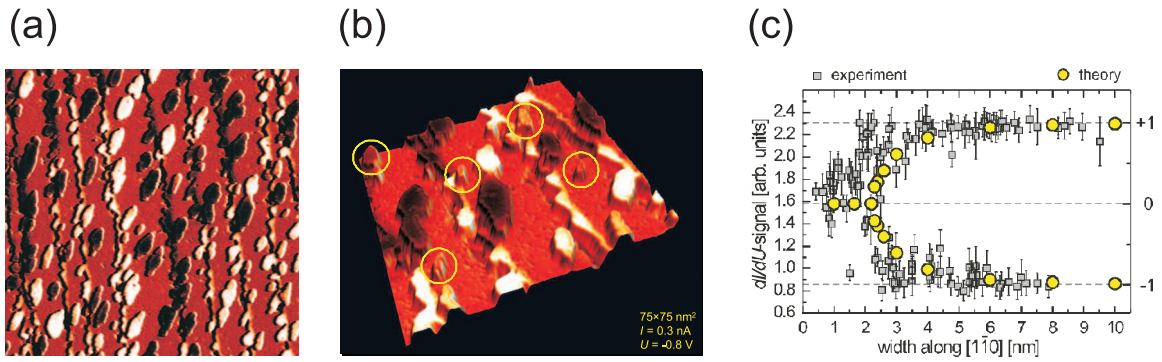

FIG. 38. (Color) Magnetism of single-domain nanoislands as function of their lateral size. (a) SP-STS image(400×400 nm^2) of Fe double-layer nanoislands with a Fe monolayer in between. The data have been recorded with an out-of-plane-sensitive Gd-coated probe tip. (b) Zoom-in SP-STS image (70×70 nm^2) showing vanishing out-of-plane spin contrast on the smallest Fe double-layer nanoislands. (c) Magnitude of the spin-resolved dI/dU signal as a function of the islands' lateral size.

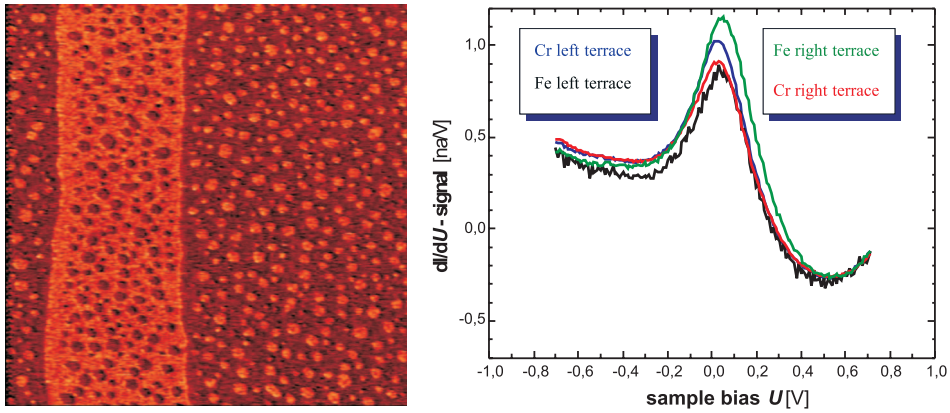

FIG. 39. (Color) Exchange-coupled nanoislands. (a) Spin-resolved dI/dU map (400×400 nm^2) of nanoscale Fe islands of single-atomic height on a stepped Cr(001) substrate. The data were recorded at room temperature with an in-plane-sensitive Fe-coated tip. Due to an antiferromagnetic exchange coupling between the nanoscale Fe islands and the Cr(001) substrate, the Fe islands are magnetized in opposite directions relative to the underlying Cr(001) terraces and therefore exhibit opposite in-plane spin contrast. (b) Local spin-resolved differential tunneling conductance spectra as measured above differently magnetized Cr(001) terraces and corresponding Fe nanoislands located on top of these two types of Cr(001) terraces. The reversal of intensity levels of the differential tunneling conductance at the bias voltage corresonding to the energetic position of the d_{z^2}-like surface state of Fe(001) and Cr(001) indicates the antiferromagnetic coupling between the Fe islands and the Cr(001) substrate. From Ravlic, Bode, and Wiesendanger, 2003.

by performing spin-resolved spectroscopic measurements with an in-plane-sensitive Fe-coated W tip.

Monolayer-high Fe nanoislands have been studied on W(110) and Mo(110) substrates by SP-STS. Interestingly, while the monolayer Fe islands on W(110) exhibit in-plane magnetic anisotropy (Krause *et al.*, 2007), the Fe nanoislands on Mo(110) were found to be magnetized out of plane (Bode, Pietzsch, *et al.*, 2004; Bode, Kubetzka, von Bergmann, *et al.*, 2005; Prokop *et al.*, 2006), similarly to the behavior of the corresponding nanostripe systems (Sec. IV.B). In contrast to double-layer-high Fe nanoislands surrounded by an Fe monolayer (wetting layer), as discussed above, Fe monolayer islands on nonmagnetic substrates are not exchange coupled but only weakly coupled by magnetostatic interaction. Therefore, monolayer-high Fe islands of small lateral size (<10 nm) usually exhibit a thermally induced magnetization switching even at low temperatures (see Sec. IV.F.1). On the other hand, by choosing an antiferromagnetic substrate, such as Cr(001), nanoscale Fe islands were found to be magnetically stable even at room temperature (Ravlic, Bode, and Wiesendanger, 2003). This experimental observation can be explained by an antiferromagnetic exchange coupling between the nanoscale Fe islands and the Cr(001) substrate as directly revealed by SP-STS (Fig. 39).

In addition to nanoscale Fe islands, SP-STS studies have also focused on nanoscale Co islands, particularly on Cu(111) and Pt(111) substrates (Pietzsch *et al.*, 2004a, 2006; Rusponi *et al.*, 2005; Meier *et al.*, 2006, 2007). In both cases, the competition between fcc and hcp stacking of the Co islands grown on fcc(111) substrates leads to a spatially inhomogeneous (spin-averaged) electronic structure, which needs to be distinguished from spin-dependent contrast in SP-STS data, related to the different magnetic states of such islands. Figure 40(a) shows spin-averaged STS data of nanoscale Co islands on a Cu(111) substrate as measured with a nonmagnetic W tip. Surprisingly, a strong spectroscopic contrast is observed between different Co islands of the same height [two layers above the Cu(111) substrate] and similar lateral size. The two different contrast levels cannot be related to different magnetization states in this case but rather to a different type of crystallographic stacking, as is obvious from the strong correlation of the different spectroscopic contrast levels with the orientation of the triangular-shaped Co islands relative to the Cu(111) substrate. By analyzing the local differential tunneling conductance spectra measured with a W tip on differently stacked Co islands (fcc and hcp), a clear difference is observed between the two spectra for the negative-bias-voltage regime, which can be assigned to a stacking-sensitive d_{z^2}-like surface state peak showing up at -0.35 V for fcc and at -0.28 V for hcp stacked Co islands [Fig. 40(b)]. This example illustrates that differences in spectroscopic contrast between islands of the same elemental composition as well as of the same size and height cannot simply be interpreted in terms of different magnetization states.

If a magnetically coated W tip that is sensitive to the out-of-plane magnetization component is used, an additional spin-dependent contrast is observed for the double-layer Co nanoislands on Cu(111) which exhibit a strong out-of-plane magnetic anisotropy. In this case, four different types of spin-resolved local tunneling conductance spectra are obtained [Fig. 41(a)], resulting from the two different types of stacking plus the two different

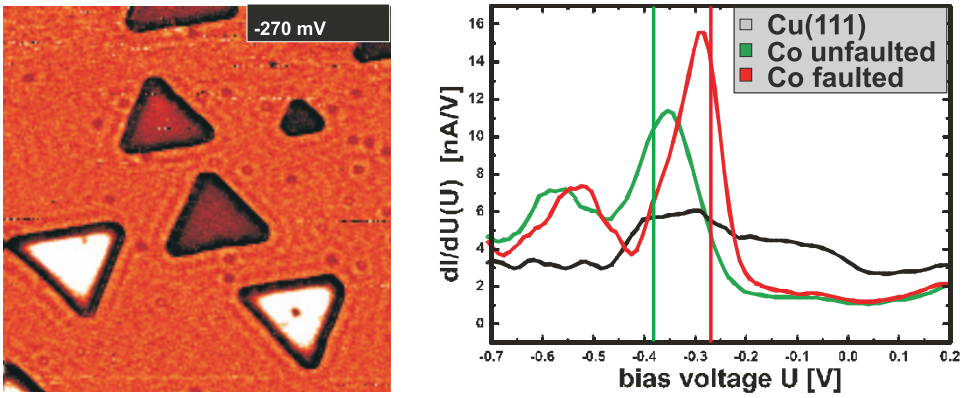

FIG. 40. (Color) Stacking-dependent spectroscopic contrast on Co nanoislands. (a) Spin-averaged dI/dU map (60×60 nm^2) of nanoscale Co islands [two layers high relative to the Cu(111) substrate] as measured with a nonmagnetic W tip. The strong spectroscopic contrast between different islands originates from a different stacking of the Co islands and is a pure electronic structure effect. It is not related to a different magnetization state of the Co islands. (b) Local (spin-averaged) differential tunneling conductance spectra obtained with a nonmagnetic W tip above differently stacked Co islands. While a d_{z^2}-like surface state related peak is found at a sample bias voltage of −0.35 V for fcc-stacked Co islands, this peak is shifted to −0.28 V for hcp-stacked Co islands. This difference gives rise to a stacking-dependent contrast in spatially resolved spectroscopic images. The third spectrum shown was measured above the Cu(111) substrate. It shows a conductance rise at −0.46 V which is related to the onset of the free-electron-like *sp*-type surface state of the Cu(111) substrate. From Pietzsch *et al.*, 2004a.

types of relative orientation of tip and island magnetization (parallel or antiparallel). In order to discriminate between the structure-related electronic contrast and the magnetization-dependent spin contrast, the so-called structural asymmetry defined by

$$A_{\text{struct}}(eU) = \frac{dI/dU_{\text{fcc}}(U) - dI/dU_{\text{hcp}}(U)}{dI/dU_{\text{fcc}}(U) + dI/dU_{\text{hcp}}(U)} \tag{39}$$

and the spin asymmetry defined by

$$A_{\text{spin}}(eU) = \frac{dI/dU_{\uparrow\uparrow}(U) - dI/dU_{\uparrow\downarrow}(U)}{dI/dU_{\uparrow\uparrow}(U) + dI/dU_{\uparrow\downarrow}(U)} \tag{40}$$

have to be calculated as functions of bias voltage, i.e., as functions of energy [Fig. 41(b)]. A pure and clear magnetic contrast is obtained if the applied bias voltage is chosen such that the structural asymmetry vanishes while the spin asymmetry reaches a high absolute value (see Sec. III.B.2). This is illustrated in Fig. 41(c) showing a spin-resolved STS image of the Co nanoislands on Cu(111) obtained with an appropriately chosen bias voltage. In this case, the spectroscopic contrast is related to the different magnetization states of the Co islands and is no longer correlated with the orientation of the Co islands relative to the Cu(111) substrate.

A definite proof of the magnetic origin of the observed spectroscopic contrast in SP-STS is given by studying the response of the system to external magnetic fields of different magnitude and orientation. Such field-dependent SP-STS data for Co nanoislands on Cu(111), obtained with an out-of-plane-sensitive Cr-coated W tip and an appropriately chosen sample bias voltage, are presented in Fig. 42. At zero applied field an equal number of bright (upward-magnetized) and dark (downward-magnetized) Co islands exists. As the external field is increased in the $+z$ direction perpendicular to the sample surface plane, more and more Co islands switch their magnetization state to become bright, i.e., their magnetization direction is becoming aligned with the external field direction. When the direction of the external field is reversed to the $-z$ direction, the spin-resolved spectroscopic contrast of the Co islands is reversed. The system becomes magnetically saturated in an external field of about 1.8 T. A large remanence-to-saturation ratio $M_r/M_s \sim 1$ and a high coercive field of $1 < \mu_0 H_c < 1.5$ T is observed for this particular system (Pietzsch *et al.*, 2004a). It should be emphasized that the use of an antiferromagnetically coated probe tip was essential for this experiment in order to exclude field-induced changes of the tip's magnetic state. If a ferromagnetically coated probe tip is chosen, the observed contrast on the islands is always bright in a high external field, independent of its direction, because both tip and sample magnetizations are aligned parallel (either in the $+z$ or in the $-z$ direction).

4. Spin-dependent quantum confinement states in nanoislands

For sufficiently small islands with a lateral size comparable to the electron wavelength, the quantum mechanical confinement of the electrons can lead to an energy-dependent oscillatory LDOS distribution at the islands' surfaces. This is illustrated by the spin-averaged STS data for nanoscale Co islands on the Cu(111) surface presented in Fig. 43. While similar STS observations have been made for many different types of nanoscale island system (see, e.g., Li *et al.*, 1998; Diekhöner *et al.*, 2003), SP-STS additionally allows questions related to the magnetic state of such islands to be addressed. In

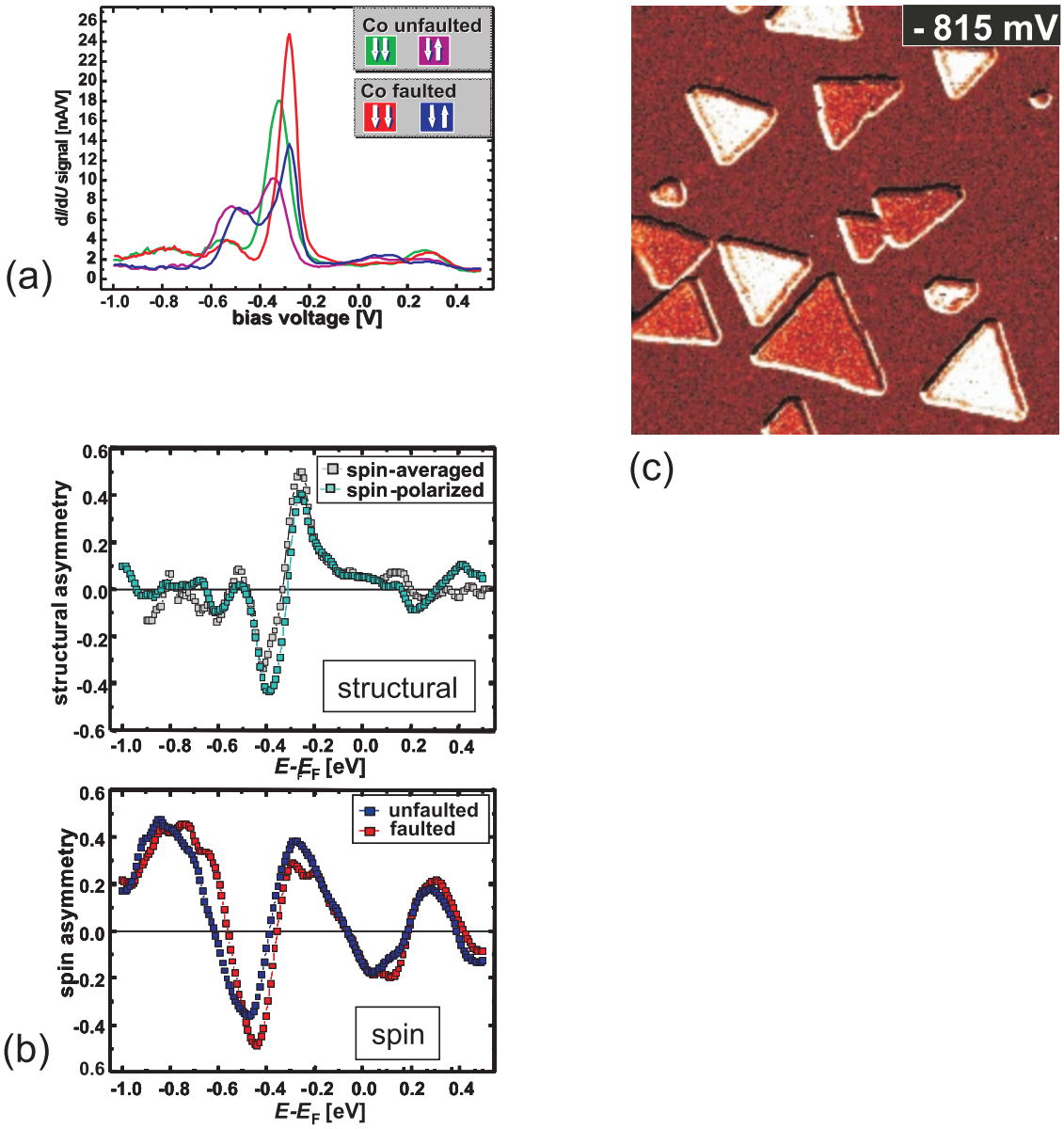

FIG. 41. (Color) Disentangling stacking- and magnetic-state-dependent contrast of Co nanoislands. (a) Spin-resolved differential tunneling conductance spectra measured with an out-of-plane-sensitive Cr-coated W tip on differently stacked and differently magnetized double-layer Co nanoislands on Cu(111). (b) Energy-dependent "structural asymmetry" and "spin asymmetry" curves derived from the spin-resolved tunneling spectra presented in (a). By choosing sample bias voltages for which the spin asymmetry becomes large while the structural asymmetry is negligible, a clear and pure magnetic contrast can be achieved in spatially resolved SP-STS measurements (c). Image size: 60×60 nm^2.

particular, the spin dependence of the electronic confinement states and the spin dependence of the electronic scattering at nanoscale interfaces, such as those between magnetic nanoislands and nonmagnetic substrates, can be investigated by SP-STS (Pietzsch *et al.*, 2006). The spin dependence of 2D electronic confinement states in nanoscale Co islands is revealed by the experimental observation of a spin-dependent LDOS oscillation amplitude of the confinement states for differently magnetized Co nanoislands (Fig. 44). Based on knowledge of the spin character of the tip's electronic states, the spin character of the observed oscillatory confinement states can be derived. In the case of nanoscale Co islands, the main contribution to the observed spin-dependent LDOS oscillations was found to originate from a dispersive majority-spin state (Pietzsch *et al.*, 2006).

In addition to the lateral 2D electronic confinement states in nanoscale islands, 1D electronic confinement has been revealed at the edges of such islands. By performing spin-resolved spectroscopic measurements, the spin character of the 1D electronic confinement states is determined as a function of energy (Pietzsch *et al.*, 2006). Interestingly, the spin character of the 1D confinement states differed in magnitude as well as in sign from the spin character of the 2D confinement states for a wide

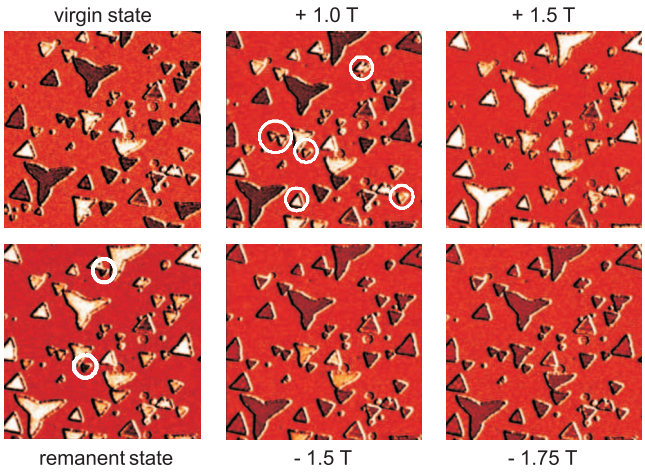

FIG. 42. (Color) Set of SP-STS data (150×150 nm^2) showing the response of nanoscale Co islands on Cu(111) to an external magnetic field applied perpendicular to the sample surface plane. The SP-STS images were obtained with an out-of-plane-sensitive Cr-coated W tip which is not affected by the external field. From Pietzsch *et al.*, 2004a.

range of energies. Since the lateral extension of the 1D confinement states was found to be less than 1 nm, it directly follows that the spin character of electronic states may change on a very small length scale which has not been accessible so far by other spin-resolved electron spectroscopy techniques.

D. Atomic-resolution spin mapping by SP-STM

While high-resolution imaging of magnetic domains and domain walls as well as spatially resolved mapping of spin-resolved electronic states are important fields of application for SP-STM and SP-STS, the development of the SP-STM technique was primarily motivated by a combination of the atomic-resolution capability of STM with spin sensitivity. This ultimate goal of magnetic imaging techniques has already been achieved by applying SP-STM to several different classes of magnetic materials, including antiferromagnetic transition-metal films, antiferromagnetic nitrides, and ferrimagnetic transition-metal oxides.

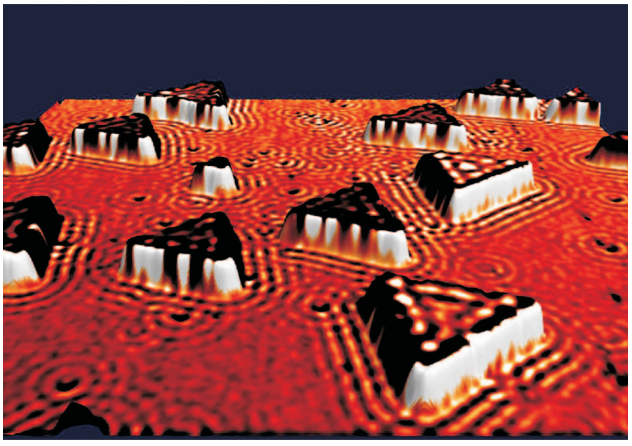

FIG. 43. (Color) Spin-averaged STS image (60×60 nm^2) showing 2D electronic confinement states in double-layer Co nanoislands on Cu(111) as well as scattering states of the Cu(111) surface state electrons at single Co adatoms and Co/Cu interfaces.

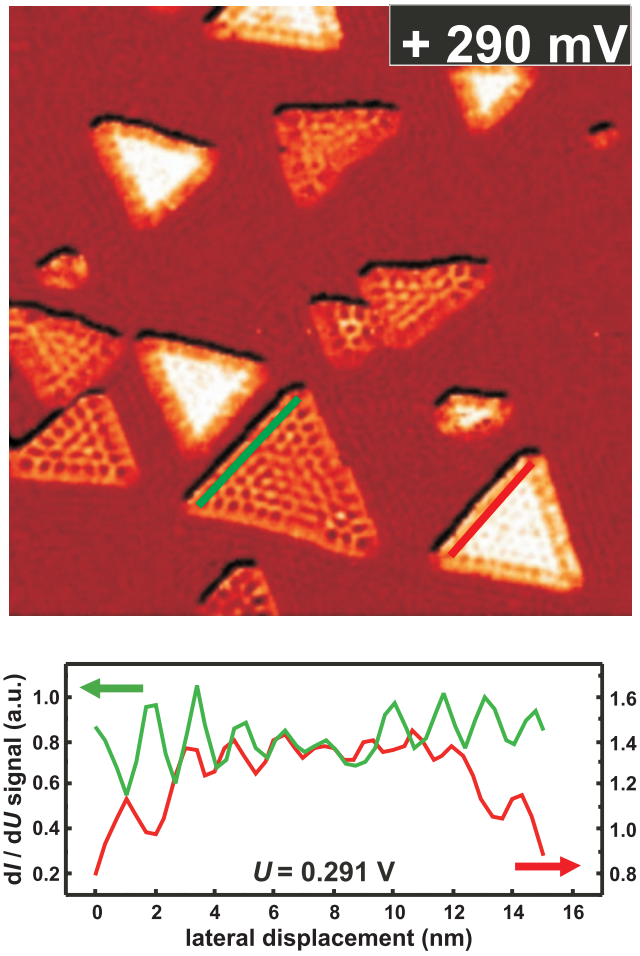

FIG. 44. (Color) SP-STS data (60×60 nm^2) revealing the spin dependence of the 2D electronic confinement states in nanoscale Co islands which manifests itself by a spin-dependent oscillation amplitude of the confinement states for differently magnetized Co nanoislands. From Pietzsch *et al.*, 2006.

1. Antiferromagnetic transition-metal films

It is difficult to investigate antiferromagnetic surfaces and thin films with experimental techniques which provide spatially averaged information at a length scale that is larger than the magnetic unit cell because the magnetic contributions of the two spin sublattices cancel and the net magnetization vanishes in this case. A particular challenge has been the observation of an antiferromagnetically ordered, densely packed atomic layer in which nearest-neighbor sites exhibit opposite orientations of their magnetic moments. SP-STM operated in the constant-current or the spectroscopic mode has been successfully applied to reveal surface spin structures even at this ultimate atomic length scale (Heinze *et al.*, 2000; Kubetzka *et al.*, 2005). A first example is given by the antiferromagnetic ground state of a single atomic

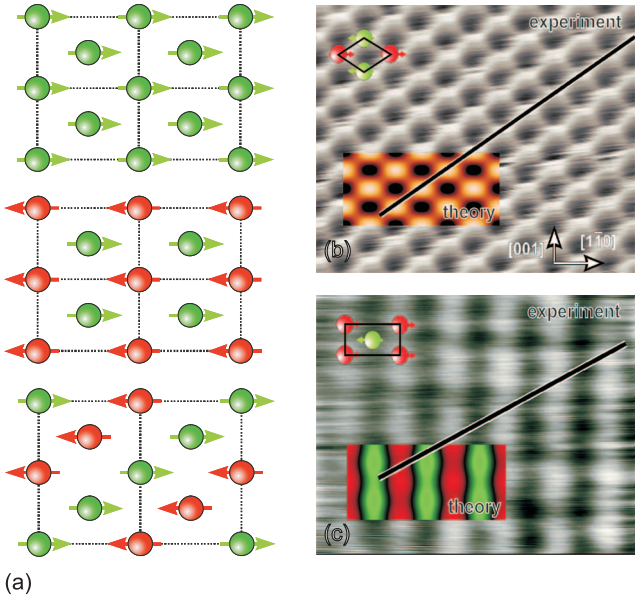

FIG. 45. (Color) Atomic-resolution spin mapping on an antiferromagnetic Mn monolayer. (a) Schematic of an antiferromagnetically ordered atomic layer with a bcc (110) lattice symmetry. The rectangular magnetic unit cell is twice larger than the diamond-shaped structural unit cell. (b) Atomic-resolution constant-current STM image (2.7×2.2 nm^2) of an atomic layer of Mn, pseudomorphically grown on a W(110) substrate. Since a nonmagnetic W tip was used in this case, the opposite orientation of magnetic moments of adjacent Mn atoms cannot be revealed. All Mn atoms therefore appear identical. (c) In contrast, the magnetic superperiodicity corresponding to the theoretically predicted $c(2\times2)$ antiferromagnetic state of the atomic layer of Mn on W(110) can be revealed by an in-plane sensitive Fe-coated W tip. The insets in (b) and (c) show a comparison with simulated STM and SP-STM images based on density functional theory, respectively. From Heinze *et al.*, 2000.

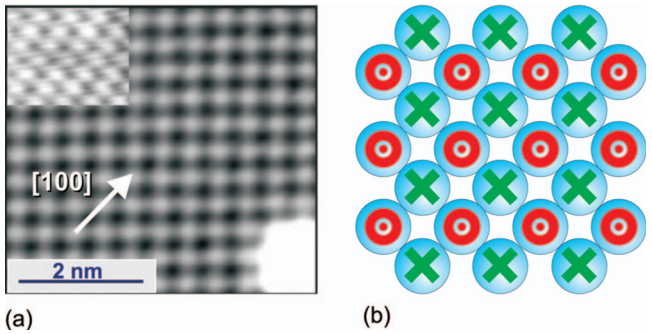

FIG. 46. (Color) Atomic-resolution spin mapping on an antiferromagnetic Fe monolayer. (a) SP-STM image showing the magnetic (2×2) superstructure of (b) an antiferromagnetic monolayer of Fe on a W(001) substrate. Since an out-of-plane magnetized Fe-coated W tip has been used, one concludes that the Fe monolayer on W(001) exhibits an out-of-plane magnetic anisotropy, which was subsequently confirmed by DFT calculations. The inset in (a) shows an atomically resolved (1×1) lattice as revealed either by a nonmagnetic or by an in-plane-sensitive probe tip. From Kubetzka *et al.*, 2005.

layer of Mn pseudomorphically grown on a W(110) substrate [Fig. 45(a)]. Conventional STM imaging in the constant-current mode of operation performed with a nonmagnetic W tip allows the visualization of the atomic structure of the Mn atomic layer without being sensitive to the magnetic superstructure [Fig. 45(b)]. However, if a magnetically coated tip is used, a completely different image is obtained. Instead of the pattern reproducing the atomic lattice periodicity, a stripelike pattern appears with a periodicity perpendicular to the stripes that is twice the structural periodicity [Fig. 45(c)]. The experimental observation can be interpreted as follows: If the tip apex atom and a Mn atom have their magnetic moments aligned parallel, the tunneling current will increase. As a consequence, the tip will be retracted from the surface in the constant-current mode of operation, leading to a bright contrast in the SP-STM image of Fig. 45(c). On the other hand, if the magnetic moments of the tip apex atom and the surface Mn atom are aligned antiparallel, the tunneling current will be lowered. Consequently, the tip will approach toward the surface under constant-current conditions, and a dark contrast in the SP-STM image results. By performing SP-STM experiments with in-plane-sensitive Fe-coated W tips as well as with out-of-plane-sensitive Gd-coated W tips, the theoretically predicted in-plane magnetic anisotropy of the $c(2\times2)$ antiferromagnetic layer of Mn on W(110) has been confirmed experimentally (Heinze *et al.*, 2000; Bode, Heinze, Kubetzka, Pietzsch, Hennefarth, *et al.*, 2002). It should be emphasized that SP-STM was the first experimental method capable of showing antiferromagnetic order in quasi-two-dimensional atomic layers on nonmagnetic substrates.

While the twofold symmetry of a (110) lattice leads to a stripelike magnetic superstructure like the one observed in Fig. 45(c), a fourfold-symmetric (001) lattice is expected to offer the ultimate test case for atomic-resolution SP-STM studies. An interesting example is provided by an Fe monolayer pseudomorphically grown on a W(001) substrate. Calculations based on density-functional theory (DFT) predicted an antiferromagnetic ground state for a single atomic layer of Fe on a (001)-oriented tungsten substrate (Wu and Freeman, 1992), in contrast to the ferromagnetic ground state of the Fe monolayer on a W(110) substrate (see Sec. IV.B). Indeed, using an out-of-plane-sensitive probe tip, the predicted Néel-type order, leading to a (2×2) antiferromagnetic superlattice, can directly be revealed in real space by SP-STM and SP-STS (Kubetzka *et al.*, 2005; von Bergmann *et al.*, 2005), while a nonmagnetic or in-plane-sensitive tip images only the (1×1) atomic lattice (Fig. 46). In order to prove the magnetic origin of the observed superstructure, field-dependent SP-STM experiments with ferromagnetic Fe-coated W tips were performed (Fig. 47). An external magnetic field on the order of 2 T applied perpendicular to the sample surface plane, i.e., along the tip axis, is sufficiently strong to reorientate the magnetization direction of an Fe-coated tip from in plane to out of plane, while leaving the antifer-

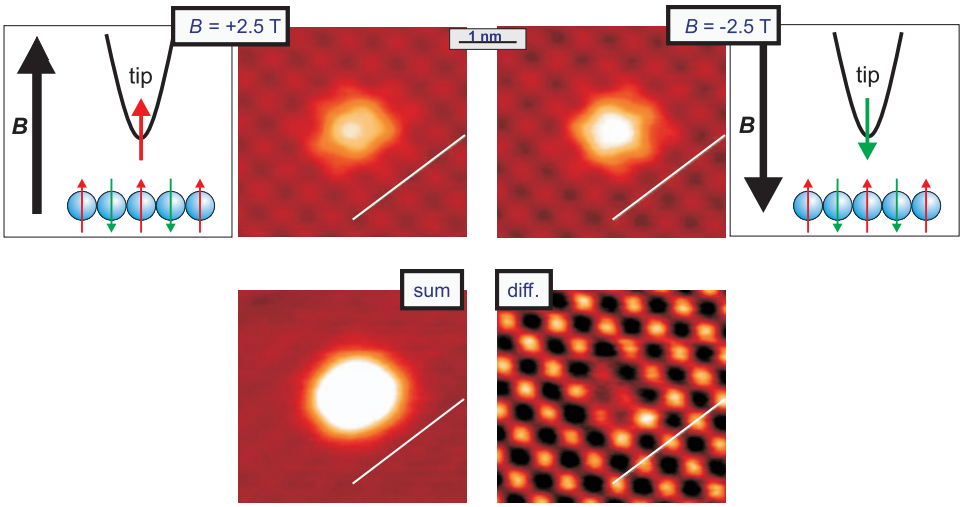

FIG. 47. (Color) The upper part shows two SP-STM images of exactly the same surface location on a 1 ML Fe/W(001) sample which were obtained with the same Fe-coated W tip magnetized by an external field in two opposite out-of-plane directions. An atomic adsorbate was used for making an accurate registry between the two SP-STM images allowing the calculation of the sum (topographic contrast) and difference (magnetic contrast) images (lower part).

romagnetic ground state of the single atomic layer of Fe on the W(001) substrate unaffected because the (antiferromagnetic) exchange coupling within the Fe monolayer is much larger than the Zeeman energy contribution related to the applied field. Consequently, it is possible, using the same tip, to switch reproducibly between a nonmagnetic and a magnetic imaging mode by appropriately aligning the tip's magnetization direction. Moreover, by changing the direction of the externally applied magnetic field and therefore the direction of the out-of-plane tip magnetization, a pair of spin-resolved images can be obtained showing the two different spin sublattices of the Néel-ordered state of the Fe monolayer on W(001) (Fig. 47). A scan window which includes an atomic adsorbate was chosen in this case in order to make an accurate registry between the two spin-resolved images, thereby allowing the calculation of the corresponding sum and difference images. While the sum image provides information about the surface topography, which is dominated by the adsorbate, the difference image enhances the magnetic contrast. Interestingly, the magnetic superstructure is visible even at the position of the adsorbate, indicating that the antiferromagnetic state of the Fe monolayer remains largely unaffected by the presence of the adsorbate.

Larger-scale SP-STM data of the atomically resolved antiferromagnetic Fe monolayer on W(001) reveal a perfect Néel-ordered state even in the presence of atomic-scale defects (e.g., vacancies and impurities) and ferromagnetic second-layer Fe islands [Fig. 48(a)]. Based on the accurate atomic-level registry between several SP-STM images obtained at different laterally shifted positions of the sample, an extended view of the surface spin structure in the presence of surface imperfections can be obtained [Fig. 48(b)]. This example demonstrates the high degree of reproducibility that can now be achieved in atomic-resolution SP-STM investigations performed at cryogenic temperatures.

Domain walls were found to be very rare for the Fe monolayer on W(001). They typically occur if two extended defects are close in space. In that case, it was possible to reveal the spin structure of a domain wall in an antiferromagnetic system with atomic resolution (Bode, Vedmedenko, *et al.*, 2006). The experimental SP-STM data were found to be in excellent agreement with theoretical results based on Monte Carlo simulations (Fig. 49). This example illustrates the potential of SP-STM for revealing even complex noncollinear spin structures at the atomic level.

Recently another example of a noncollinear spin structure was found in near-atomic-resolution SP-STM studies of 10–15 ML films of Mn on Fe(001) substrates (Gao *et al.*, 2007). Using the modulated tip magnetization mode of operation together with ferromagnetic ring electrode probes having a well-defined in-plane magnetization direction, they found that the reconstructed Mn surface formed a complex noncollinear antiferromagnetic structure with both the size and direction of the in-plane magnetization varying within the 0.9×1.8 nm^2 large unit cell.

2. Antiferromagnetic nitrides and ferrimagnetic oxides

Near-atomic-resolution SP-STM in the constant-current mode of operation has also been applied to more complex material systems, such as antiferromagnetic transition-metal nitrides and ferrimagnetic transition-metal oxides. For instance, using in-plane-sensitive Mn-coated W tips, the antiferromagnetically coupled rows of Mn1 sites on the $Mn_3N_2(010)$ surface were directly revealed even at room temperature (Yang *et al.*, 2002; Smith *et al.*, 2004, 2005; Yang *et al.*, 2006). The SP-STM images on this particular surface were found to contain two components, the nonpolarized and the spin-polarized contributions, exhibiting spatial periods of 0.6 and 1.2 nm, respectively (Fig. 50).

Since the early stage of SP-STM development, strong emphasis was put on the investigation of various magnetite (Fe_3O_4) surfaces (Wiesendanger, Shvets, *et al.*, 1992a, 1992b, 1992c; Koltun *et al.*, 2001; Shvets *et al.*, 2004; Berdunov, Murphy, Mariotto, and Shvets, 2004; Berdunov, Murphy, Mariotto, Shvets, and Mykovskiy, 2004; Jordan *et al.*, 2005). Bulk magnetite is expected to exhibit the characteristics of a half-metallic ferromagnet

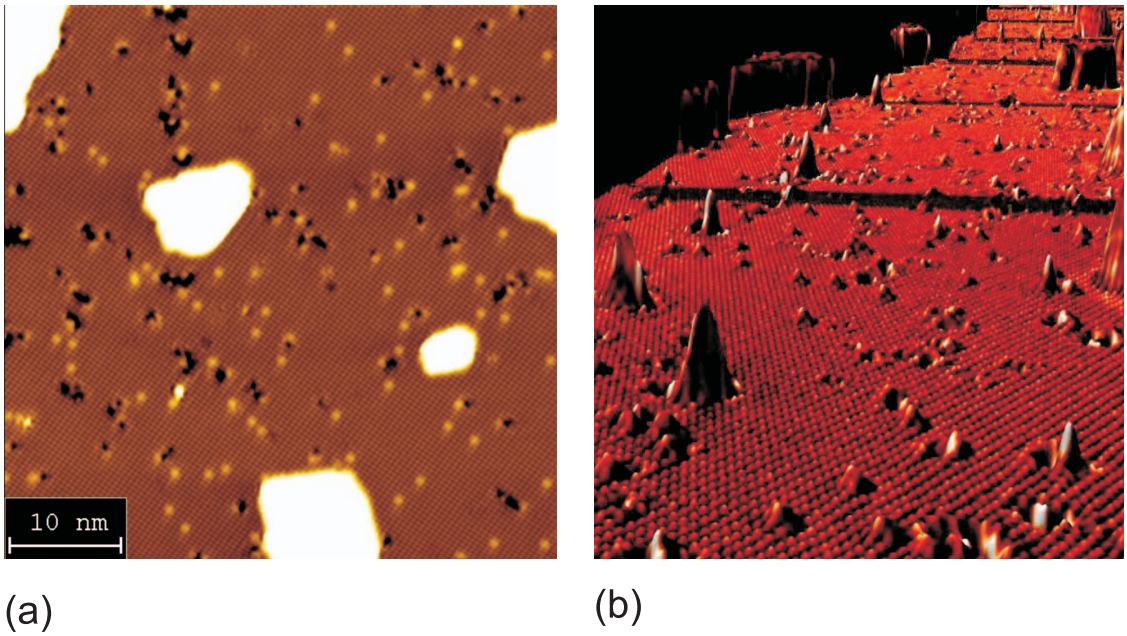

FIG. 48. (Color) Atomic-resolution spin mapping in the presence of surface defects. (a) Larger-scale SP-STM image of the antiferromagnetic Fe monolayer on W(001) with atomic resolution. In addition to the magnetic (2×2) superlattice, atomic-scale defects (vacancies and impurities) as well as second-layer Fe islands (bright features) are visible. (b) Perspective view of several SP-STM images, each $(50\ \text{nm})^2$ in size, which have been put together in order to reveal the perfect Néel-type order of the Fe monolayer on W(001) over an extended surface area and show the degree of reproducibility of atomic-resolution SP-STM imaging.

and is therefore a promising test sample for SP-STM studies. Because of the relatively large unit cell of the complex cubic inverse spinel structure of magnetite, different surfaces may be exposed after different surface treatments. Moreover, sample annealing or Ar^+-ion sputtering may lead to changes in oxygen stoichiometry in the near-surface region. Therefore, a detailed description of the surface preparation and the resulting surface structure has to be given in order to make a useful comparison between results from different experimental studies of magnetite.

The first near-atomic-resolution SP-STM study performed at room temperature was devoted to the (001) surfaces of *in situ* cleaved natural single crystals of magnetite (Wiesendanger, Shvets, *et al.*, 1992a, 1992b, 1992c). While most parts of the cleaved Fe_3O_4 single-crystal surface revealed the (001) plane with tetrahedrally coordinated Fe^{3+} sites (so-called A sites) on top, without exhibiting an interesting surface spin structure, a few parts of the surface showed the C_a and C_b planes with octahedrally coordinated Fe^{2+} and Fe^{3+} sites (so-called B sites) as well as oxygen sites on top. The structure model for these particular $Fe_3O_4(001)$ planes is shown in Fig. 51(a). They consist of Fe rows separated by oxygen sites, resulting in a row spacing of 0.6 nm. These Fe rows change their orientation by 90° from a C_a to a C_b plane, which can be seen in the SP-STM image of Fig. 51(c). Along these Fe rows pairs of Fe^{2+} sites (spin configuration; $3d^{5\uparrow}3d^{\downarrow}$; magnetic moment, $4\mu_B$) and Fe^{3+} sites (spin configuration, $3d^{5\uparrow}$; magnetic moment, $5\mu_B$) alternate, leading to a magnetic superperiodicity of 1.2 nm along these Fe rows, i.e., four times the atomic spacing of 0.3 nm. High-resolution constant-

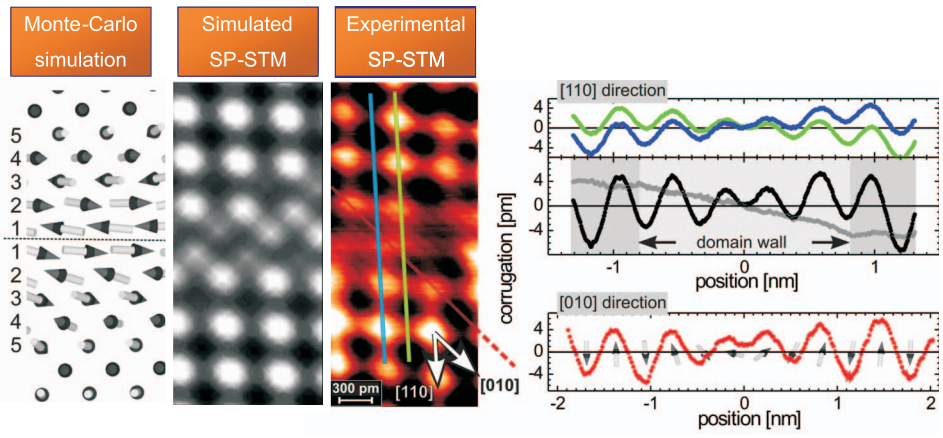

FIG. 49. (Color) Domain wall in the antiferromagnetic Fe monolayer on W(001): comparison between the spin structure as derived from Monte Carlo simulations, simulated SP-STM image based on the calculated spin structure, and experimental atomic-resolution SP-STM data. From Bode, Vedmedenko, *et al.*, 2006.

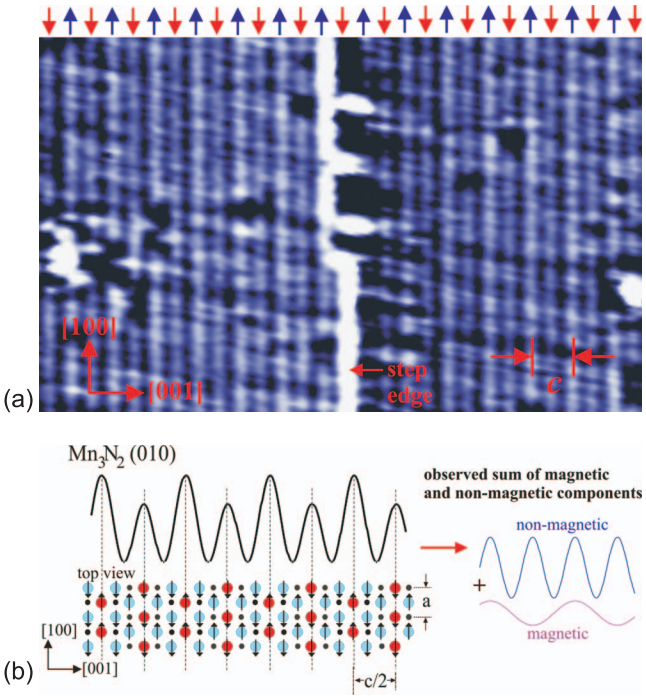

FIG. 50. (Color) Atomic-resolution spin mapping on an antiferromagnetic nitride surface. (a) Constant-current SP-STM image obtained with an in-plane-sensitive Mn-coated W tip showing the antiferromagnetically coupled rows of Mn1 sites on the Mn_3N_2(010) surface. (b) Schematic of the spin structure of Mn_3N_2(010) and a corresponding experimental SP-STM line profile obtained under constant-current conditions. The period of the magnetic modulation amounts to 1.2 nm. From Smith *et al.*, 2005.

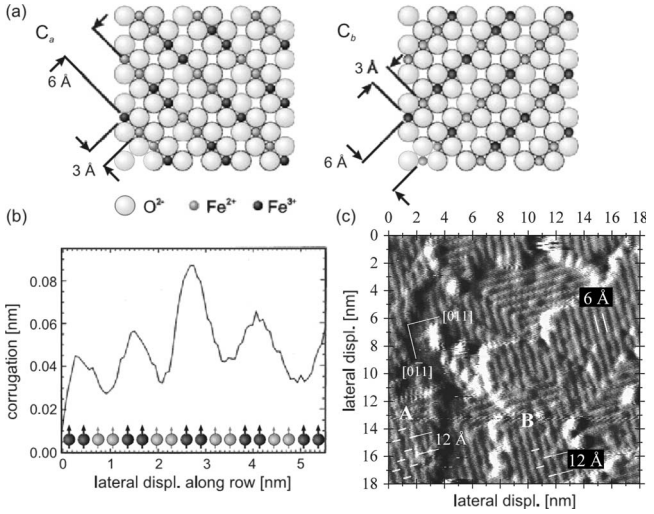

FIG. 51. Atomic-resolution spin mapping on a ferrimagnetic transition metal oxide surface. (a) Schematic structure model of different Fe-O(001) planes of magnetite (Fe_3O_4) exhibiting Fe rows of alternating Fe^{2+} and Fe^{3+} pairs. While the separation of the Fe rows is 0.6 nm, the atomic spacing along the Fe rows is 0.3 nm. The magnetic period along the Fe rows is expected to be four times larger than the atomic spacing, i.e., 1.2 nm. (b) Schematic of the spin structure along the Fe rows of an Fe-O plane of magnetite and a corresponding experimental SP-STM line profile obtained under constant-current conditions. The observed period of 1.2 nm reflects the spin structure of alternating Fe^{2+} and Fe^{3+} pairs (Wiesendanger, Shvets, *et al.*, 1992a). (c) Constant-current SP-STM image of the Fe_3O_4(001) surface revealing the magnetic superstructure period of 1.2 nm along the Fe rows of an Fe-O(001) plane. From Koltun *et al.*, 2001.

current SP-STM experiments performed with Fe tips revealed the magnetic superstructure modulation along the rows of octahedrally coordinated Fe sites of Fe_3O_4(001), as shown in Fig. 51(b). Similar results were obtained for (001) surfaces of synthetic Fe_3O_4 single crystals using ferromagnetic Fe as well as antiferromagnetic MnNi tips (Koltun *et al.*, 2001; Shvets *et al.*, 2004). The formation of Fe^{2+} and Fe^{3+} pairs along the [110]-oriented rows of Fe *B* sites, related to a charge- and spin-ordered state at the (001) surface of magnetite at room temperature, has been explained by an increase in the metal-insulator (Verwey) transition temperature at the surface of magnetite, resulting from the reduced coordination and the correspondingly reduced electronic bandwidth at the surface compared to the bulk (Coey *et al.*, 1993; Wiesendanger *et al.*, 1994; Shvets *et al.*, 2004).

Another atomic-resolution SP-STM study concentrated on oxygen vacancies on the (111) surface of synthetic Fe_3O_4 crystals (Berdunov, Murphy, Mariotto, and Shvets, 2004; Berdunov, Murphy, Mariotto, Shvets, and Mykovskiy, 2004; Murphy *et al.*, 2005). In this case a magnetic-field dependent contrast of electronic states around individual oxygen vacancy sites was revealed by SP-STM using antiferromagnetic MnNi tips.

E. SP-STM studies on individual adatoms

After this discussion of the atomic-resolution capability of SP-STM and its application to various types of antiferromagnetic and ferrimagnetic sample system, the question arises whether the sensitivity of SP-STM can ultimately achieve the level of individual magnetic atoms adsorbed on nonmagnetic substrates. Furthermore, the coupling of individual magnetic atoms and molecules to magnetic substrates as well as the influence of nonmagnetic adatoms on the spin-polarized electronic states of magnetic substrates are interesting topics for SP-STM investigations.

1. Determination of spin states of individual magnetic adatoms on nonmagnetic substrates

Individual magnetic adatoms on a nonmagnetic substrate are the smallest building blocks for magnetic nanostructures that one can imagine. Using STM-based atom manipulation techniques it is possible to construct artificial magnetic nanostructures and to use them as model systems for future nanomagnetic or spintronic devices. Previously, the spatially averaged magnetic properties of an ensemble of magnetic adatoms have been

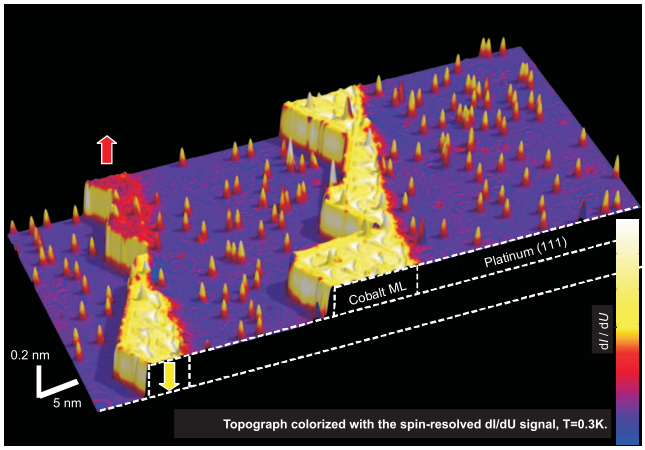

FIG. 52. (Color) SP-STS image showing Co monolayer stripes prepared by step-flow growth on a stepped Pt(111) substrate as well as individual Co adatoms on the bare Pt(111) terraces. Out-of-plane spin contrast of a Cr-coated W tip was verified by revealing the magnetic structure of the out-of-plane magnetized Co nanostripes and the response of the sample to an external magnetic field (see Fig. 31). From Meier *et al.*, 2008.

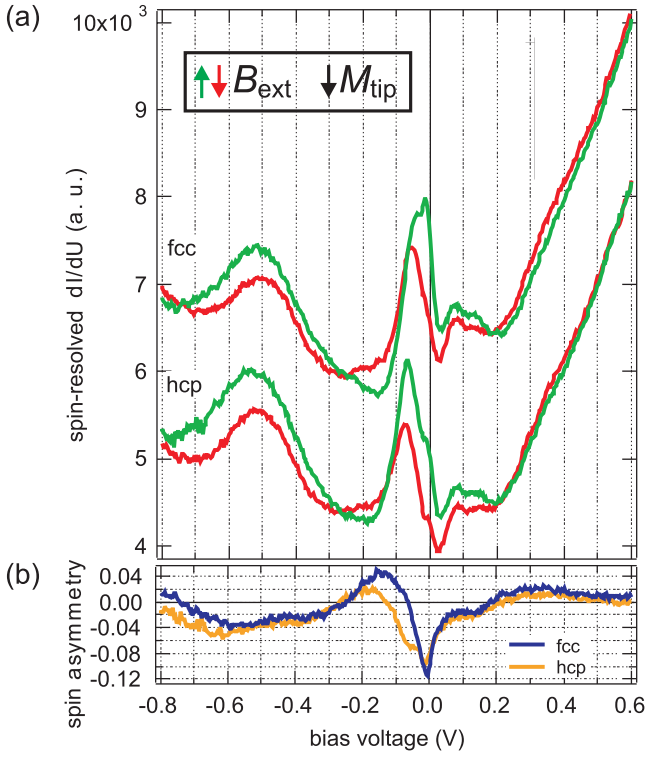

FIG. 53. (Color) SP-STS applied to individual magnetic adatoms. (a) Spin-resolved local differential tunneling conductance spectra measured with an out-of-plane-sensitive Cr-coated tip above individual Co adatoms adsorbed either on fcc or on hcp sites of the Pt(111) substrate. Depending on the relative alignment of the magnetic moments of the tip apex atom and the Co adatoms, different spin-resolved tunneling conductance curves are obtained (red spectra for the parallel case and green spectra for the antiparallel case). (b) The energy-dependent spin asymmetry curves calculated from the spin-resolved tunneling spectra in (a) show quite similar behavior for Co-adatoms adsorbed on fcc and on hcp sites, except for the energy range between –0.2 eV and the Fermi level. From Meier *et al.*, 2008.

investigated by x-ray magnetic circular dichroism (XMCD) (Gambardella *et al.*, 2003). Alternatively, the occurrence of a sharp resonance close to the Fermi level, as observed in local tunneling spectra measured above individual magnetic adatoms (Li *et al.*, 1998; Madhavan *et al.*, 1998), has been exploited to determine the coupling between a magnetic adatom and a metal substrate (Knorr *et al.*, 2002; Wahl *et al.*, 2004) as well as the coupling between two magnetic adatoms mediated by the substrate (Wahl *et al.*, 2007). Since the sharp resonance is usually assigned to the Kondo effect, which originates from the screening of the spin of a magnetic impurity by the surrounding conduction band electrons, it is a rather indirect way of determining the magnetic properties of individual magnetic adatoms. In general, detailed information about the magnetic system under investigation cannot be extracted on the basis of a single parameter (the resonance width, which is related to a characteristic energy scale—the Kondo temperature T_K of the impurity system) extracted from the observation of a Kondo resonance peak. It is therefore a great challenge to perform spin-resolved spectroscopic studies on individual magnetic adatoms by SP-STM and SP-STS.

Application of SP-STM and SP-STS to individual magnetic adatoms brings one into a new regime of sensitivity for spin-resolved microscopy and spectroscopy (Meier *et al.*, 2008). Therefore, it is desirable to have a sample system which allows a calibration of the tip properties by simultaneous observation of the magnetic state of a previously investigated magnetic nanostructure. An example in Fig. 52 shows a SP-STS image of submonolayer Co on a Pt(111) substrate. In a two-stage Co deposition process, nanoscale Co stripes were first prepared by step-flow growth on the stepped Pt(111) substrate, while individual Co adatoms were subsequently deposited at low temperatures, thereby preventing Co adatom diffusion on the Pt surface. Since the system of Co on Pt(111) is known to exhibit out-of-plane magnetic anisotropy, an out-of-plane-sensitive Cr-coated W tip was used for studying the magnetic state of the sample. Indeed, with such tips, the Co monolayer stripes reveal a magnetic domain structure with lateral constrictions acting as pinning sites for domain walls (Fig. 52). The ultimate proof of the magnetic origin of the observed contrast is given by observing the response of the sample to an external magnetic field applied perpendicular to the surface plane (Fig. 31). Once the out-of-plane magnetic contrast on the Co nanostripes is proven, spin-resolved STS measurements can be performed on the simultaneously observed *individual* Co adatoms using the same Cr-coated tip. Figure 53(a) shows the spin-resolved local differential tunneling conductance spectra measured above Co adatoms adsorbed either on fcc or on hcp sites of the Pt(111) substrate. The spectra depend on the relative alignment of the magnetic moments of the Co adatoms, controlled by the direction of the externally ap-

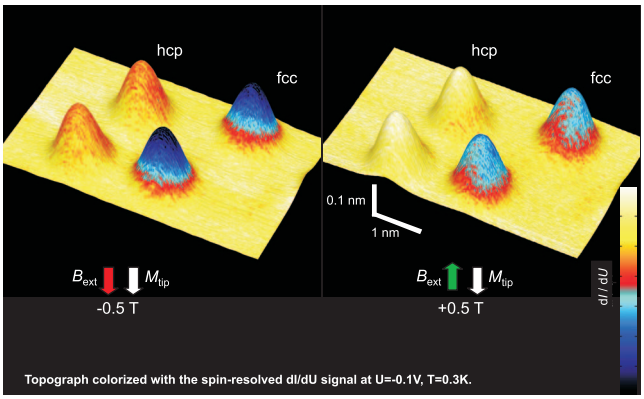

FIG. 54. (Color) SP-STM images of four Co adatoms on Pt(111) obtained with a parallel (left) or antiparallel (right) alignment of the magnetic moments of tip apex atom and Co adatoms. In this case, a sample bias voltage of −0.1 V was chosen for which the electronic contrast, arising from the two inequivalent Co adsorption sites (fcc and hcp), is much stronger than the magnetic contrast arising from the different orientation of the Co moments in the left and in the right image. From Meier *et al.*, 2008.

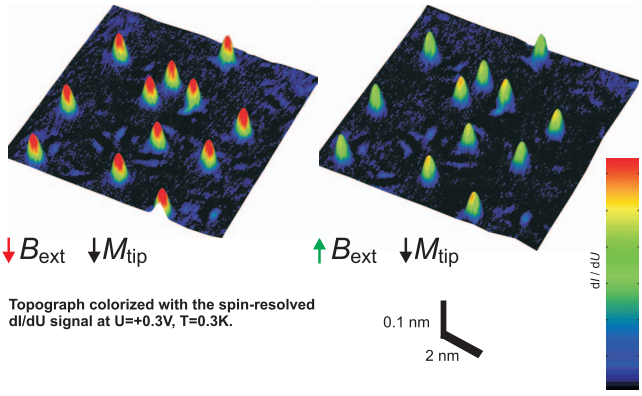

FIG. 55. (Color) Set of two SP-STM images showing several Co adatoms on Pt(111) with their spins aligned either parallel (left) or antiparallel (right) with respect to the spin orientation of the tip apex atom. In this case, a sample bias voltage of +0.3 V was chosen for which the observed contrast difference between the left and the right image is primarily dominated by the different magnetic states of the Co adatoms, while the inequivalent Co adsorption sites cannot be distinguished. From Meier *et al.*, 2008.

plied magnetic field and the tip apex atom. The resulting energy-dependent spin asymmetry curves for the two inequivalent Co adsorption sites, calculated according to Eq. (40), are shown in Fig. 53(b). Both the magnitude and sign of the spin asymmetry change with energy. A major difference between the two inequivalent adsorption sites can be noticed only in a small energy window between −0.2 eV and the Fermi energy, for which electronic contrast effects are expected to dominate over spin-related contrast effects. Indeed, when SP-STS images are recorded at a sample bias voltage of −0.1 V, the electronic contrast difference between Co atoms adsorbed on fcc and hcp sites is much larger than the magnetic contrast originating from the difference between spin-dependent tunneling from a Co adatom with its magnetic moment pointing parallel or antiparallel to the magnetic moment of the tip apex atom (Fig. 54). On the other hand, for a sample bias voltage of +0.3 V, the electronic contrast between Co atoms adsorbed on fcc and hcp sites vanishes and a clear spin-dependent contrast can be observed in SP-STS images of Co adatoms polarized either in the downward or in the upward direction (Fig. 55). The experimental data presented in Fig. 55 prove that the sensitivity of SP-STM and SP-STS is sufficient to reveal the spin state of an individual magnetic atom adsorbed on a nonmagnetic substrate, thereby directly proving the existence of the tunneling magnetoresistance effect for a magnetic single-atom tunnel junction.

Based on the abitilty to measure the spin-resolved differential tunneling conductance above an individual magnetic adatom, a magnetization curve of a single adatom is obtained by plotting the spin-dependent dI/dU signal as a function of the externally applied field (Fig. 56). In this case, the measured quantity is not related to an ensemble-averaged magnetization, as in conventional magnetometry, but rather to a time-averaged magnetization of an individual adatom. The time-averaged component of the magnetization of adatoms $\langle M_A \rangle$ in the external magnetic field direction can be calculated according to

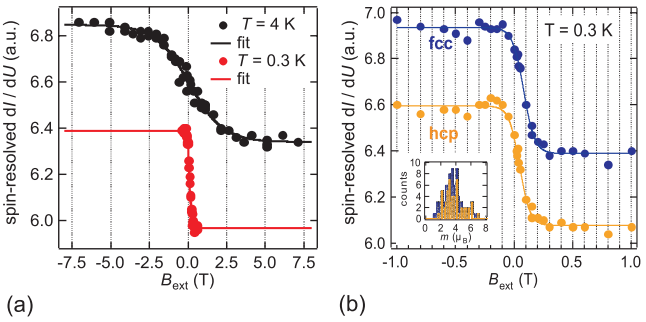

FIG. 56. (Color) Determination of atom-resolved magnetization curves by SP-STS. (a) Experimentally determined magnetization curves for individual Co adatoms on a Pt(111) substrate for two different temperatures: By recording the spin-resolved differential tunneling conductance signal above single Co adatoms as a function of the externally applied magnetic field and by fitting the experimental data according to Eq. (41), the magnetic moment of the Co adatoms can be extracted. (b) Magnetization curves measured at 0.3 K for Co adatoms adsorbed on fcc and on hcp sites. The inset shows the histograms of the extracted magnetic moments of 38 hcp adatoms and 46 fcc adatoms. The significant variation of the extracted magnetic moments is not caused by the difference in the adsorption sites, but must be related with a spin-dependent interaction among the Co adatoms mediated via the Pt substrate in combination with the statistical distribution of the Co adatoms on the substrate. From Meier *et al.*, 2008.

$$\langle M_A \rangle = M_{\rm sat} \frac{\int_0^{2\pi} d\phi \int_0^{\pi} d\theta \sin\theta \cos\theta e^{-E(\theta,B_{\rm ext})/k_B T}}{\int_0^{2\pi} d\phi \int_0^{\pi} d\theta \sin\theta e^{-E(\theta,B_{\rm ext})/k_B T}}, \tag{41}$$

where $E(\theta,B_{\rm ext})=-m(B_{\rm ext}-B_T)\cos\theta-K(\cos\theta)^2$ is the magnetic energy function of the adatom, m is the adatom's magnetic moment, $M_{\rm sat}$ is the saturation magnetization, K is the magnetic anisotropy energy, k_B is Boltzmann's constant, T is the temperature, and $B_{\rm ext}$ is the external magnetic field applied in the easy-axis direction. A residual magnetic stray field of the tip B_t is accounted for using an effective external field ($B_{\rm ext}-B_t$) in the magnetic energy function. By fitting the experimental data obtained at different temperatures with Eq. (41), the magnetic moment m, the saturation magnetization $M_{\rm sat}$, and the tip's residual stray field can be deduced [Fig. 56(a)]. Interestingly, the values for the magnetic moments extracted from the SP-STS data measured at 0.3 K vary considerably (between $2\mu_B$ and $6\mu_B$), while the ensemble-averaged value was found to be in reasonable agreement with results from XMCD measurements (Gambardella *et al.*, 2003). The observed significant variation in the magnetic moment of individual Co adatoms is not caused by the inequivalent Co adsorption sites, as shown in Fig. 56(b), but appears to be related to a spatially inhomogeneous polarization of the Pt substrate resulting from the statistical distribution of the Co adatoms (Meier *et al.*, 2008). This example illustrates the strength of a local probe method for studying magnetic properties of individual adsorbed atoms or molecules, which are strongly influenced by interaction effects mediated by the substrate's electronic states.

The assumption of a long-range magnetic coupling between individual Co adatoms mediated via the Pt(111) substrate has been verified directly by measurements of single-atom magnetization curves for pairs of Co adatoms as a function of their spacing. The sign of the coupling was found to change periodically as a function of distance, i.e., both ferromagnetic and antiferromagnetic coupling between individual Co adatoms was observed depending on their separation. Additionally, the long-range magnetic coupling between individual Co adatoms and a ferromagnetic Co monolayer stripe on a Pt(111) substrate has been studied by SP-STS (Meier *et al.*, 2008). In this case, clear magnetic hysteresis loops have been measured above individual Co adatoms which are indirectly exchange coupled to a ferromagnetic nanostructure [Figs. 57(a)–57(c)]. Based on the dependence of the hysteresis loops on the distance d between the Co adatoms and the Co monolayer stripe, quantitative values for the exchange coupling energy J as a function of d have been extracted [Fig. 57(d)]. A damped oscillatory behavior, which is reminiscent of Ruderman-Kittel-Kasuya-Yoshida (RKKY) like exchange, was revealed, involving a periodic change between ferromagnetic and antiferromagnetic couplings as a function of distance. In contrast, dipolar magnetic coupling will be antiferromagnetic and negligibly small in magnitude [Fig. 57(d)]. In order to test whether a RKKY-type coupling at the single-atom level has indeed been observed, the experimental data points have been fitted using the following range functions with different dimensionalities D (Fischer and Klein, 1975):

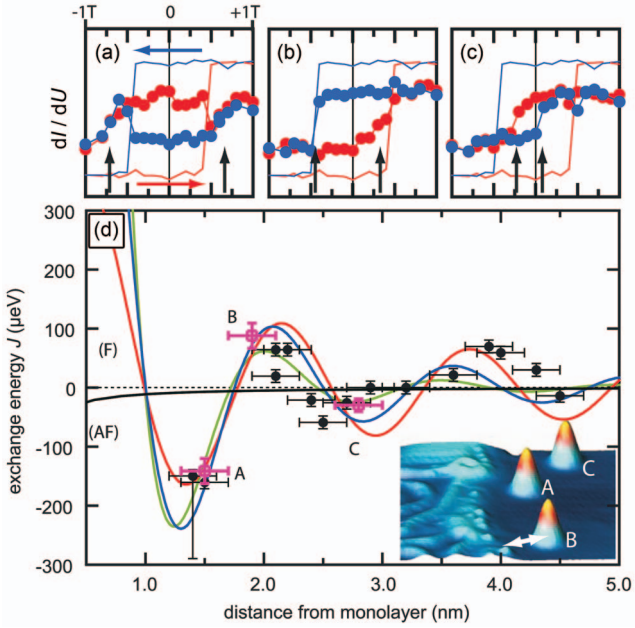

FIG. 57. (Color) Indirect magnetic exchange interaction between Co adatoms and a Co monolayer stripe on a Pt(111) substrate. (a)–(c) Magnetization curves measured on the Co monolayer (straight lines) and on three adatoms (dots) A, B, and C visible in the inset topograph of (d). The black vertical arrows in (a)–(c) indicate the exchange bias fields $B_{\rm ex}$, which can be converted into exchange energy values as plotted in (d) as a function of distance of the Co adatoms from the Co monolayer stripe. The black line in (d) represents the dipolar interaction calculated from the stray field of a 10-nm-wide Co stripe, whereas the red, blue, and green lines are fits to 1D, 2D, and 3D range functions for indirect magnetic exchange interaction. From Meier *et al.*, 2008.

$$J_{\rm RKKY}(d) \propto \frac{\cos(2k_F d)}{(2k_F d)^D}. \tag{42}$$

The good agreement is obtained for $D=1$ and a wavelength of 3 nm, corresponding to an oscillation period of the exchange energy of 1.5 nm. A dimensionality below 2 is expected if the interaction is dominated by surface-related electronic states, and the superposition of the contributions from all Co atoms along the stripe edge attenuates the decay of the indirect exchange interaction as a function of distance of the individual Co adatom. The observed period of the oscillation is found to be larger than typical Fermi wavelengths of the Pt(111) surface (Wiebe *et al.*, 2005). However, effects similar to those found in layered metallic systems explaining the long-period oscillation of the interlayer exchange cou-

pling (Bruno and Chappert, 1992) can also play a crucial role in the stripe-adatom interaction.

2. Spin states of individual magnetic adatoms on magnetic substrates

In the above-mentioned case the spin direction of the individual magnetic adatoms was fixed and determined by an external magnetic field, but it is also possible to observe stationary spin states of individual magnetic adatoms that are exchange coupled to a magnetic substrate. For instance, individual Fe and Cr atoms adsorbed on nanoscale Co islands on Cu(111) were studied by SP-STS at a temperature of 5 K (Yayon *et al.*, 2007). Using out-of-plane-sensitive Cr-coated W tips it was found that the Fe and Cr adatoms exhibit an out-of-plane orientation of their magnetic moments, similarly to the nanoscale Co islands on Cu(111) (see Sec. IV.C). Moreover, analysis of spin-resolved differential tunneling conductance spectra measured above Fe and Cr adatoms adsorbed on two oppositely magnetized Co islands showed that the Fe adatoms coupled ferromagnetically to the Co moments, while the Cr adatoms coupled antiferromagnetically. This example illustrates that exchange coupling is effective even at the level of individual adsorbed atoms, which explains why atomically sharp magnetic tips can provide a stable spin contrast in SP-STM and SP-STS data without being limited by spin fluctuations.

3. Spin-dependent scattering at single nonmagnetic atoms on magnetic substrates

SP-STM and SP-STS can also be applied to study spin-dependent scattering states around individual impurity adatoms on magnetic substrates. An important example is given by chemisorbed oxygen atoms on highly reactive transition-metal substrates, such as iron. By preparation of single oxygen atoms on an Fe(110) substrate, the spin-dependent scattering of Fe electrons with *d*-like symmetry can be directly revealed in real space by SP-STS (von Bergmann, Bode, Kubetzka, *et al.*, 2004). The spatial distribution of scattering states is known to reflect the orbital character of the electronic states involved in the scattering. While circular-symmetric scattering states are observed around adatoms on noble-metal (111) substrates (see Fig. 43), the shape of the scattering state observed in Fig. 58 reflects the *d*-orbital symmetry of the Fe electronic states at the particular energy determined by the applied sample bias voltage. Moreover, by observation of the scattering states around individual oxygen atoms chemisorbed on oppositely magnetized Fe(110) surface areas, the spin character of the scattering states can be determined unambiguously. This is accomplished by analyzing the relative strength of the scattering for the two different spin channels. It was found that the scattering of minority-spin electrons of Fe is much stronger than that of majority-spin electrons, in agreement with theoretical studies (von Bergmann, Bode, Kubetzka, *et al.*, 2004). As a consequence, the microscopic origin of magnetoresistance effects, arising from the presence of impurities, can be traced back directly to the spin-dependent scattering at the atomic level.

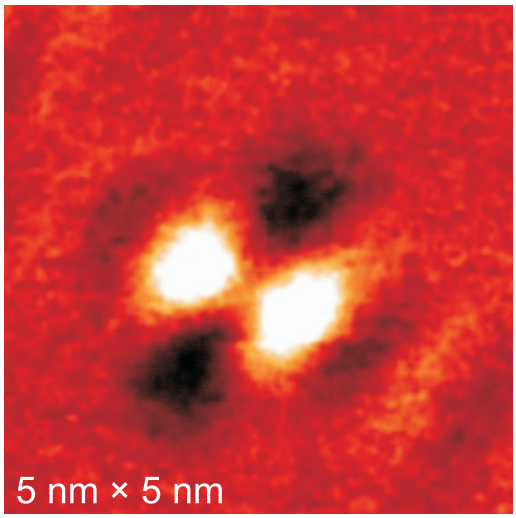

FIG. 58. (Color) SP-STS image showing a spin-dependent scattering state arising from a single oxygen atom chemisorbed on a Fe(110) substrate. The contrast originates from the scattering of minority-spin electronic states of *d*-like symmetry as revealed experimentally by the spatial distribution of the scattering state and the relative strength of the scattering for the minority- and majority-spin channels. The interpretation has been supported by *ab initio* spin-resolved electronic structure calculations. From von Bergmann, Bode, Kubetzka, *et al.*, 2004.

F. Magnetization dynamics and spin transport phenomena

1. Thermally induced magnetization switching in nanoislands

In the previous sections, the focus was on applications of SP-STM in magnetic imaging of static domain configurations in thin films as well as investigating spin states of nanoislands and single atoms that are stable in time due to exchange coupling to a magnetic thin film or the presence of an external magnetic field. In the following, it will be shown that time-resolved SP-STM studies allow insight into the thermal switching behavior of superparamagnetic nanoislands and single paramagnetic spins. The unambiguous interpretation of such data necessarily requires antiferromagnetic SP-STM probe tips because the magnetic stray field of a ferromagnetic tip would modify the intrinsic magnetic switching behavior of nanoislands or single atoms.

Since scanning microscopy techniques usually suffer from a limited time resolution because the data are recorded sequentially, alternative modes of operation, such as the line or point mode, have been introduced for the investigation of dynamic phenomena. In these modes, one or even two scanning directions are given up in order to improve the time resolution in the SP-STM experiment.

A typical experimental procedure starts with observing the spatial distribution of magnetic nanoislands or

magnetic atoms before selecting an individual nano-object for time-resolved study. Subsequently, the SP-STM tip is held stationary above the individual magnetic nano-object and the spin-resolved tunneling current or the spin-resolved differential tunneling conductance signal is recorded as a function of time.

The first time-resolved SP-STM study of the thermal switching behavior of magnetic nano-objects focused on perpendicularly magnetized nanoscale Fe islands of single atomic layer height on a Mo(110) substrate using out-of-plane-sensitive Cr-coated W tips (Bode, Pietzsch, *et al.*, 2004; Bode, Kubetzka, von Bergmann, *et al.*, 2005). While Fe islands with an area larger than 40 nm^2 were observed to be magnetically stable at the measurement temperature of $T=13$ K, smaller Fe islands exhibited a time-dependent spin contrast (either between two subsequent scan lines within one particular SP-STM image or between subsequent SP-STM images; see Fig. 59). Interestingly, it was found that the magnetic switching rate of the Fe nanoislands is not only determined by their size, but also strongly affected by their shape, i.e., elongated islands switch much more rapidly than compact islands of the same volume (Bode, Pietzsch, *et al.*, 2004). This experimental observation has been explained by different processes of magnetization reversal for compact and elongated islands.

For compact islands, the switching rate ν can be derived under the assumption of a coherent rotation of magnetization, i.e., at any time—even during the magnetic switching—the magnetic moments of the entire island remain oriented in the same direction, behaving like a single giant spin (Brown, 1963),

$$\nu = \nu_0 \exp(-E_B/k_B T) \tag{43}$$

with the attempt frequency ν_0, the energy barrier E_B that separates two magnetization states (e.g., up and down), the Boltzmann constant k_B, and the temperature T. The energy barrier for this type of magnetization reversal is given by the material-specific anisotropy energy density constant K times the magnet's volume V,

$$E_B = KV. \tag{44}$$

Most previous experimental studies of magnetic switching behavior have been performed on ensembles of nanoparticles which were supposed to be identical. Since the switching rate ν depends exponentially on the particle's volume, even a relatively narrow size distribution may cause a significant variation in the switching rate. Furthermore, the Néel-Brown law [Eq. (43)] is not generally applicable for irregularly shaped nanoparticles or nanoislands. The magnetization reversal mechanism may be completely different for elongated particles compared to compact ones. In particular, it has been predicted theoretically (Braun, 1993, 1994) that for elongated particles that exceed a critical length, determined by the exchange stiffness A and the effective anisotropy constant K, the nucleation of a reversed domain in the interior of the sample is possible because the energy barrier related to domain-wall creation in an elongated particle with a small cross section F given by

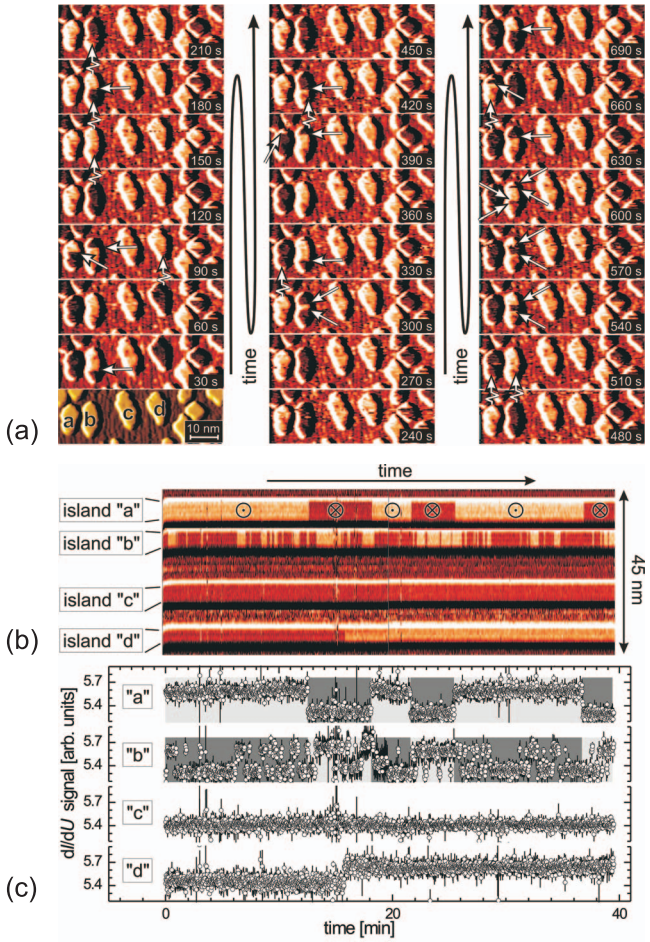

FIG. 59. (Color) Time-resolved SP-STS on individual nanoislands. (a) Topographic STM image (bottom left) and 23 successive spin-resolved dI/dU maps of four superparamagnetic Fe nanoislands on Mo(110) labeled a–d. Magnetic switching events that were directly observed are marked by straight arrows while zigzag arrows indicate switching events that must have occurred when the tip did not scan across the particular islands. (b) Time- and spin-resolved dI/dU signal of the four nanoislands shown in (a). Since the position of the slow scanning direction is fixed, this direction represents the time rather than a lateral scale. The total observation time is about 40 min with a 1 s increment. Five switching events of island *a* can be recognized. (c) Averaged line profiles drawn along the time axis. The effect of the dipolar coupling between islands *a* and *b* is highlighted by the differently shaded regions. From Bode, Kubetzka, von Bergmann, *et al.*, 2005.

$$E_B = 2F(AK)^{1/2} \tag{45}$$

becomes lower than the energy barrier for coherent rotation of magnetization. The experimental SP-STM results support this theoretical prediction of a shape-dependent magnetization reversal process.

Moreover, the interparticle distances should be experimentally accessible in order to quantify the effect of dipolar interactions on the particle's intrinsic switching rate at small interparticle spacings. The influence of such

dipolar interactions on the switching behavior of closely spaced nanoislands is shown in Fig. 59(a), where the time-dependent magnetization states of the two Fe islands *a* and *b* are strongly correlated because the dipolar interaction between these two neighboring islands leads to preference for an antiparallel alignment of their magnetization directions.

In conclusion, a careful characterization of the size and shape of individual nanoparticles or nanoislands, as well as the determination of interparticle spacings, is required in order to determine the magnetic switching behavior of nanoscale objects (Krause *et al.*, 2009). SP-STM is a powerful technique because detailed structural and morphological information can be combined directly with the observation of time-dependent magnetic states at the nanoscale.

As the size of the nanoscale object is further reduced to the ultimate limit of single atoms, the characteristic time scale for magnetic switching decreases and one might expect that it will become more difficult, even in the point mode, to resolve these fast switching events with time-dependent measurements of the spin-resolved tunneling current or tunneling conductance. However, it has been theoretically predicted that SP-STM might be a useful technique to perform "noise spectroscopy" of a single spin, thereby directly probing the highly disordered quantum states of a microscopic system (Nussinov *et al.*, 2003).

2. Spin-current-induced magnetization switching across a vacuum barrier

It has been predicted theoretically that the magnetization state can also be switched by spin-polarized currents which locally exert a spin torque leading to the reversal of magnetization at sufficiently high current densities (Berger, 1996; Slonczewski, 1996). While this effect was first experimentally observed in magnetic multilayer structures with a nonmagnetic metallic spacer layer sandwiched between two magnetic layers (Tsoi *et al.*, 1998; Myers *et al.*, 1999), it was only recently that a spin-polarized STM was used to demonstrate spin-current-induced magnetization switching across a vacuum barrier (Krause *et al.*, 2007). In combination with the ultimate lateral resolution of SP-STM, a separation between the Oersted field and true current-induced spin torque effects could be achieved, thereby providing insight into the microscopic processes of current-induced magnetization switching. This experiment demonstrated that the same SP-STM setup can be used to both manipulate and read out the magnetization of nanoscale Fe islands consisting of only 100 atoms.

3. SP-STM studies of magnons

In addition to the investigation of dynamic and transport phenomena in the time domain, SP-STM may be applied to study magnetic excitations in the frequency domain. This can be accomplished by combining SP-STM with inelastic electron tunneling spectroscopy (IETS), which is a well-established technique for planar tunnel junctions (Wiesendanger, 1994a). The tunneling electron may lead to excitation of an object placed in the gap between the two electrodes of the tunnel junction or in the electrodes themselves if its energy eU is equal to or larger than the energy of the excitation. Since the number of possible final states increases, the tunneling current is enhanced. This leads to a step in the differential tunneling conductance at the energy of the excitation and, accordingly, to a peak in the second derivative $d^2I/dU^2(U)$.

Inelastic scanning-tunneling spectroscopy (ISTS) has been well established in studies of vibrational excitations of single molecules placed between the STM tip and a metallic substrate (Stipe *et al.*, 1998). Recently ISTS has been applied to observe spin flips of single atoms and spin excitations in atomic chains exposed to an external magnetic field (Heinrich *et al.*, 2004; Hirjibehedin *et al.*, 2006, 2007). It has been possible to directly measure the energy required to flip the spin of a single adsorbed Mn atom and to probe the interactions between spins in linear atomic chains of up to ten Mn atoms. While these studies have been performed with conventional nonmagnetic probe tips, the ultimate goal would be a combination of inelastic and spin-resolved scanning-tunneling spectroscopy for atomic-scale studies of spin states and spin excitations.

The application of inelastic SP-STM to observe the local excitation of magnons has already been demonstrated using bulk Fe samples and thin films of Co grown on Cu(111) substrates (Balashov *et al.*, 2006). Recording of inelastic tunneling spectra with Fe-coated W tips in an external magnetic field has given a strong indication of the magnonic nature of the excitation. It was found that the cross section for magnon excitation scales linearly with the Co film thickness. Future inelastic and spin-resolved STS studies may allow the investigation of magnons in laterally confined nanoscale structures or the study of localized magnon modes in the vicinity of single magnetic impurities.

G. New developments

The previous sections have provided numerous examples of applications of SP-STM where theoretically predicted magnetic states could be verified experimentally for the first time thanks to the unprecedented real-space resolution of SP-STM, e.g., the antiferromagnetic ground states of single atomic layers of Mn on W(110) and Fe on W(001), the topological antiferromagnetic order of the Cr(001) surface, the atomically sharp domain walls in ferromagnetic atomic layers of Fe on W(110), or the quantitative determination of the magnetic vortex core width in mesoscopic-scale magnetic islands. However, SP-STM has also led to discoveries of new magnetic states in ultrathin films. Three examples will be presented in the following sections.

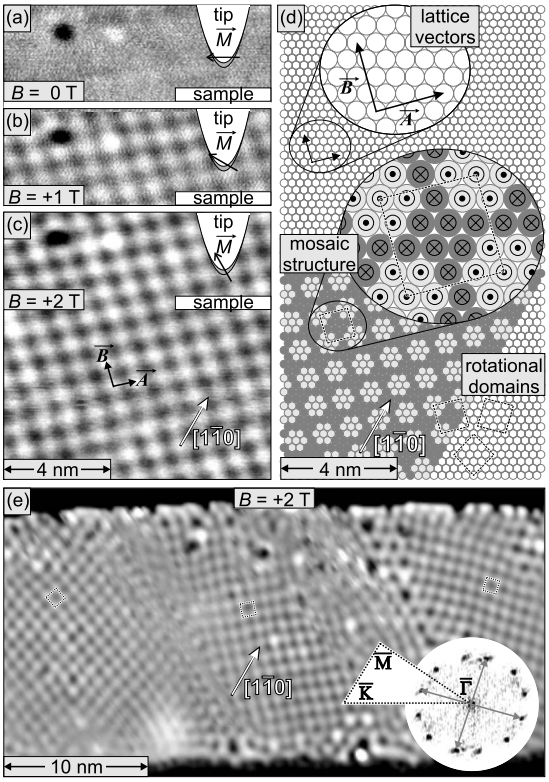

FIG. 60. Discovery of a novel complex nanoscale magnetic structure in a Fe monolayer pseudomorphically grown on an Ir(111) substrate. (a) SP-STM image obtained with an in-plane-sensitive Fe-coated W tip showing no magnetic contrast. (b), (c) Magnetic superstructure of Fe on Ir(111) as revealed with an out-of-plane magnetized Fe-coated W tip in different external magnetic fields. (d) Spin structure model for the Fe monolayer on Ir(111) based on the experimental SP-STM data. (e) SP-STM image revealing all three possible rotational domains of the magnetic superstructure found on Fe/Ir(111). From von Bergmann, Heinze, *et al.*, 2006.

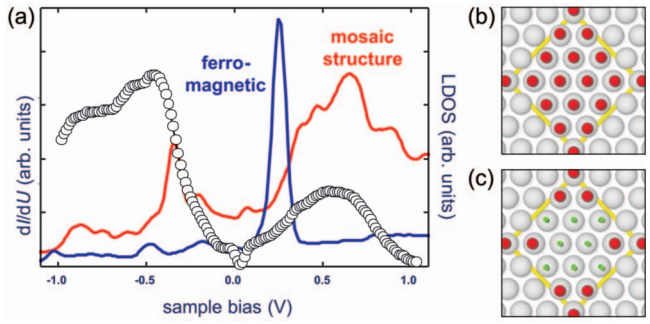

FIG. 61. (Color) Electronic structure of the Fe monolayer on Ir(111). (a) Experimental $dI/dU(U)$ spectrum for 1 ML of Fe on Ir(111) compared to the calculated vacuum LDOS of (b) an assumed ferromagnetic state and (c) for the mosaic spin structure model. From von Bergmann, Heinze, *et al.*, 2006.

1. Novel types of magnetic order at the nanoscale

A complex magnetic structure with a nanometer-sized two-dimensional magnetic unit cell was discovered by SP-STM applied to Fe monolayers pseudomorphically grown on an Ir(111) substrate (von Bergmann, Heinze, *et al.*, 2006). While in-plane-sensitive Fe-coated W tips were unable to reveal any magnetic structure for this particular system at a temperature of 13 K [Fig. 60(a)], a clear magnetic contrast was seen using out-of-plane magnetized probe tips [Figs. 60(b) and 60(c)], indicating the presence of out-of-plane magnetic anisotropy. Interestingly, an approximately square-shaped magnetic unit cell with a lattice constant of about 1 nm was found, consisting of 15 atoms. Due to the sixfold symmetry of the hexagonal lattice of the Ir(111) substrate, three rotational domains can be expected to occur, which are simultaneously observed in the large-scale SP-STM image of Fig. 60(e). Assuming for simplicity a collinear spin structure with perpendicularly orientated surface spins, in agreement with the experimental SP-STM results obtained with in-plane- and out-of-plane-sensitive probe tips, a 7:8 mosaic spin structure can be derived where seven spins point in one direction and eight spins in the opposite one [Fig. 60(d)]. Since different domains of the proposed mosaic spin structure will exhibit an 8:7 ratio equally as likely as the 7:8 ratio of spin-up and spin-down sites, a net zero magnetization state of the Fe monolayer film results, as would be the case for an antiferromagnetically ordered state. Interestingly, the proposed mosaic spin structure exhibits both ferromagnetically and antiferromagnetically coupled nearest-neighbor sites. Based on *ab initio* electronic structure calculations it was shown that the total energy of the proposed mosaic spin structure is indeed lower than that of a pure ferromagnetic or a pure antiferromagnetic state. Moreover, by comparison of the experimental tunneling conductance spectrum for the Fe monolayer on Ir(111) with the caculated vacuum LDOS of an assumed ferromagnetic state and the proposed mosaic spin structure (Fig. 61), one can see that the LDOS for a ferromagnetic Fe monolayer on Ir(111) would not fit the experimental data at all, whereas the agreement between experiment and theory is remarkably good based on the mosaic spin structure model.

While the presence of spin frustration for several sites of the proposed mosaic spin structure can be expected to lead to deviations from collinearity, the lack of in-plane magnetic contrast in the experimental SP-STM data as well as the good agreement of the calculated LDOS with the measured tunneling spectrum under the assumption of a collinear magnetic state suggest that the true magnetic structure of the Fe monolayer on Ir(111) cannot be much different from the proposed collinear spin structure model displayed in Fig. 60(d). Many similar complex nanomagnetic states can be expected to occur in ultrathin magnetic films, which previously have remained undetectable due to either a lack of spatial resolution or the limited sensitivity of conventional magnetic characterization techniques.

2. Spin spirals in ultrathin films as examples of noncollinear spin structures

While the previous example illustrated that complex collinear magnetic structures can exist with nanometer-

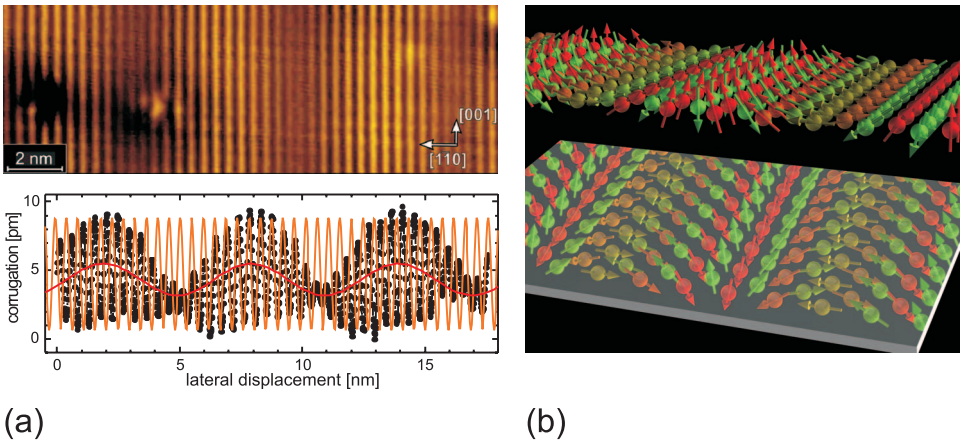

FIG. 62. (Color) Discovery of a surface-related spin spiral state by SP-STM. (a) SP-STM image of a single monolayer of Mn pseudomorphically grown on a W(110) substrate. In addition to the local antiferromagnetic order on the atomic scale, an additional long-wavelength modulation having a periodicity of about 6 nm is observed, which is due to a spin spiral state (Bode *et al.*, 2007). (b) Schematic of the spin spiral having a unique sense of rotation, or chirality, with respect to the surface that is different from its mirror image. From P. Ferriani.

sized magnetic unit cells, other types of complex magnetic states based on noncollinear spin structures were already predicted (Wortmann *et al.*, 2001, 2002; Heinze *et al.*, 2002). It was pointed out that SP-STM can play a key role in the verification of such noncollinear spin states, which typically occur in magnetically frustrated layers of antiferromagnetic materials on triangular (111) substrate lattices.

Another type of noncollinear spin structure, a so-called spin spiral, has recently been discovered by SP-STM on a single atomic layer of Mn pseudomorphically grown on a W(110) substrate (Bode *et al.*, 2007). While we learned in Sec. IV.D.1 that such a monolayer of Mn on W(110) is antiferromagnetically ordered on the local scale (Heinze *et al.*, 2000), an additional long-wavelength modulation is visible in larger-scale SP-STM images, as shown in Fig. 62(a). SP-STM experiments with in-plane- as well as out-of-plane-sensitive magnetic probe tips allowed the observed supermodulation to be attributed to a spin spiral state, whereas a spin-density-wave state was ruled out. The observed spin spiral exhibits a unique sense of rotation, or chirality, with respect to the surface, and can be attributed to the Dzyaloshinskii-Moriya interaction (Dzyaloshinskii, 1957; Moriya, 1960) which arises from spin-orbit scattering of electrons in an inversion-asymmetric crystal field,

$$E_{\mathrm{DM}} = \sum_{i,j} \vec{D}_{ij} \cdot (\vec{S}_i \times \vec{S}_j). \tag{46}$$

Here $\vec{S}_{i,j}$ denotes the spin on the atomic site i (j) and $\vec{D}_{ij}$ is the Dzyaloshinskii-Moriya vector. Since low-dimensional systems, such as single atomic layers on metal substrates, generally lack structural inversion symmetry, homochiral spin structures [Fig. 62(b)] may occur. Another surface-related spin spiral state was found by SP-STM for a single atomic layer of Mn on a W(001) substrate, but in this case with a much smaller spin spiral periodicity, leading to a strong noncollinearity of neighboring Mn spins (Ferriani *et al.*, 2008).

While spin spirals were previously known to occur in bulk crystals that lack inversion symmetry, the discovery of chiral spin structures in nanoscale magnets by SP-STM may play an important role in spintronic devices because a spin-polarized current flowing through a chiral magnetic structure will exert a spin torque on the magnetic structure. Ultimately, the concepts of spin-current-induced magnetization switching across a vacuum gap, introduced in Sec. IV.F.2, may be applied to chiral magnetic nanostructures.

3. Spin-resolved imaging through adsorption layers or ultrathin nonmagnetic metal films

Since magnetic transition and rare-earth metals are highly reactive, the application of SP-STM has been limited to ultrahigh-vacuum conditions so far. It remains a challenging future task to find chemically inert overlayers which allow for high-resolution spin mapping by SP-STM through such overlayers even under ambient conditions.

A first step toward this goal has been made by investigating Fe nanoislands in a magnetic vortex state by SP-STM before and after adsorption of sulfur (Berbil-Bautista *et al.*, 2006). A comparison between spin-resolved $dI/dU(U)$ spectra before and after sulfur adsorption shows that the spin-resolved local density of states of the Fe nanoislands prepared on a W(110) substrate is only weakly modified due to the presence of a $c(3\times1)$ sulfur overlayer which is manifested by an almost rigid shift in energy of the most prominent features in the tunneling spectra (Fig. 63). As a result, the magnetic vortex state of the Fe nanoislands can still be imaged through the sulfur layer by SP-STM, though with a reduced signal-to-noise ratio. The observed behavior for sulfur adsorbed on Fe/W(110) is in strong contrast to the chemisorption of oxygen on the same magnetic sub-

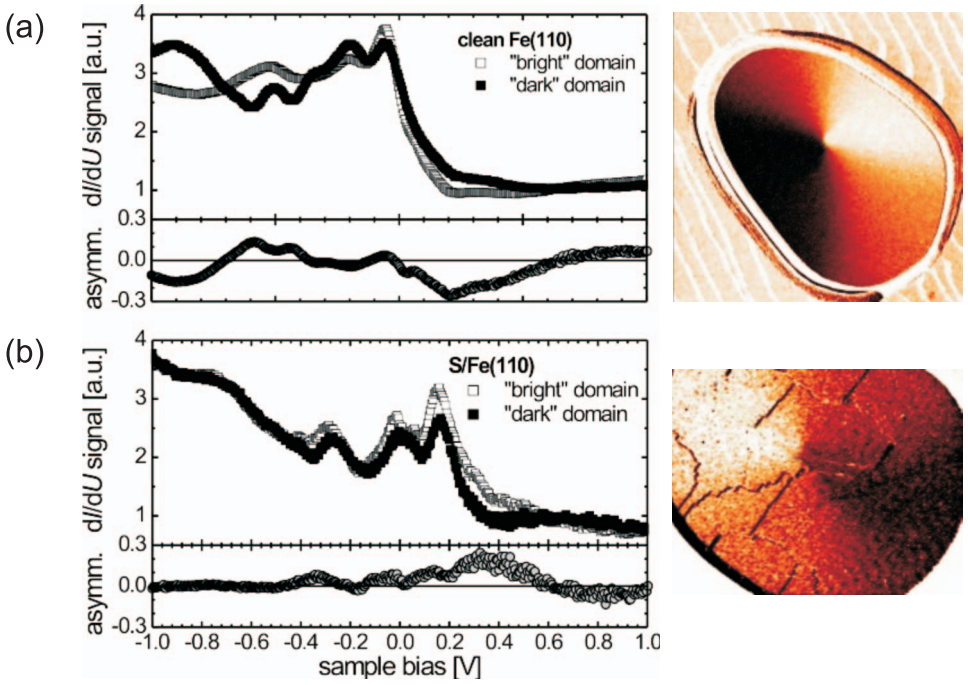

FIG. 63. (Color) Magnetic imaging through adsorption layers. (a) Spin-resolved $dI/dU(U)$ spectra and spatially resolved SP-STM (350×350 nm^2) data of a clean Fe nanoisland in a magnetic vortex state prepared on a W(110) substrate. (b) Spin-resolved $dI/dU(U)$ spectra and spatially resolved SP-STM data of a similar Fe nanoisland covered by a $c(3\times1)$ sulfur layer. The adsorption of sulfur leads only to a weak perturbation of the spin-resolved electronic structure of the Fe nanoisland thereby still allowing the spin-resolved mapping of the magnetic vortex state through the adsorption layer. From Berbil-Bautista *et al.*, 2006.

strate. In the latter case a drastic change in the spin-resolved electronic structure even at significantly lower oxygen coverage is found (see Fig. 58). Since sulfur and other chalcogenides are known to lead to inert surfaces, e.g., in transition-metal dichalcogenides which can easily be imaged by STM with atomic resolution even under ambient conditions, a sulfur coverage equivalent to a closed monolayer may be sufficient to lead to a chemically nonreactive surface.

Another approach for getting a chemically inert surface for SP-STM studies under ambient conditions is the use of noble-metal overlayers, such as Au or Pt. It was shown that SP-STM imaging of magnetic domain walls at Co(0001) single-crystal surfaces is possible through ultrathin Au films that are 1.3 or 2.6 ML thick (Wulfhekel, 2005). The spin contrast was found to decrease only weakly with increasing Au thickness, thereby demonstrating that SP-STM imaging through a protective metal layer is possible. The experimental observations can be explained by the slow decay of the electron spin polarization as a function of the thickness of the nonmagnetic overlayer. The spin-scattering length usually exceeds the mean free path of the electrons, being on the order of several tens of nanometers in the case of Au.

While the spin information is carried through the nonmagnetic metal overlayer, a serious concern is the modification of the interface magnetic anisotropy upon the adsorption of a nonmagnetic metal on a magnetic thin film. Therefore, the challenge remains to identify the most suitable chemically inert overlayer material leading to a negligible perturbation of the magnetic state of the system investigated while carrying the spin information up to the surface probed by SP-STM.

V. MAGNETIC EXCHANGE FORCE MICROSCOPY

While SP-STM and SP-STS have provided insight into magnetic domain structures and atomic spin configurations at surfaces, the applications of these methods is limited to electrically conducting samples such as magnetic metals or magnetic semiconductors. In order to reveal atomic spin structures at surfaces of insulators and to open up the exciting possibility of studying spin ordering effects with atomic resolution while going through a metal-insulator transition, a force-microscopy-based technique is needed. A new type of magnetic microscopy, i.e., magnetic exchange force microscopy (MExFM), has recently been introduced (Kaiser *et al.*, 2007), involving detection of the short-range spin-dependent exchange and correlation forces at very small separations (typically 0.3–0.5 nm) between a magnetic tip and a magnetic sample.

A. Principles and methods of MExFM

In contrast to the well-established magnetic force microscopy (MFM) technique (Martin and Wickramasinghe, 1987; Sáenz *et al.*, 1987), which is based on the detection of long-range magnetic dipole forces at typical tip-to-surface distances of 10–20 nm achieving a lateral resolution of 10–50 nm (Hartmann, 1999; Schwarz *et al.*, 2004, 2007; Abelmann *et al.*, 2005), MExFM aims at a combination of atomic force microscopy (AFM) (Binnig *et al.*, 1986) with in-plane atomic resolution and single-spin sensitivity. An important starting point for achieving atomic-resolution spin mapping on surfaces of insulators is the development of noncontact atomic force microscopy (NC-AFM) with true atomic resolution (Giessibl, 1995, 2003). Currently NC-AFM allows atomically resolved studies of any material system (Morita *et*

al., 2002), even in the case of curved surface topographies (Ashino *et al.*, 2004). MExFM combines the possibilities of NC-AFM with atomic-scale spin resolution using atomically sharp magnetic probe tips with a well-defined spin state at the tip apex.

As for SP-STM the relative orientation of the spins of the tip apex atom and the surface atoms is important for MExFM. According to the Heisenberg model the magnitude of the interaction between two spins $\vec{S}_1$ and $\vec{S}_2$ is given by their scalar product:

$$H = J_{12}\vec{S}_1 \cdot \vec{S}_2, \tag{47}$$

where J_{12} is the exchange integral. Thus, the interaction between the spins of tip and sample is strongest for either parallel or antiparallel spin orientations.

The knowledge gained during the development of SP-STM in preparing tips with a well-defined spin orientation (see Sec. III.A) has proven to be indispensable for the success of MExFM experiments. Typically, an ultrathin layer of Fe is evaporated *in situ* in UHV onto Si tips that are integrated into Si-based AFM cantilevers. Such Fe-coated tips are sensitive to the in-plane surface spin component, like the Fe-coated W tips used for SP-STM studies. An external magnetic field of up to several tesla can be used to reorient the magnetization of the Fe-coated tip into the direction along the tip axis, i.e., perpendicular to the sample surface plane, thereby making the tip sensitive to the out-of-plane surface spin component. Such ferromagnetic Fe-coated probe tips are useful for the investigation of antiferromagnetic material systems, as discussed in the following section. However, if ferromagnetic insulators are to be investigated by MExFM, the use of ferromagnetic probe tips has to be avoided in order to exclude the disturbing influence of dipolar magnetic interactions. Such dipolar interactions, which are inherently present in conventional MFM experiments, can perturb the intrinsic magnetic state of the sample or modify the magnetic state of the probe tip during imaging, particularly at small tip-sample separations. Therefore, antiferromagnetic MExFM probes, such as Cr-coated Si tips, are prefered in order to avoid magnetic stray fields from the tip.

While both static and dynamic modes of AFM operation are known, MExFM makes use of the dynamic mode where the cantilever oscillates with amplitude A, self-excited at or near the resonance frequency

$$\omega_0 = 2\pi f_0 = \sqrt{c_z/m}, \tag{48}$$

where c_z is the spring constant of the cantilever and m is its effective mass. In the dynamic mode of AFM operation the measured signal is related to the force gradient F_z'. To calculate F_z' one assumes that the spring constant of the cantilever is effectively softened or hardened by an attractive or repulsive interaction, respectively,

$$c_{\text{eff}} = c_z - F_z'. \tag{49}$$

As a result, the actual oscillation frequency ω deviates from the frequency ω_0 of the free noninteracting cantilever by

$$\Delta\omega = \omega - \omega_0. \tag{50}$$

The minimal detectable force gradient is limited by all kinds of external noise sources and by the sensitivity of the deflection sensor (Albrecht *et al.*, 1991),

$$\partial F_{\text{min}}/\partial z = \sqrt{4c_z k_B T B/\omega_0 Q\langle A^2\rangle}, \tag{51}$$

where k_B is Boltzmann's constant, T is the temperature, B is the measurement bandwidth, Q is the quality factor of the oscillator, and $\langle A^2\rangle$ is the mean square amplitude of the cantilever oscillation. It immediately follows from Eq. (51) that high-sensitivity dynamic AFM measurements necessarily require soft cantilevers, low temperatures, and a high Q factor, achieved under UHV conditions. The development of UHV-AFM instruments which can operate at low temperatures (Allers *et al.*, 1998; Liebmann *et al.*, 2002) proved to be important for the development of MExFM (Kaiser *et al.*, 2007).

B. Applications of MExFM

1. Antiferromagnetic insulators

The ultimate test system for MExFM with atomic resolution is an insulator in an antiferromagnetic ground state. NiO with its Néel temperature of 525 K and an almost perfectly bulk-terminated (001) surface [Fig. 64(a)] was found to be well suited for MExFM studies (Kaiser *et al.*, 2007). Upon sample cleavage atomic-resolution NC-AFM images can routinely be obtained on the (001) cleavage plane as shown in Fig. 64(b). Analysis of the observed atomic periodicity makes it clear that only one atomic species (either nickel or oxygen) is imaged as bright spots in NC-AFM experiments (Allers, Langkat, and Wiesendanger, 2001; Langkat *et al.*, 2003). Since AFM is primarily sensitive to the total valence-charge distribution, the atomic protrusions (bright sites) have to be assigned to the oxygen sublattice because the oxygen sites exhibit a larger valence charge density than the nickel sites [Fig. 64(c)]. No difference can be observed between magnetically inequivalent Ni sites in spin-averaged NC-AFM data [Fig. 64(b)].

The spin structure of the collinear antiferromagnet NiO can be described by ferromagnetic (111) sheets stacked in an antiferromagnetic order as shown in Fig. 64(a). Within each (111) sheet the spins of the nickel atoms point in the [211] direction. The spin orientation therefore alternates on neighboring rows along [110] directions on the (001) surface. According to the superexchange model, the magnetic exchange interaction between the localized Ni d states in NiO is mediated through the oxygen atoms. If a magnetic tip is brought close to a NiO(001) surface within a distance of 0.3–0.5 nm, either direct magnetic exchange between the tip apex atom and the surface Ni atoms or indirect superexchange interaction between the tip atom and subsurface Ni atoms via surface oxygen atoms can occur. In order to reveal the magnetic superstructure on the NiO(001) surface by MExFM the use of out-of-plane magnetized probe tips was found to be of crucial impor-

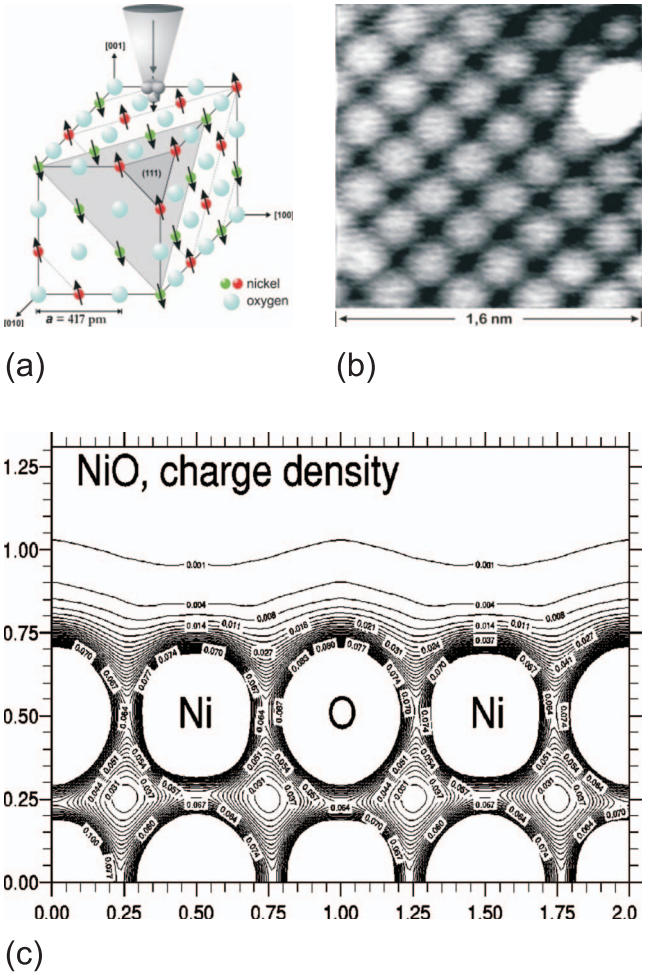

FIG. 64. (Color) Application of NC-AFM to NiO(001). (a) Crystal structure of NiO with a (001) surface plane. The lattice constant of NiO is $a=0.417$ nm. (b) Atomically resolved NC-AFM image of NiO(001) showing only one atomic species as bright spots. In addition, a single adsorbate is visible on the right-hand side of the image. From Allers, Langkat, and Wiesendanger, 2001. (c) Total valence charge density distribution for the NiO(001) surface indicating that the oxygen atoms should appear as protrusions (bright sites) in NC-AFM images whereas the Ni atoms should correspond to the dark sites. From Castell *et al.*, 1999.

tance (Kaiser *et al.*, 2007). Such MExFM probes were obtained by magnetizing Fe-coated Si tips in strong external magnetic fields of up to 5 T applied along the tip axis, i.e., perpendicularly to the sample surface plane [Fig. 65(a)]. These external fields do not influence the antiferromagnetic order of the NiO sample because the exchange coupling energy between the spins of the nickel atoms is much larger than the Zeeman energy related to the externally applied magnetic field. Figure 65(b) shows atomic-resolution MExFM data of the NiO(001) surface as obtained with an out-of-plane magnetized Fe-coated tip. Unit-cell averaging has been employed for this particular data set in order to improve the signal-to-noise ratio. It can be seen that every second row of apparent topographic depressions (nickel sites) appears darker than the row of nickel sites in between, leading to a superperiodicity as expected for an antiferromagnetically ordered state. The 2D Fourier transform of the raw data set, shown in Fig. 65(c), confirms the presence of a superstructure corresponding to the antiferromagnetic state of the NiO(001) surface because an additional pair of spots representing the size of the magnetic unit cell is visible in addition to the four brightest spots representing the atomic lattice structure of the NiO(001) plane.

Direct comparison of NC-AFM data on NiO(001) with pure chemical contrast and MExFM data with additional spin contrast is shown in Fig. 66. No contrast between magnetically inequivalent Ni sites is observed in the NC-AFM data of Fig. 66(a), as becomes evident on a closer inspection of a corresponding line section. The minima of the measured atomic-scale corrugation, corresponding to the nickel sites, appear exactly at the same height level. On the other hand, an apparent height difference of 4.5 pm between the nickel (dark) and oxygen (bright) sites can be deduced from the line section of the chemical-contrast NC-AFM image. The MExFM image shown in Fig. 66(b), however, exhibits a difference between magnetically inequivalent Ni sites: Ni atoms with opposite spin orientations now show up with an apparent height difference of 1.5 pm as revealed by the corresponding line section. This small apparent height difference between magnetically inequivalent

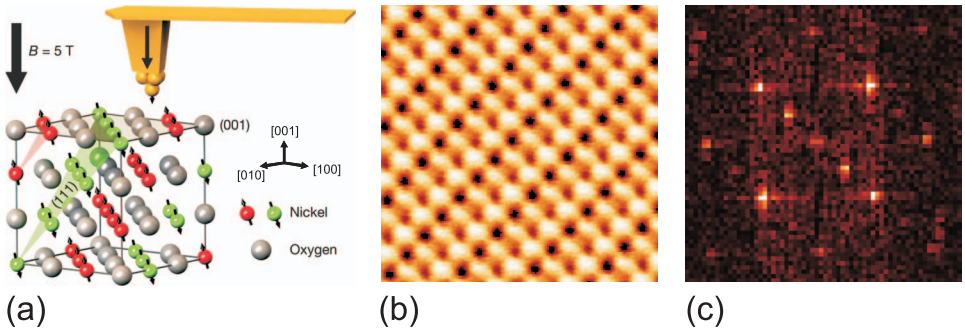

FIG. 65. (Color) Atomic-resolution spin mapping by MExFM. (a) Schematic of the spin structure of antiferromagnetic NiO(001) probed by a spin-sensitive MExFM tip. (b) Spin-resolved image of NiO(001) with atomic resolution as obtained by MExFM after unit-cell averaging. (c) Fourier transform of the raw MExFM data showing two spots which correspond to the magnetic superstructure period of the antiferromagnetic spin ordering at the NiO(001) surface. From Kaiser *et al.*, 2007.

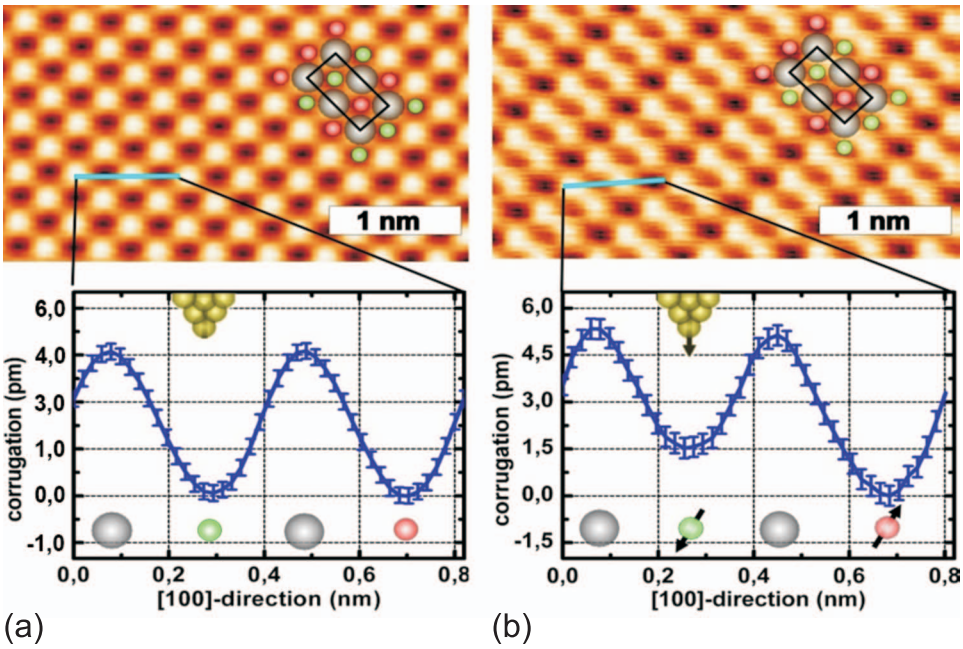

FIG. 66. (Color) Comparison of (a) an atomic-resolution image of NiO(001) as obtained by conventional NC-AFM exhibiting pure chemical contrast and (b) atomic-resolution MExFM data showing the additional superstructure due to the antiferromagnetic structure of NiO. The line section in (a) reveals an apparent height difference of 4.5 pm between nickel (dark) and oxygen (bright) sites, corresponding to a chemical contrast as explained in Fig. 64. In the MExFM image of (b) the oxygen atoms reveal the same contrast throughout the image while the nickel atoms with opposite spin orientations now show up with an apparent height difference of 1.5 pm. This small height difference in the MExFM data results from the magnetic exchange force interaction between the magnetic atom at the tip apex and the magnetic atoms on the sample surface depending on the relative spin alignment. Unit-cell averaging has been employed in order to improve the signal-to-noise ratio in the data sets.

nickel sites in the MExFM image of NiO(001) results from the direct exchange interaction between the magnetic Fe atom at the tip apex and the magnetic Ni atoms at the sample surface, which depends on the relative spin alignment according to Eq. (47). Experimentally it was found that the spin-dependent exchange and correlation forces on the antiferromagnetic NiO(001) surface can be detected only at very small tip-surface separations. This observation can be explained by the localized nature of the Ni *d* states in NiO as typical for an insulating sample system.

In order to resolve an apparent height difference of 1.5 pm only, as found between the magnetically inequivalent Ni sites on the NiO(001) surface, a very good signal-to-noise ratio is required. This usually implies the need for operating the MExFM instrument at low temperatures and in UHV, according to Eq. (51). Within the limits of detection sensitivity no contrast was found between the oxygen sites in the MExFM data shown in Fig. 66(b). Therefore, it can be concluded that the superexchange between the magnetic Fe tip atom and the subsurface Ni atoms via the surface oxygen atoms is much weaker than the direct exchange interaction between the tip atom and the surface Ni atoms, as expected.

An interesting question related to the dynamic mode of MExFM operation is whether the periodic approach of the oscillating magnetic tip to the sample surface within a distance of 0.3–0.5 nm can lead to some kind of spin excitation. Such spin excitation should be detectable in MExFM by analysis of the dissipation signal related to the damping of the cantilever oscillation. Figure 67 shows a comparison of MExFM data of the NiO(001) surface and the simultaneously recorded spatially resolved dissipation signal. Interestingly, the dissipation image [Fig. 67(b)] appears inverted with respect to the corresponding MExFM image [Fig. 67(a)], i.e., the highest dissipation signal is detected above the Ni sites. This behavior would indeed be expected if the energy dissipation is related to local spin excitations. A different value of the dissipated energy is observed above the magnetically inequivalent Ni sites. This can be explained by a dissipation mechanism based on spin excitation, which is sensitive to the relative orientation of the spins of tip and sample atoms. Surprisingly, a different value of the dissipated energy is also found above the oxygen sites which otherwise remain indistinguishable in the MExFM data of the NiO(001) surface. It may be speculated whether some energy dissipation might occur through superexchange interaction between the magnetic tip atom and subsurface Ni atoms via the surface oxygen sites.

2. Antiferromagnetic metals

While the prime motivation for the development of MExFM has been the extension of atomic-resolution spin mapping to insulating magnetic sample systems, the applicability of MExFM is not limited to insulators. Like

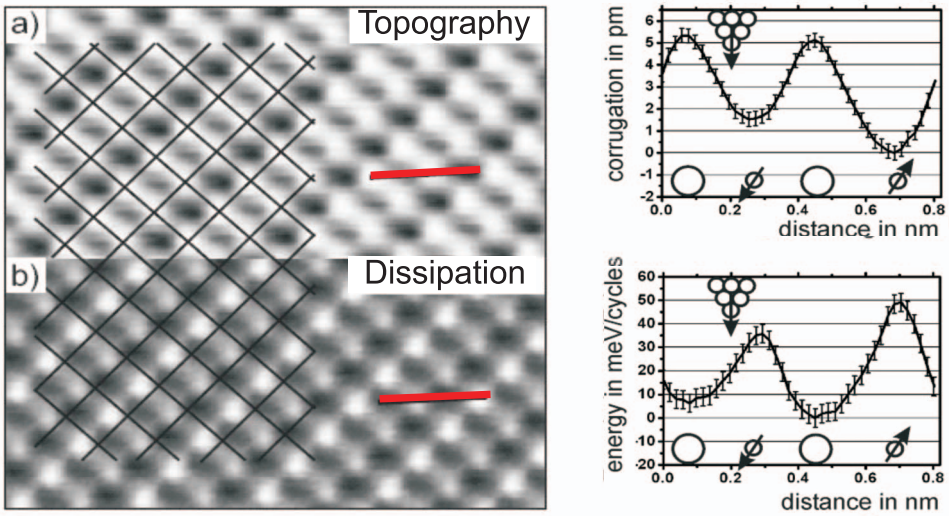

FIG. 67. (Color) Comparison of (a) atomic-resolution MExFM data on NiO(001) and (b) corresponding data set of the simultaneously recorded dissipation signal. The contrast in the dissipation data appears to be inverted compared to the MExFM image, i.e., the dissipation is highest above the Ni sites. Interestingly, the dissipation data also show contrast between different oxygen sites, which might be explained by the detection of superexchange interactions between the magnetic tip atom and subsurface Ni atoms via the surface oxygen atoms.

NC-AFM, the MExFM technique can be applied to metals and semiconductors as well. An example is given by the antiferromagnetic atomic layer of Fe on W(001) which was introduced in Sec. IV.D.1 (Schmidt *et al.*, 2009). The magnetic superstructure of that system corresponding to its antiferromagnetically ordered state at a measurement temperature of 8 K is well resolved in raw-data MExFM images [Fig. 68(a)]. The measured corrugation between Fe atoms in spin-up and spin-down states amounts to 5.3 pm, which is significantly larger than the apparent height difference between magnetically inequivalent Ni sites on the NiO(001) surface. It was found experimentally that the magnetic superstructure of the antiferromagnetic Fe monolayer on W(001) can be observed with tip-surface separations much larger than for MExFM measurements on the NiO(001) surface. This behavior can be explained by the fact that the *d* states of the metallic Fe monolayer extend farther into the vacuum region than the localized *d* states of Ni in the insulating NiO. As a consequence, the spin states can be probed up to larger tip-surface separations when MExFM is applied to a metallic system compared to an insulating sample.

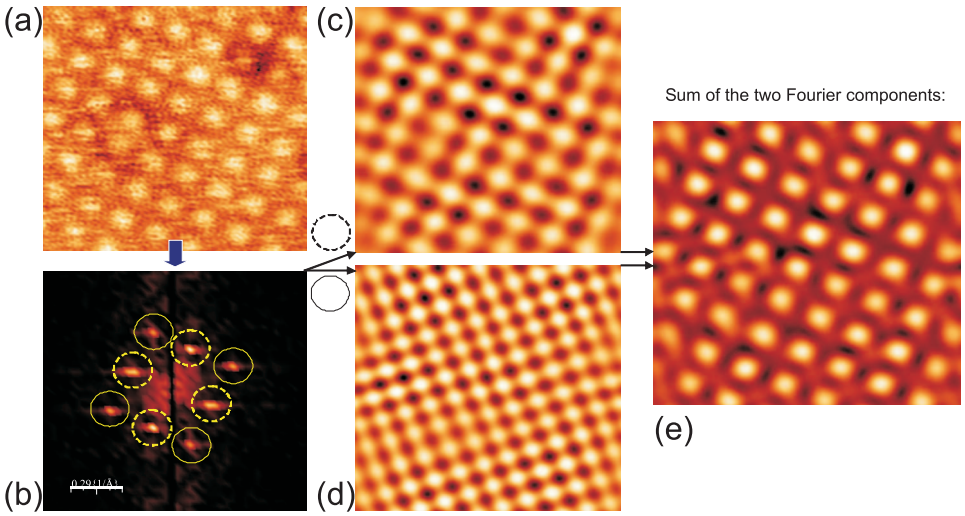

FIG. 68. (Color) Application of MExFM to magnetic metal surfaces. (a) Atomic-resolution MExFM data (3.2×3.2 nm^2) of an antiferromagnetic atomic layer of Fe grown on a W(001) substrate. (b) The Fourier transform of the MExFM data reveals two sets of spots corresponding to (c) the magnetic superlattice and (d) the atomic lattice periodicities. Therefore, both types of information are included in the raw data. (e) The MExFM image contrast is strongly dominated by the long-period magnetic superstructure compared to the short-period atomic lattice structure.

As shown in Fig. 68(b) the 2D Fourier transform of the MExFM image obtained on the antiferromagnetic Fe monolayer on W(001) contains two sets of spots, one corresponding to the magnetic superstructure [Fig. 68(c)] and the other to the atomic lattice structure [Fig. 68(d)]. This means that both types of information, magnetic order and atomic lattice periodicity, are contained in the MExFM data. However, the MExFM image appears to be dominated by the long-period magnetic superstructure [Fig. 68(e)], similar to the case of SPSTM images of the antiferromagnetic monolayers of Mn and Fe on W(110) and W(001), respectively (see Sec. IV.D.1).

C. Comparison of MExFM and SP-STM

The recent development of atomic-resolution MExFM, and in particular its application to metallic magnetic systems as discussed in the previous example, calls for a direct comparison between MExFM and SP-STM. At present, both techniques require UHV conditions. Both methods can be applied even in high external magnetic fields. While MExFM has so far successfully been demonstrated at low temperatures only, SP-STM has already been applied in a wide range of temperatures (from 300 mK up to 350 K).

Both experimental methods require the preparation of magnetic probe tips with a well-defined spin state of the tip apex atom. Moreover, both techniques rely on an overlap of spin-polarized electronic states of tip and sample surface atoms. Static spin structures as well as local spin excitations can be probed down to the atomic level by using either SP-STM or MExFM. While the combination of SP-STM with inelastic tunneling spectroscopy is required to probe local spin excitations by STM-based techniques, the same goal can in principle be achieved by a combination of MExFM with simultaneous measurements of the dissipation signal. SP-STM combined with SP-STS certainly has its strength in providing access to the spin- and energy-resolved local density of states, while MExFM is unique for its applicability to insulating sample systems.

VI. SUMMARY AND CONCLUSIONS

The experimental techniques of SP-STM and MExFM are providing new insight into spin structures and local spin excitations at length scales that are inaccessible by other magnetization-sensitive measurements. The combination of atomic resolution in direct space, single-spin sensitivity, and high energy resolution (in the case of SP-STS) offers unique possibilities for probing spin-dependent interactions in any kind of material system. Moreover, the combination of SP-STS with inelastic tunneling spectroscopy methods or the combination of MExFM with measurements of the energy dissipation opens up exciting opportunities for probing local spin excitations down to the atomic length scale.

While the instrumental developments and the optimization of probe tip preparation have required a significant amount of time and effort, SP-STM and MExFM have recently led to new discoveries such as complex nanoscale magnetic order in ultrathin films or unexpected magnetic properties of individual magnetic adatoms. Another recent exciting research direction is the combination of spin manipulation based on spin-current-induced switching and spin read out based on SP-STM methods. Ultimately, a new type of magnetic recording technology might be developed based on spin-state writing and read out rather than on magnetic stray fields. While the detection of magnetic stray fields becomes more and more difficult as the magnetic bit size is further reduced, the concept of spin manipulation and spin state determination was demonstrated down to the atomic level using SP-STM-based techniques. However, AFM-based methods are more widely used in industry than STM-based techniques; therefore it is expected that MExFM will finally have the greatest impact on the further development of magnetic devices. On the other hand, SP-STM and SP-STS are most useful for exploring the fundamentals of magnetic interactions at various energy scales and at the level of individual atoms and molecules.

ACKNOWLEDGMENTS

The author would like to thank all current and former co-workers and collaborators for their contributions to this work, in particular, W. Allers, L. Berbil-Bautista, S. Blügel, M. Bode, M. Dreyer, P. Ferriani, M. Getzlaff, S. Heinze, G. Herzog, U. Kaiser, S. Krause, A. Kubetzka, A. Lichtenstein, M. Liebmann, M. Löhndorf, F. Meier, M. Morgenstern, S. Pan, R. Pascal, O. Pietzsch, R. Ravlic, R. Schmidt, A. Schwarz, U. D. Schwarz, I. V. Shvets, E. Vedmedenko, K. von Bergmann, A. Wachowiak, A. Wadas, J. Wiebe, and L. Zhou. The author is indebted to R. Koltun, A. Smith, and W. Wulfhekel for providing figures for this article. Financial support from the Center of Excellence SFB 668 of the Deutsche Forschungsgemeinschaft and from the ERC Advanced Grant "FURORE" is gratefully acknowledged.

REFERENCES

Abelmann, L., A. van den Bos, and C. Lodder, 2005, *in Magnetic Microscopy of Nanostructures*, edited by H. Hopster, and H. P. Oepen (Springer, Berlin), Chap. 12, pp. 253–283.

Åkerman, J., 2005, "Toward a universal memory," Science **308**, 508–510.

Akiyama, R., H. Tanaka, T. Matsumoto, and T. Kawai, 2001, "Spin-polarized scanning tunneling microscopy on half-metallic manganite thin film with half-metallic manganite tip," Appl. Phys. Lett. **79**, 4378–4380.

Albonetti, C., I. Bergenti, M. Cavallini, V. Dediu, M. Massi, J.-F. Moulin, and F. Biscarini, 2002, "Electrochemical preparation of cobalt tips for scanning tunneling microscopy," Rev. Sci. Instrum. **73**, 4254–4256.

Albrecht, T. R., P. Grütter, D. Horne, and D. Rugar, 1991,

"Frequency modulation detection using high-Q cantilevers for enhanced force microscope sensitivity," J. Appl. Phys. **69**, 668–673.

Allers, W., S. Langkat, and R. Wiesendanger, 2001, "Low-temperature dynamic force microscopy on nickel oxide (2001)," Appl. Phys. A: Mater. Sci. Process. **72**, S27–S30.

Allers, W., A. Schwarz, U. D. Schwarz, and R. Wiesendanger, 1998, "A scanning force microscope with atomic resolution in ultrahigh vacuum and at low temperatures," Rev. Sci. Instrum. **69**, 221–225.

Alvarado, S. F., 1995, "Tunneling potential barrier dependence of electron spin polarization," Phys. Rev. Lett. **75**, 513–516.

Alvarado, S. F., and P. Renaud, 1992, "Observation of spin-polarized electron tunneling from a ferromagnet into GaAs," Phys. Rev. Lett. **68**, 1387–1390.

Anisimovas, E., and P. Johansson, 1999, "Tip-geometry effects in circularly polarized light emission from a scanning tunneling microscope," Phys. Rev. B **59**, 5126–5133.

Ashino, M., A. Schwarz, T. Behnke, and R. Wiesendanger, 2004, "Atomic-resolution dynamic force microscopy and spectroscopy of a single-walled carbon nanotube: characterization of interatomic van der Waals forces," Phys. Rev. Lett. **93**, 136101.

Balashov, T., A. F. Takács, W. Wulfhekel, and J. Kirschner, 2006, "Magnon excitation with spin-polarized scanning tunneling microscopy," Phys. Rev. Lett. **97**, 187201.

Bardeen, J., 1961, "Tunneling from a many body point of view," Phys. Rev. Lett. **6**, 57–59.

Berbil-Bautista, L., S. Krause, M. Bode, and R. Wiesendanger, 2007, "Spin-polarized scanning tunneling microscopy and spectroscopy of ferromagnetic Dy(0001)/W(110) films," Phys. Rev. B **76**, 064411.

Berbil-Bautista, L., S. Krause, T. Hänke, M. Bode, and R. Wiesendanger, 2006, "Spin-polarized scanning tunneling microscopy through an adsorbate layer: Sulfur-covered Fe/W(110)," Surf. Sci. **600**, L20–L24.

Berdunov, N., S. Murphy, G. Mariotto, and I. V. Shvets, 2004, "Atomically resolved spin-dependent tunneling on the oxygen-terminated Fe_3O_4(111)," Phys. Rev. Lett. **93**, 057201.

Berdunov, N., S. Murphy, G. Mariotto, I. V. Shvets, and Y. M. Mykovskiy, 2004, "Spin-polarized tunneling effects observed on the oxygen-terminated Fe_3O_4(111) surface," J. Appl. Phys. **95**, 6891–6893.

Berger, L., 1996, "Emission of spin waves by a magnetic multilayer traversed by a current," Phys. Rev. B **54**, 9353–9358.

Binnig, G., C. F. Quate, and C. Gerber, 1986, "Atomic force microscope," Phys. Rev. Lett. **56**, 930–933.

Binnig, G., and H. Rohrer, 1987, "Scanning tunneling microscopy—from birth to adolescence," Rev. Mod. Phys. **59**, 615–625.

Binnig, G., H. Rohrer, C. Gerber, and E. Weibel, 1982a, "Tunneling through a contollable vacuum gap," Appl. Phys. Lett. **40**, 178–180.

Binnig, G., H. Rohrer, C. Gerber, and E. Weibel, 1982b, "Surface studies by scanning tunnelling microscopy," Phys. Rev. Lett. **49**, 57–61.

Binnig, G., H. Rohrer, C. Gerber, and E. Weibel, 1983, "7 $\times$7 reconstruction on Si(111) resolved in real space," Phys. Rev. Lett. **50**, 120–123.

Blügel, S., D. Pescia, and P. H. Dederichs, 1989, "Ferromagnetism versus antiferromagnetism of the Cr(001) surface," Phys. Rev. B **39**, 1392–1394.

Bode, M., 2003, "Spin-polarized scanning tunneling microscopy," Rep. Prog. Phys. **66**, 523–581.

Bode, M., M. Getzlaff, S. Heinze, R. Pascal, and R. Wiesendanger, 1998, "Magnetic exchange splitting of the Gd(0001) surface state studied by variable-temperature scanning tunneling spectroscopy," Appl. Phys. A: Mater. Sci. Process. **66**, S121–S124.

Bode, M., M. Getzlaff, A. Kubetzka, R. Pascal, O. Pietzsch, and R. Wiesendanger, 1999, "Temperature-dependent exchange splitting of a surface state on a local-moment magnet: Tb(0001)," Phys. Rev. Lett. **83**, 3017–3020.

Bode, M., M. Getzlaff, and R. Wiesendanger, 1998, "Spin-polarized vacuum tunneling into the exchange-split surface state of Gd(0001)," Phys. Rev. Lett. **81**, 4256–4259.

Bode, M., M. Getzlaff, and R. Wiesendanger, 1999, "Quantitative aspects of spin-polarized scanning tunneling spectroscopy of Gd(0001)," J. Vac. Sci. Technol. A **17**, 2228–2232.

Bode, M., S. Heinze, A. Kubetzka, O. Pietzsch, M. Hennefarth, M. Getzlaff, R. Wiesendanger, X. Nie, G. Bihlmayer, and S. Blügel, 2002, "Structural, electronic, and magnetic properties of a Mn monolayer on W(110)," Phys. Rev. B **66**, 014425.

Bode, M., S. Heinze, A. Kubetzka, O. Pietzsch, X. Nie, G. Bihlmayer, S. Blügel, and R. Wiesendanger, 2002, "Magnetization-direction-dependent local electronic structure probed by scanning tunneling spectroscopy," Phys. Rev. Lett. **89**, 237205.

Bode, M., M. Heide, K. von Bergmann, P. Ferriani, S. Heinze, G. Bihlmayer, A. Kubetzka, O. Pietzsch, S. Blügel, and R. Wiesendanger, 2007, "Chiral magnetic order at surfaces driven by inversion asymmetry," Nature (London) **447**, 190–193.

Bode, M., A. Kubetzka, S. Heinze, O. Pietzsch, R. Wiesendanger, M. Heide, X. Nie, G. Bihlmayer, and S. Blügel, 2003, "Spin-orbit induced local band structure variations revealed by scanning tunnelling spectroscopy," J. Exp. Zool. **15**, S679–S692.

Bode, M., A. Kubetzka, O. Pietzsch, and R. Wiesendanger, 2001, "Spin-polarized scanning tunneling spectroscopy on Fe nanowires," Appl. Phys. A: Mater. Sci. Process. **72**, S149–S153.

Bode, M., A. Kubetzka, O. Pietzsch, and R. Wiesendanger, 2002, "Spin-resolved spectro-microscopy of magnetic nanowire arrays," Surf. Sci. **514**, 135–144.

Bode, M., A. Kubetzka, O. Pietzsch, and R. Wiesendanger, 2005, in *Modern Techniques for Characterizing Magnetic Materials*, edited by Y. Zhu (Kluwer Academic, Dordrecht), p. 383.

Bode, M., A. Kubetzka, K. von Bergmann, O. Pietzsch, and R. Wiesendanger, 2005, "Imaging the switching behavior of superparamagnetic nanoislands by spin-polarized scanning tunneling microscopy," Microsc. Res. Tech. **66**, 117–125.

Bode, M., R. Pascal, and R. Wiesendanger, 1997, "Scanning tunneling spectroscopy of Fe/W(110) using iron covered probe tips," J. Vac. Sci. Technol. A **15**, 1285–1290.

Bode, M., O. Pietzsch, A. Kubetzka, S. Heinze, and R. Wiesendanger, 2001, "Experimental evidence for intra-atomic non-collinear magnetism at thin film probe tips," Phys. Rev. Lett. **86**, 2142–2145.

Bode, M., O. Pietzsch, A. Kubetzka, and R. Wiesendanger, 2004, "Shape-dependent thermal switching behavior of superparamagnetic nanoislands," Phys. Rev. Lett. **92**, 067201.

Bode, M., R. Ravlic, M. Kleiber, and R. Wiesendanger, 2005,

"Growth and magnetism of Fe on Cr(001): a spin-polarized scanning tunneling spectroscopy and magnetic force microscopy study," Appl. Phys. A: Mater. Sci. Process. **80**, 907–912.
Bode, M., E. Y. Vedmedenko, K. von Bergmann, A. Kubetzka, P. Ferriani, S. Heinze, and R. Wiesendanger, 2006, "Atomic spin structure of antiferromagnetic domain walls," Nature Mater. **5**, 477–481.
Bode, M., K. von Bergmann, O. Pietzsch, A. Kubetzka, and R. Wiesendanger, 2006, "Spin-polarized scanning tunneling spectroscopy of dislocation lines in Fe films on W(110)," J. Magn. Magn. Mater. **304**, 1–5.
Bode, M., A. Wachowiak, J. Wiebe, A. Kubetzka, M. Morgenstern, and R. Wiesendanger, 2004, "Thickness dependent magnetization states of Fe islands on W(110): From single domain to vortex and diamond patterns," Appl. Phys. Lett. **84**, 948–950.
Bode, M., and R. Wiesendanger, 2005, in *Magnetic Microscopy of Nanostructures*, edited by H. Hopster and H. P. Oepen (Springer, Berlin), Chap. 10, pp. 203–223.
Bodea, S., W. Wulfhekel, and J. Kirschner, 2005, "Influence of step edges and strain on the domain wall width," Phys. Rev. B **72**, 100403.
Braun, H.-B., 1993, "Thermally activated magnetization reversal in elongated ferromagnetic particles," Phys. Rev. Lett. **71**, 3557–3560.
Braun, H.-B., 1994, "Statistical mechanics of nonuniform magnetization reversal," Phys. Rev. B **50**, 16501–16521.
Brown, W. F., 1963, "Thermal fluctuations of a single-domain particle," Phys. Rev. **130**, 1677–1686.
Bruno, P., 1999, "Geometrically constrained magnetic wall," Phys. Rev. Lett. **83**, 2425–2428.
Bruno, P., and C. Chappert, 1992, "Ruderman-Kittel theory of oscillatory interlayer exchange coupling," Phys. Rev. B **46**, 261–270.
Bryl, R., and M. S. Altman, 2003, "Spin-polarized vacuum tunneling in field emission from Co-coated W(111) tips," J. Appl. Phys. **94**, 4670–4675.
Castell, M. R., S. L. Dudarev, G. A. D. Briggs, and A. P. Sutton, 1999, "Unexpected differences in the surface electronic structure of NiO and CoO observed by STM and explained by first-principles theory," Phys. Rev. B **59**, 7342–7345.
Cavallini, M., and F. Biscarini, 2000, "Electrochemically etched nickel tips for spin polarized scanning tunneling microscopy," Rev. Sci. Instrum. **71**, 4457–4460.
Ceballos, S. F., G. Mariotto, S. Murphy, and I. V. Shvets, 2003, "Fabrication of magnetic STM probes and their application to studies of the Fe_3O_4(001) surface," Surf. Sci. **523**, 131–140.
Chen, C. J., 1990a, "Tunneling matrix-elements in three-dimensional space: The derivative rule and the sum rule," Phys. Rev. B **42**, 8841–8857.
Chen, C. J., 1990b, "Origin of atomic resolution on metal-surfaces in scanning tunneling microscopy," Phys. Rev. Lett. **65**, 448–451.
Chen, C. J., 1991, "Microscopic view of scanning tunneling microscopy," J. Vac. Sci. Technol. A **9**, 44–50.
Coey, J. M. D., I. V. Shvets, R. Wiesendanger, and H.-J. Güntherodt, 1993, "Charge freezing and surface anisotropy on magnetite (100)," J. Appl. Phys. **73**, 6742–6744.
de Groot, R. A., 1991, "Half-metallic magnetism in the 1990s," Physica B **172**, 45–50.
de Groot, R. A., F. M. Müller, P. G. van Engen, and K. H. J. Buschow, 1983, "New class of materials: Half-metallic ferromagnets," Phys. Rev. Lett. **50**, 2024–2027.
Diekhöner, L., M. A. Schneider, A. N. Baranov, V. S. Stepanyuk, P. Bruno, and K. Kern, 2003, "Surface states of cobalt nanoislands on Cu(111)," Phys. Rev. Lett. **90**, 236801.
Ding, H. F., W. Wulfhekel, P. Bruno, and J. Kirschner, 2003, "Absence of zero-bias anomaly in spin-polarized vacuum tunneling in Co(0001)," Phys. Rev. Lett. **90**, 116603.
Ding, H. F., W. Wulfhekel, and J. Kirschner, 2002, "Ultra-sharp domain walls in the closure domain pattern of Co(0001)," Europhys. Lett. **57**, 100–106.
Ding, H. F., W. Wulfhekel, U. Schlickum, and J. Kirschner, 2003, "Spin-polarized vacuum tunneling at small gap widths," Europhys. Lett. **63**, 419–425.
Donath, M., B. Gubanka, and F. Passek, 1996, "Temperature-dependent spin polarization of magnetic surface state at Gd(0001)," Phys. Rev. Lett. **77**, 5138–5141.
Dreyer, M., M. Löhndorf, A. Wadas, and R. Wiesendanger, 1998, "Ultrahigh vacuum magnetic force microscopy of the domain structure of ultrathin Co films," Appl. Phys. A: Mater. Sci. Process. **66**, 1209–1212.
Dzyaloshinskii, I. E., 1957, "Thermodynamic theory of 'weak' ferromagnetism in antiferromagnetic substances," Sov. Phys. JETP **5**, 1259–1262.
Elmers, H. J., 1998, "Magnetization states in ultrathin films with laterally modulated anisotropies," J. Magn. Magn. Mater. **185**, 274–282.
Elmers, H. J., J. Hauschild, and U. Gradmann, 1999, "Onset of perpendicular magnetization in nanostripe arrays of Fe on stepped W(110) surfaces," Phys. Rev. B **59**, 3688–3695.
Esaki, L., 1974, "Long journey into tunneling," Rev. Mod. Phys. **46**, 237–244.
Feldtkeller, E., and H. Thomas, 1965, "Struktur und Energie von Blochlinien in dünnen ferromagnetischen Schichten," Phys. Kondens. Mater. **4**, 8–14.
Ferriani, P., K. von Bergmann, E. Y. Vedmedenko, S. Heinze, M. Bode, M. Heide, G. Bihlmayer, S. Blügel, and R. Wiesendanger, 2008, "Atomic-scale non-collinear magnetic order in thin films induced by spin-orbit coupling," Phys. Rev. Lett. **101**, 027201.
Fischer, B., and M. W. Klein, 1975, "Magnetic and nonmagnetic impurities in two-dimensional metals," Phys. Rev. B **11**, 2025–2029.
Fu, C. L., and A. J. Freeman, 1986, "Surface ferromagnetism of Cr(001)," Phys. Rev. B **33**, 1755–1761.
Gambardella, P., R. Rusponi, M. Veronese, S. S. Dhesi, C. Grazioli, A. Dallmeyer, I. Cabria, R. Zeller, P. H. Dederichs, K. Kern, C. Carbone, and H. Brune, 2003, "Giant magnetic anisotropy of single cobalt atoms and nanoparticles," Science **300**, 1130–1133.
Gao, C. L., U. Schlickum, W. Wulfhekel, and J. Kirschner, 2007, "Mapping the surface spin structure of large unit cells: reconstructed Mn films on Fe(001)," Phys. Rev. Lett. **98**, 107203.
Getzlaff, M., M. Bode, S. Heinze, R. Pascal, and R. Wiesendanger, 1998, "Temperature-dependent exchange-splitting of the magnetic Gd(0001) surface state," J. Magn. Magn. Mater. **184**, 155–165.
Getzlaff, M., M. Bode, and R. Wiesendanger, 1999, "Spin-polarized vacuum tunneling: correlation of electronic and magnetic properties on the nanometer scale," Surf. Rev. Lett. **6**, 591–597.
Giaever, I., 1974, "Electron tunneling and superconductivity," Rev. Mod. Phys. **46**, 245–250.
Giessibl, F. J., 1995, "Atomic-resolution of the silicon (111)-

(7X7) surface by atomic force microscopy," Science **267**, 68–71.
Giessibl, F. J., 2003, "Advances in atomic force microscopy," Rev. Mod. Phys. **75**, 949–983.
Hänke, T., M. Bode, S. Krause, L. Berbil-Bautista, and R. Wiesendanger, 2005, "Temperature-dependent scanning tunneling spectroscopy of Cr(001): orbital Kondo resonance versus surface state," Phys. Rev. B **72**, 085453.
Hänke, T., S. Krause, L. Berbil-Bautista, M. Bode, R. Wiesendanger, D. Lott, and A. Schreyer, 2005, "Absence of spin-flip transition at the Cr(001) surface: A combined spin-polarized scanning tunneling microscopy and neutron scattering study," Phys. Rev. B **71**, 184407.
Hartmann, U., 1999, "Magnetic force microscopy," Annu. Rev. Mater. Sci. **29**, 53–87.
Heinrich, A. J., J. A. Gupta, C. P. Lutz, and D. M. Eigler, 2004, "Single-atom spin-flip spectroscopy," Science **306**, 466–469.
Heinze, S., 2006, "Simulation of spin-polarized scanning tunneling microscopy images of nanoscale non-collinear magnetic structures," Appl. Phys. A: Mater. Sci. Process. **85**, 407–414.
Heinze, S., M. Bode, A. Kubetzka, O. Pietzsch, X. Nie, S. Blügel, and R. Wiesendanger, 2000, "Real-space imaging of two-dimensional antiferromagnetism on the atomic scale," Science **288**, 1805–1808.
Heinze, S., P. Kurz, D. Wortmann, G. Bihlmayer, and S. Blügel, 2002, "Complex magnetism in ultra-thin films: atomic-scale spin structures and resolution by the spin-polarized scanning tunneling microscope," Appl. Phys. A: Mater. Sci. Process. **75**, 25–36.
Hertel, R., 2002, "Thickness dependence of the magnetization structures of thin permalloy rectangles," Z. Metallkd. **93**, 957–962.
Hilzinger, H. R., and H. Kronmüller, 1972, "Spin configuration and intrinsic coercive field of narrow domain walls in Co_5R compounds," Phys. Status Solidi B **54**, 593–604.
Hirjibehedin, C. F., C.-Y. Lin, A. F. Otte, M. Ternes, C. P. Lutz, B. A. Jones, and A. J. Heinrich, 2007, "Large magnetic anisotropy of a single atomic spin embedded in a surface molecular network," Science **317**, 1199–1203.
Hirjibehedin, C. F., C. P. Lutz, and A. J. Heinrich, 2006, "Spin coupling in engineered atomic structures," Science **312**, 1021–1024.
Hubert, A., and R. Schäfer, 1998, *Magnetic Domains* (Springer, Berlin).
Johnson, M., and J. Clarke, 1990, "Spin-polarized scanning tunneling microscope: concept, design, and preliminary results from a prototype operated in air," J. Appl. Phys. **67**, 6141–6152.
Jordan, K., G. Mariotto, S. F. Ceballos, S. Murphy, and I. V. Shvets, 2005, "Spin polarized STM imaging of the $Fe_3O_4(001)$ surface using anti-ferromagnetic tips," J. Magn. Magn. Mater. **290-291**, 1029–1032.
Josephson, B. D., 1974, "Discovery of tunnelling supercurrents," Rev. Mod. Phys. **46**, 251–254.
Jullière, M., 1975, "Tunneling between ferromagnetic-films," Phys. Lett. A **54**, 225–226.
Kaiser, U., A. Schwarz, and R. Wiesendanger, 2007, "Magnetic exchange force microscopy with atomic resolution," Nature (London) **446**, 522–525.
Kawagoe, T., Y. Iguchi, A. Yamasaki, Y. Suzuki, K. Koike, and S. Suga, 2005, "Surface magnetic structure of epitaxial Cr(001) films on Au(001) studied by spin-polarized scanning tunneling spectroscopy," Phys. Rev. B **71**, 014427.
Kawagoe, T., Y. Suzuki, M. Bode, and K. Koike, 2003, "Evidence of a topological antiferromagnetic order on ultrathin Cr(001) film surface studied by spin-polarized scanning tunneling spectroscopy," J. Appl. Phys. **93**, 6575–6577.
Klebanoff, L. E., S. W. Robey, G. Liu, and D. A. Shirley, 1984, "Observation of a surface magnetic phase transition on Cr(100)," Phys. Rev. B **30**, 1048–1051.
Kleiber, M., M. Bode, R. Ravlic, N. Tezuka, and R. Wiesendanger, 2002, "Magnetic properties of the Cr(001) surface studied by spin-polarized scanning tunnelling spectroscopy," J. Magn. Magn. Mater. **240**, 64–69.
Kleiber, M., M. Bode, R. Ravlic, and R. Wiesendanger, 2000, "Topology-induced spin frustrations at the Cr(001) surface studied by spin-polarized scanning tunneling spectroscopy," Phys. Rev. Lett. **85**, 4606–4609.
Knorr, N., M. A. Schneider, L. Diekhöner, P. Wahl, and K. Kern, 2002, "Kondo effect of single Co adatoms on Cu surfaces," Phys. Rev. Lett. **88**, 096804.
Koltun, R., M. Herrmann, G. Güntherodt, and V. A. M. Brabers, 2001, "Enhanced atomic-scale contrast on $Fe_3O_4(100)$ observed with an Fe STM tip," Appl. Phys. A: Mater. Sci. Process. **73**, 49–53.
Krause, S., L. Berbil-Bautista, T. Hänke, F. Vonau, M. Bode, and R. Wiesendanger, 2006, "Consequences of line defects on the magnetic structure of high anisotropy films: Pinning centers on Dy/W(110)," Europhys. Lett. **76**, 637–643.
Krause, S., L. Berbil-Bautista, G. Herzog, M. Bode, and R. Wiesendanger, 2007, "Current-induced magnetization switching with a spin-polarized scanning tunneling microscope," Science **317**, 1537–1540.
Krause, S., G. Herzog, T. Stapelfeldt, L. Berbil-Bautista, M. Bode, E. Y. Vedmedenko, and R. Wiesendanger, 2009, "Magnetization reversal of nanoscale islands: How size and shape affect the Arrhenius prefactor," Phys. Rev. Lett. **103**, 127202.
Kubetzka, A., M. Bode, O. Pietzsch, and R. Wiesendanger, 2002, "Spin-polarized scanning tunneling microscopy with antiferromagnetic probe tips," Phys. Rev. Lett. **88**, 057201.
Kubetzka, A., M. Bode, and R. Wiesendanger, 2007, "Spin-polarized STM in field emission mode," Appl. Phys. Lett. **91**, 012508.
Kubetzka A., P. Ferriani, M. Bode, S. Heinze, G. Bihlmayer, K. von Bergmann, O. Pietzsch, S. Blügel, and R. Wiesendanger, 2005, "Revealing antiferromagnetic order of the Fe monolayer on W(001): Spin-polarized scanning tunneling microscopy and first-principles calculations," Phys. Rev. Lett. **94**, 087204.
Kubetzka, A., O. Pietzsch, M. Bode, R. Ravlic, and R. Wiesendanger, 2003, "Spin-polarized STM investigation of magnetic domain walls," Acta Phys. Pol. A **104**, 259–268.
Kubetzka, A., O. Pietzsch, M. Bode, and R. Wiesendanger, 2001, "Magnetism of nanoscale Fe islands studied by spin-polarized scanning tunneling spectroscopy," Phys. Rev. B **63**, 140407.
Kubetzka, A., O. Pietzsch, M. Bode, and R. Wiesendanger, 2003a, "Determining the spin polarization of surfaces by spin-polarized scanning tunneling spectroscopy," Appl. Phys. A: Mater. Sci. Process. **76**, 873–877.
Kubetzka, A., O. Pietzsch, M. Bode, and R. Wiesendanger, 2003b, "Spin-polarized scanning tunneling microscopy study of 360 degrees walls in an external magnetic field," Phys. Rev. B **67**, 020401.
LaBella, V. P., D. W. Bullock, Z. Ding, C. Emery, A. Venkate-

san, W. F. Oliver, G. J. Salamo, P. M. Thibado, and M. Mortazavi, 2001, "Spatially resolved spin-injection probability for gallium arsenide," Science **292**, 1518–1521.

Laiho, R., and H. J. Reittu, 1993, "Theory of scanning tunneling microscopy with spin-polarized electrons obtained from a semiconductor tip," Surf. Sci. **289**, 363–369.

Laiho, R., and H. J. Reittu, 1996, "Spin-polarized scanning probe microscopy," Phys. Solid State **38**, 506–512.

Laiho, R., and H. J. Reittu, 1997, "Spin-polarized scanning tunneling microscopy with detection of polarized luminescence emerging from a semiconductor tip," J. Phys.: Condens. Matter **9**, 5697–5707.

Langkat, S. M., H. Hölscher, A. Schwarz, and R. Wiesendanger, 2003, "Determination of site specific interatomic forces between an iron coated tip and the NiO(001) surface by force field spectroscopy," Surf. Sci. **527**, 12–20.

Li, J., W.-D. Schneider, R. Berndt, and S. Crampin, 1998, "Electron confinement to nanoscale Ag islands on Ag(111): a quantitative study," Phys. Rev. Lett. **80**, 3332–3335.

Liebmann, M., A. Schwarz, S. M. Langkat, and R. Wiesendanger, 2002, "A low-temperature ultrahigh vacuum scanning force microscope with a split-coil magnet," Rev. Sci. Instrum. **73**, 3508–3514.

Madhavan, V., W. Chen, T. Jamneala, M. F. Crommie, and N. S. Wingreen, 1998, "Tunneling into a single magnetic atom: spectroscopic evidence of the Kondo resonance," Science **280**, 567–569.

Maekawa, S., and U. Gäfvert, 1982, "Electron tunneling between ferromagnetic films," IEEE Trans. Magn. **18**, 707–708.

Mariotto, G., S. Murphy, and I. V. Shvets, 2002, "Charge ordering on the surface of Fe_3O_4(001)," Phys. Rev. B **66**, 245426.

Martin, Y., and K. Wickramasinghe, 1987, "Magnetic imaging by force microscopy with 1000-Å resolution," Appl. Phys. Lett. **50**, 1455–1457.

Meckler, S., M. Gyamfi, O. Pietzsch, and R. Wiesendanger, 2009, "A low-temperature spin-polarized scanning tunneling microscope operating in a fully rotatable magnetic field," Rev. Sci. Instrum. **80**, 023708.

Meckler, S., N. Mikuszeit, A. Pressler, E. Vedmedenko, O. Pietzsch, and R. Wiesendanger, 2009, "Real-space observation of a right-handed inhomogeneous cycloidal spin spiral by spin-polarized scanning tunneling microscopy in a triple axes vector magnet," Phys. Rev. Lett. **103**, 157201.

Meier, F., K. von Bergmann, P. Ferriani, J. Wiebe, M. Bode, K. Hashimoto, S. Heinze, and R. Wiesendanger, 2006, "Spin-dependent electronic and magnetic properties of Co nanostructures on Pt(111) studied by spin-resolved scanning tunneling spectroscopy," Phys. Rev. B **74**, 195411.

Meier, F., K. von Bergmann, J. Wiebe, M. Bode, and R. Wiesendanger, 2007, "Co double-layer nanostructures on Pt(111) studied by spin-polarized scanning tunneling microscopy," J. Phys. D: Appl. Phys. **40**, 1306–1311.

Meier, F., L. Zhou, J. Wiebe, and R. Wiesendanger, 2008, "The magnetization of individual adatoms," Science **320**, 82–86.

Meservey, R., P. M. Tedrow, and P. Fulde, 1970, "Magnetic field splitting of quasiparticle states in superconducting aluminum films," Phys. Rev. Lett. **25**, 1270–1272.

Minakov, A. A., and I. V. Shvets, 1990, "On the possibility of resolving quantization axes of surface spins by means of a scanning tunneling microscope with a magnetic tip," Surf. Sci. **236**, L377–L381.

Morita, S., R. Wiesendanger, and E. Meyer, 2002, Eds., *Non-contact Atomic Force Microscopy* (Springer, Berlin).

Moriya, T., 1960, "Anisotropic superexchange interaction and weak ferromagnetism," Phys. Rev. **120**, 91–98.

Murphy, S., S. F. Ceballos, G. Mariotto, N. Berdunov, K. Jordan, I. V. Shvets, and Y. M. Mukovskii, 2005, "Atomic scale spin-dependent STM on magnetite using antiferromagnetic STM tips," Microsc. Res. Tech. **66**, 85–92.

Murphy, S., J. Osing, and I. V. Shvets, 1999, "Fabrication of submicron-scale manganese-nickel tips for spin-polarized STM studies," Appl. Surf. Sci. **144-145**, 497–500.

Myers, E. B., D. C. Ralph, J. A. Katine, R. N. Louie, and R. A. Buhrmann, 1999, "Current-induced switching of domains in magnetic multilayer devices," Science **285**, 867–870.

Nabhan, W., Y. Suzuki, R. Shinohara, K. Yamaguchi, and E. Tamura, 1999, "Effect of dichroism in the GaAs-tip-based spin-polarized STM," Appl. Surf. Sci. **144-145**, 570–574.

Nussinov, Z., M. F. Crommie, and A. V. Balatsky, 2003, "Noise spectroscopy of a single spin with spin-polarized STM," Phys. Rev. B **68**, 085402.

Okuno, S. N., T. Kishi, and K. Tanaka, 2002, "Spin-polarized tunneling spectroscopy of Co(0001) surface states," Phys. Rev. Lett. **88**, 066803.

Pascal, R., C. Zarnitz, M. Bode, and R. Wiesendanger, 1997, "Fabrication of atomic gratings based on self-organization of adsorbates with repulsive interaction," Appl. Phys. A: Mater. Sci. Process. **65**, 81–83.

Pierce, D. T., 1988, "Spin-polarized electron microscopy," Phys. Scr. **38**, 291–296.

Pietzsch, O., A. Kubetzka, M. Bode, and R. Wiesendanger, 2000a, "Real-space observation of dipolar antiferromagnetism in magnetic nanowires by spin-polarized scanning tunneling spectroscopy," Phys. Rev. Lett. **84**, 5212–5215.

Pietzsch, O., A. Kubetzka, M. Bode, and R. Wiesendanger, 2000b, "A low-temperature UHV scanning tunneling microscope with a split-coil magnet system and a rotary motion stepper motor for high spatial resolution studies of surface magnetism," Rev. Sci. Instrum. **71**, 424–430.

Pietzsch, O., A. Kubetzka, M. Bode, and R. Wiesendanger, 2001, "Observation of magnetic hysteresis at the nanometer scale by spin-polarized scanning tunnelling spectroscopy," Science **292**, 2053–2056.

Pietzsch, O., A. Kubetzka, M. Bode, and R. Wiesendanger, 2004a, "Spin-polarized scanning tunneling spectroscopy of nanoscale cobalt islands on Cu(111)," Phys. Rev. Lett. **92**, 057202.

Pietzsch, O., A. Kubetzka, M. Bode, and R. Wiesendanger, 2004b, "Recent advances in spin-polarized scanning tunneling microscopy," Appl. Phys. A: Mater. Sci. Process. **78**, 781–785.

Pietzsch, O., S. Okatov, A. Kubetzka, M. Bode, S. Heinze, A. Lichtenstein, and R. Wiesendanger, 2006, "Spin-resolved electronic structure of nanoscale cobalt islands on Cu(111)," Phys. Rev. Lett. **96**, 237203.

Pratzer, M., H. J. Elmers, M. Bode, O. Pietzsch, A. Kubetzka, and R. Wiesendanger, 2001, "Atomic-scale magnetic domain walls in quasi-one-dimensional Fe nanostripes," Phys. Rev. Lett. **87**, 127201.

Prokop, J., A. Kukunin, and H. J. Elmers, 2005, "Magnetic anisotropies and coupling mechanisms in Fe/Mo(110) nanostripes," Phys. Rev. Lett. **95**, 187202.

Prokop, J., A. Kukunin, and H. J. Elmers, 2006, "Spin-polarized scanning tunneling microscopy and spectroscopy of ultrathin Fe/Mo(110) films using W/Au/Co tips," Phys. Rev. B **73**, 014428.

Prokop, J., A. Kukunin, and H. J. Elmers, 2007, "Spin-polarized tunneling spectroscopy and magnetic coupling in Au-coated Fe/Mo(110) nanostructures," Phys. Rev. B **75**, 144423.

Ravlic, R., M. Bode, A. Kubetzka, and R. Wiesendanger, 2003, "Correlation of dislocation and domain structure of Cr(001) investigated by spin-polarized scanning tunneling microscopy," Phys. Rev. B **67**, 174411.

Ravlic, R., M. Bode, and R. Wiesendanger, 2003, "Correlation of structural, local electronic and magnetic properties of Fe on Cr(001) studied by spin-polarized scanning tunneling spectroscopy," J. Phys.: Condens. Matter **15**, S2513–S2531.

Rusponi, S., N. Weiss, T. Cren, M. Epple, and H. Brune, 2005, "High tunnel magnetoresistance in spin-polarized scanning tunneling microscopy of Co nanoparticles on Pt(111)," Appl. Phys. Lett. **87**, 162514.

Sáenz, J. J., N. Garcia, P. Grütter, E. Meyer, H. Heinzelmann, R. Wiesendanger, L. Rosenthaler, H. R. Hidber, and H.-J. Güntherodt, 1987, "Observation of magnetic forces by the atomic force microscope," J. Appl. Phys. **62**, 4293–4295.

Schlickum, U., N. Janke-Gilman, W. Wulfhekel, and J. Kirschner, 2004, "Step-induced frustration of antiferromagnetic order in Mn on Fe(001)," Phys. Rev. Lett. **92**, 107203.

Schlickum, U., W. Wulfhekel, and J. Kirschner, 2003, "Spin-polarized scanning tunneling microscope for imaging the in-plane magnetization," Appl. Phys. Lett. **83**, 2016–2018.

Schmidt, R., C. Lazo, H. Hölscher, U. H. Pi, V. Caciuc, A. Schwarz, R. Wiesendanger, and S. Heinze, 2009, "Probing the magnetic exchange forces of iron on the atmoic scale," Nano Lett. **9**, 200–204.

Schwarz, A., M. Bode, and R. Wiesendanger, 2007, *in Handbook of Magnetism and Advanced Magnetic Materials*, edited by H. Kronmüller, and S. S. P. Parkin (Wiley, New York), Vol. 3, pp. 1687–1709.

Schwarz, A., M. Liebmann, U. Kaiser, R. Wiesendanger, T. W. Noh, and D. W. Kim, 2004, "Visualization of the Barkhausen effect by magnetic force microscopy," Phys. Rev. Lett. **92**, 077206.

Shinohara, R., K. Yamaguchi, H. Hirota, Y. Suzuki, T. Manago, H. Akinaga, T. Kuroda, and F. Minami, 2000, "Lifetime and spin relaxation time measurements of micro-fabricated GaAs tips," Jpn. J. Appl. Phys. **39**, 7093–7096.

Shvets, I. V., G. Mariotto, K. Jordan, N. Berdunov, R. Kantor, and S. Murphy, 2004, "Long-range charge order on the Fe_3O_4(001) surface," Phys. Rev. B **70**, 155406.

Shvets, I. V., R. Wiesendanger, D. Bürgler, G. Tarrach, H.-J. Güntherodt, and J. M. D. Coey, 1992, "Progress towards spin-polarized STM," J. Appl. Phys. **71**, 5489–5499.

Slonczewski, J. C., 1989, "Conductance and exchange coupling of two ferromagnets separated by a tunnelling barrier," Phys. Rev. B **39**, 6995–7002.

Slonczewski, J. C., 1996, "Current-driven excitation of magnetic multilayers," J. Magn. Magn. Mater. **159**, L1–L7.

Smith, A. R., R. Yang, H. Q. Yang, A. Dick, J. Neugebauer, and W. R. L. Lambrecht, 2005, "Recent advances in atomic-scale spin-polarized scanning tunneling microscopy," Microsc. Res. Tech. **66**, 72–84.

Smith, A. R., R. Yang, H. Yang, W. R. L. Lambrecht, A. Dick, and J. Neugebauer, 2004, "Aspects of spin-polarized scanning tunneling microscopy at the atomic scale: experiment, theory, and simulation," Surf. Sci. **561**, 154–170.

Stipe, B. C., M. A. Razaei, and W. Ho, 1998, "Single-molecule vibrational spectroscopy and microscopy," Science **280**, 1732–1735.

Sueoka, K., K. Mukasa, and K. Hayakawa, 1993, "Possibility of observing spin-polarized tunneling current using scanning tunneling microscope with optically pumped GaAs," Jpn. J. Appl. Phys. **32**, 2989–2993.

Tedrow, P. M., and R. Meservey, 1971, "Spin-dependent tunneling into ferromagnetic nickel," Phys. Rev. Lett. **26**, 192–195.

Tedrow, P.M., and R. Meservey, 1973, "Spin polarization of electrons tunneling from films of Fe, Co, Ni, and Gd," Phys. Rev. B **7**, 318–326.

Tersoff, J., and D. R. Hamann, 1983, "Theory and application for the scanning tunneling microscope," Phys. Rev. Lett. **50**, 1998–2001.

Tersoff, J., and D. R. Hamann, 1985, "Theory of the scanning tunneling microscope," Phys. Rev. B **31**, 805–813.

Tsoi M., A. G. M. Jansen, J. Bass, W.-C. Chiang, M. Seck, V. Tsoi., and P. Wyder, 1998, "Excitation of a magnetic multilayer by an electric current," Phys. Rev. Lett. **80**, 4281–4284.

Vázquez de Parga, A. L., and S. F. Alvarado, 1996, "Circular dichroism in STM-excited luminescence on metals," Europhys. Lett. **36**, 577–582.

Vedmedenko, E. Y., A. Kubetzka, K. von Bergmann, O. Pietzsch, M. Bode, J. Kirschner, H. P. Oepen, and R. Wiesendanger, 2004, "Domain wall orientation in magnetic nanowires," Phys. Rev. Lett. **92**, 077207.

von Bergmann, K., M. Bode, A. Kubetzka, M. Heide, S. Blügel, and R. Wiesendanger, 2004, "Spin-polarized electron scattering at single oxygen adsorbates on a magnetic surface," Phys. Rev. Lett. **92**, 046801.

von Bergmann, K., M. Bode, A. Kubetzka, O. Pietzsch, and R. Wiesendanger, 2005, "Spin-polarized scanning tunneling microscopy: Insight into magnetism from nanostructures to atomic scale spin structures," Microsc. Res. Tech. **66**, 61–71.

von Bergmann, K., M. Bode, and R. Wiesendanger, 2004, "Magnetism of iron on tungsten(001) studied by spin-resolved scanning tunneling microscopy and spectroscopy," Phys. Rev. B **70**, 174455.

von Bergmann, K., M. Bode, and R. Wiesendanger, 2006, "Coverage-dependent spin reorientation transition temperature of the Fe double-layer on W(110) observed by scanning tunnelling microscopy," J. Magn. Magn. Mater. **305**, 279.

von Bergmann, K., S. Heinze, M. Bode, E. Y. Vedmedenko, G. Bihlmayer, S. Blügel, and R. Wiesendanger, 2006, "Observation of a complex nanoscale magnetic structure in a hexagonal Fe monolayer," Phys. Rev. Lett. **96**, 167203.

Wachowiak, A., J. Wiebe, M. Bode, O. Pietzsch, M. Morgenstern, and R. Wiesendanger, 2002, "Direct observation of internal spin structure of magnetic vortex cores," Science **298**, 577–580.

Wahl, P., L. Diekhöner, M. A. Schneider, L. Vitali, G. Wittich, and K. Kern, 2004, "Kondo temperature of magnetic impurities at surfaces," Phys. Rev. Lett. **93**, 176603.

Wahl, P., P. Simon, L. Diekhöner, V. S. Stepanyuk, P. Bruno, M. A. Schneider, and K. Kern, 2007, "Exchange interaction between single magnetic adatoms," Phys. Rev. Lett. **98**, 056601.

Wiebe, J., F. Meier, K. Hashimoto, G. Bihlmayer, S. Blügel, P. Ferriani, S. Heinze, and R. Wiesendanger, 2005, "Unoccupied surface state on Pt(111) revealed by scanning tunneling spectroscopy," Phys. Rev. B **72**, 193406.

Wiesendanger, R., 1994a, *Scanning Probe Microscopy and*

Spectroscopy: Methods and Applications (Cambridge University Press, Cambridge).
Wiesendanger, R., 1994b, "Spin-polarized scanning tunneling microscopy: gateway to imaging and modification of surface spin configurations at the atomic level," J. Magn. Soc. Jpn. **18**, 4–14.
Wiesendanger, R., 1998, in *Scanning Probe Microscopy*, edited by R. Wiesendanger (Springer, Berlin), Chap. 4, pp. 71–95.
Wiesendanger, R., 1999, "Surface magnetism at the nanometer and atomic scale," Curr. Opin. Solid State Mater. Sci. **4**, 435–440.
Wiesendanger, R., 2007, "Mapping spin structures on the atomic scale," Europhys. News **38**, 16–21.
Wiesendanger, R., D. Anselmetti, and H.-J. Güntherodt, 1990, "Advances in STM design and instrumentation," Europhys. News **21**, 72–73.
Wiesendanger, R., and M. Bode, 2001, "Nano- and atomic-scale magnetism studied by spin-polarized scanning tunneling microscopy and spectroscopy," Solid State Commun. **119**, 341–355.
Wiesendanger, R., M. Bode, and M. Getzlaff, 1999, "Vacuum-tunneling magnetoresistance: the role of spin-polarized surface states," Appl. Phys. Lett. **75**, 124–126.
Wiesendanger, R., M. Bode, A. Kubetzka, O. Pietzsch, M. Morgenstern, A. Wachowiak, and J. Wiebe, 2004, "Fundamental studies of magnetism down to the atomic scale: present status and future perspectives of spin-polarized scanning tunneling microscopy," J. Magn. Magn. Mater. **272-276**, 2115–2120.
Wiesendanger, R., D. Bürgler, G. Tarrach, D. Anselmetti, H. R. Hidber, and H.-J. Güntherodt, 1990, "An ultrahigh vacuum scanning tunneling microscope for the investigation of clean surfaces," J. Vac. Sci. Technol. A **8**, 339–344.
Wiesendanger, R., D. Bürgler, G. Tarrach, T. Schaub, U. Hartmann, H.-J. Güntherodt, I. V. Shvets, and J. M. D. Coey, 1991, "Recent advances in scanning tunneling microscopy involving magnetic probes and samples," Appl. Phys. A: Mater. Sci. Process. **53**, 349–355.
Wiesendanger, R., D. Bürgler, G. Tarrach, A. Wadas, D. Brodbeck, H.-J. Güntherodt, G. Güntherodt, R. J. Gambino, and R. Ruf, 1991, "Vacuum tunneling of spin-polarized electrons detected by scanning tunneling microscopy," J. Vac. Sci. Technol. B **9**, 519–524.
Wiesendanger, R., and H.-J. Güntherodt, 1990, "Surface step and defect structure of Cr(001) studied by scanning tunneling microscopy," Surf. Sci. **235**, 1–4.
Wiesendanger, R., H.-J. Güntherodt, G. Güntherodt, R. J. Gambino, and R. Ruf, 1990a, "Observation of vacuum tunneling of spin-polarized electrons with the scanning tunneling microscope," Phys. Rev. Lett. **65**, 247–250.
Wiesendanger, R., H.-J. Güntherodt, G. Güntherodt, R. J. Gambino, and R. Ruf, 1990b, "Scanning tunneling microscopy with spin-polarized electrons," Z. Phys. B: Condens. Matter **80**, 5–6.
Wiesendanger, R., H.-J. Güntherodt, G. Güntherodt, R. J. Gambino, and R. Ruf, 1990c, "Measurement of the local electron spin polarization by the scanning tunneling microscope," Helv. Phys. Acta **63**, 778–782.
Wiesendanger, R., I. V. Shvets, D. Bürgler, G. Tarrach, H.-J. Güntherodt, J. M. D. Coey, and S. Gräser, 1992a, "Topographic and magnetic-sensitive scanning tunneling microscopy study of magnetite," Science **255**, 583–586.
Wiesendanger, R., I. V. Shvets, D. Bürgler, G. Tarrach, H.-J. Güntherodt, and J. M. D. Coey, 1992b, "Evidence for selective imaging of different magnetic ions on the atomic scale by using a scanning tunneling microscope with a ferromagnetic probe tip," Europhys. Lett. **19**, 141–146.
Wiesendanger, R., I. V. Shvets, D. Bürgler, G. Tarrach, H.-J. Güntherodt, and J. M. D. Coey, 1992c, "Magnetic imaging at the atomic level," Z. Phys. B: Condens. Matter **86**, 1–2.
Wiesendanger, R., I. V. Shvets, and J. M. D. Coey, 1994, "Wigner glass on the magnetite (001) surface observed by scanning tunneling microscopy with a ferromagnetic tip," J. Vac. Sci. Technol. B **12**, 2118–2121.
Wortmann, D., S. Heinze, P. Kurz, G. Bihlmayer, and S. Blügel, 2001, "Resolving complex atomic-scale spin structures by spin-polarized scanning tunneling microscopy," Phys. Rev. Lett. **86**, 4132–4135.
Wortmann, D., P. Kurz, S. Heinze, K. Hirai, G. Bihlmayer, and S. Blügel, 2002, "Resolving noncollinear magnetism by spin-polarized scanning tunneling microscopy," J. Magn. Magn. Mater. **240**, 57–63.
Wu, R., and A. J. Freeman, 1992, "Magnetic properties of Fe overlayers on W(001) and the effects of oxygen adsorption," Phys. Rev. B **45**, 7532–7535.
Wulfhekel, W., 2005, in *Magnetic Microscopy of Nanostructures*, edited by H. Hopster and H. P. Oepen (Springer, Berlin), Chap. 9, pp. 181–202.
Wulfhekel, W., H. F. Ding, and J. Kirschner, 2000, "High-resolution study of magnetization and susceptibility by spin-polarized scanning tunneling microscopy," J. Appl. Phys. **87**, 6475–6477.
Wulfhekel, W., R. Hertel, H. F. Ding, G. Steierl, and J. Kirschner, 2002, "Amorphous, low magnetostriction tips for spin-polarized scanning tunneling microscopy," J. Magn. Magn. Mater. **249**, 368–374.
Wulfhekel, W., and J. Kirschner, 1999, "Spin-polarized scanning tunneling microscopy on ferromagnets," Appl. Phys. Lett. **75**, 1944–1946.
Wulfhekel, W., U. Schlickum, and J. Kirschner, 2005, "Topological frustrations in Mn films on Fe(001)," Microsc. Res. Tech. **66**, 105–116.
Yamada, T. K., M. M. J. Bischoff, G. M. M. Heijnen, T. Mizoguchi, and H. van Kempen, 2003a, "Origin of magnetic contrast in spin-polarized scanning tunneling spectroscopy: experiments on ultra-thin Mn films," Jpn. J. Appl. Phys. **42**, 4688–4691.
Yamada, T. K., M. M. J. Bischoff, G. M. M. Heijnen, T. Mizoguchi, and H. van Kempen, 2003b, "Observation of spin-polarized surface states on ultrathin bct Mn(001) films by spin-polarized scanning tunneling spectroscopy," Phys. Rev. Lett. **90**, 056803.
Yamada, T. K., M. M. J. Bischoff, T. Mizoguchi, and H. van Kempen, 2003, "Use of voltage pulses to detect spin-polarized tunneling," Appl. Phys. Lett. **82**, 1437–1439.
Yamada, T. K., A. L. Vázquez de Parga, M. M. J. Bischoff, T. Mizoguchi, and H. van Kempen, 2005, "Evaluation of sample spin-polarization from spin-polarized scanning tunneling spectroscopy experiments," Microsc. Res. Tech. **66**, 93–104.
Yamasaki, A., W. Wulfhekel, R. Hertel, S. Suga, and J. Kirschner, 2003, "Direct observation of the single-domain limit of Fe nanomagnets by spin-polarized scanning tunneling spectroscopy," Phys. Rev. Lett. **91**, 127201.
Yang, H., A. R. Smith, M. Prikhodko, and W. R. L. Lambrecht, 2002, "Atomic-scale spin-polarized scanning tunneling microscopy applied to $Mn_3N_2(010)$," Phys. Rev. Lett. **89**, 226101.

Yang, R., H. Yang, and A. R. Smith, 2006, "Energy-dependent contrast in atomic-scale spin-polarized scanning tunneling microscopy of Mn_3N_2 (010): Experiment and first-principles theory," Phys. Rev. B **74**, 115409.

Yayon, Y., V. W. Brar, L. Senapati, S. C. Erwin, and M. F. Crommie, 2007, "Observing spin polarization of individual magnetic adatoms," Phys. Rev. Lett. **99**, 067202.

Young, R., J. Ward, and F. Scire, 1971, "Observation of metal-vacuum-metal tunnelling, field emission, and transition region," Phys. Rev. Lett. **27**, 922–924.